UNIVERSITÉ DE GRENOBLE

THÈSE

Pour obtenir le grade de

DOCTEUR DE L'UNIVERSITÉ DE GRENOBLE

Spécialité : **Terre Solide**

Arrêté ministériel : 7 août 2006

Présentée par

« Céline HADZIIOANNOU »

Thèse dirigée par **« Michel CAMPILLO »** et
codirigée par **« Eric LAROSE »**

préparée au sein du **Laboratoire de Géophysique Interne et Tectonophysique**
dans **l'École Doctorale Terre, Univers, Environnement**

Ondes sismiques en milieu complexe : Mesure des variations temporelles des vitesses

Thèse soutenue publiquement le **« 17 janvier 2011 »**,
devant le jury composé de :

M. Philippe ROUX
Chargé de recherche, LGIT Grenoble, Président
M. Jean-Pierre VILOTTE
Professeur, IPG Paris, Rapporteur
M. Heiner IGEL
Professeur, LMU Munich, Rapporteur
M. Yehuda BEN-ZION
Professeur, USC Earth Sciences Los Angeles, Membre
M. Michel CAMPILLO
Professeur, LGIT Grenoble, Membre
M. Eric LAROSE
Chargé de recherche, LGIT Grenoble, Membre

Abstract :

Cette thèse se concentre sur le suivi temporel des vitesses sismiques, notamment dans des zones de faille actives. En corrélant les signaux générés par le bruit ambiant, il est possible d'estimer la fonction de Green du milieu. Par le suivi continu de ces fonctions, des changements de vitesse dans le milieu peuvent être détectés.
Les méthodes de suivi temporel sont appliquées aux données provenant d'une zone de faille active à Parkfield, Californie, ce qui permet de détecter deux chutes de vitesse. Ces dernières coéfncident avec des évènements sismiques régionaux, la plus importante concernant un évènement proche des stations. Les deux chutes de vitesse sont suivies d'une récupération postsismique progressive.
Pour mieux comprendre la fiabilité des mesures on a effectué des expériences en laboratoire. Un résultat intéressant de ces expériences montre que la reconstruction exacte de la fonction de Green n'est pas nécessaire pour le suivi temporel, ce qui ouvre la voie à de nombreuses possibilités d'applications en sismologie.
Grâce à cette connaissance, la série de données de Parkfield a été ré-analysée. En améliorant la résolution temporelle à 1 journée, on montre que la chute de vitesse observée est cosismique avec le séisme de Parkfield. On a établi que les fluctuations de vitesse ne sont pas simplement corrélées aux variations de la distribution de sources du bruit obtenue par formation de voies.
Enfin, les méthodes développées sont appliquées à un séisme au Japon. Le réseau étant de taille beaucoup plus grande que celui utilisé pour l'étude de Parkfield, ces données sont analysées pour étudier la dépendance entre la distance stations-séisme et la chute de vitesse mesurée.

Table des matières

1 Introduction **1**

1.1 Contexte Général 1

1.2 Contexte de cette Thèse 4

2 Theorie : Ondes Sismiques **5**

2.1 Équation d'Onde 5

2.2 Ondes de la Coda 6

2.3 Fonction de Green 9

2.4 Inter-corrélation 10

2.4.1 Aperçu Historique 10

2.4.2 Inter-corrélation et Renversement de Temps 11

2.5 Bruit Sismique Ambiant 13

3 Théorie : Monitoring **17**

3.1 Changement de Vitesse 17

3.2 Méthode des Doublets 18

3.2.1 Utilisation de Corrélations de Bruit 20

3.3 Méthode de Stretching 21

4 Parkfield I **23**

4.1 Summary 23

4.2 Postseismic relaxation along the San Andreas fault 25

4.3 Introduction . . . 25
4.4 Data Used . . . 26
4.5 Noise correlation Processing . . . 26
4.6 Stability of noise correlation . . . 28
4.7 Clock Corrections . . . 28
4.8 Velocity Variation Measurement . . . 29
4.9 Results . . . 30
4.10 Non-volcanic Tremor . . . 33
4.11 Conclusion . . . 34
4.12 Questions Raised . . . 34

5 Laboratory experiments 37

5.1 Summary . . . 37
5.2 Stability of monitoring . . . 39
5.3 Introduction . . . 39
5.4 Methodology . . . 41
5.4.1 Motivations for doing analogous laboratory experiments . . . 41
5.4.2 Scattering properties of the medium . . . 42
5.5 Comparison of data processing techniques . . . 43
5.5.1 Active experiment : high quality data. . . . 43
5.5.2 Active experiment : low quality data . . . 47
5.5.3 Advantages and drawbacks of both techniques . . . 49
5.6 Monitoring with the correlation ? . . . 51

5.7 Influence of noise source stability 53
5.8 Discussion and Perspectives 56
5.9 Calculations 57
5.9.1 High Quality Data 57
5.9.2 Low Quality Data 59
5.10 Questions Raised 60

6 Precision of measurements 63

6.1 Introduction 63
6.2 Apparent Dilation 63
6.2.1 Calculation 65
6.3 Application : Laboratory Experiments 66
6.4 Application : Parkfield 68
6.5 Conclusion 70

7 Parkfield II 71

7.1 Summary 71
7.2 Improving the temporal resolution 73
7.3 Introduction 73
7.4 Parkfield Data 76
7.5 Method : Adaptive Filter 78
7.5.1 The S-transform 78
7.5.2 Construction of the Self-Filter 79
7.6 Method : Doublets & Stretching 80

7.7 Results . . . 81
7.7.1 Velocity Variations from Doublets . . . 82
7.7.2 Velocity Variations from Stretching . . . 83
7.8 Beamforming . . . 85
7.9 Error calculation . . . 88
7.10 Discussion . . . 88
7.11 Conclusion . . . 89

8 Japan **91**

8.1 Introduction . . . 91
8.2 Data . . . 91
8.3 Method : Processing . . . 93
8.3.1 Clock Error Correction . . . 94
8.3.2 Velocity Variation Measurement . . . 97
8.3.3 Coda Coherence . . . 98
8.3.4 Quality Control . . . 99
8.4 Velocity Variations . . . 100
8.4.1 Distance dependence . . . 102
8.5 Discussion & Conclusion . . . 106

9 Conclusion **107**

10 Perspectives **109**

10.1 Parkfield : 9-component Green's Tensor . . . 109

10.2 Localization 110

A Appendix **113**

A.1 On the precision of noise-correlation interferometry 113

A.1.1 Introduction 113

A.1.2 Dilation Correlation Coefficient 115

A.1.3 Comparison with Experiment 120

A.1.4 Comparison with Seismic Data from Parkfield 123

A.1.5 Summary 125

Bibliographie **127**

Chapitre 1

Introduction

Contents

1.1 Contexte Général 1
1.2 Contexte de cette Thèse 4

1.1 Contexte Général

L'un des buts de la sismologie est l'étude de la structure interne de la Terre grâce à l'utilisation des ondes sismiques. L'intérieur et la croûte de la Terre sont constitués de matériaux de densité, de structure et même de température variables. Tous ces facteurs influent sur la vitesse de propagation des ondes. Pour extraire l'information recherchée, on peut mesurer la vitesse de propagation en utilisant les ondes sismiques. Les ondes sismiques correspondant à différents séismes enregistrés par une station auront traversé des régions de la Terre avec des vitesses différentes. Lorsqu'on a accumulé suffisamment de trajectoires différentes entre séisme et station, on peut en déduire un modèle de vitesse spatiale correspondant aux vitesses de propagation mesurées sur ces trajectoires.

Comme on peut le voir sur la figure 1.1, la plupart des séismes se produisent le long des limites de plaques tectoniques et des zones de failles. Cela veut dire que les sources sont souvent localisées au même endroit, ce qui limite la diversité des trajectoires source – récepteur disponibles. La distribution hétérogène des séismes implique aussi qu'il existe sur la Terre de grandes régions ayant très peu de sources, ou bien où les seules sources sont éloignées. L'absorption rapide des fréquences élevées du signal complique encore davantage l'imagerie de la croûte dans ces régions. Enfin, l'occurrence irrégulière des séismes ne facilite pas l'étude de l'évolution temporelle des structures tectoniques.

La corrélation de bruit offre une alternative aux techniques classiques d'imagerie en sismologie. Au lieu de dépendre des séismes comme sources de signaux, on peut calculer ces derniers. L'intercorrélation du bruit sismique ambiant permet de générer

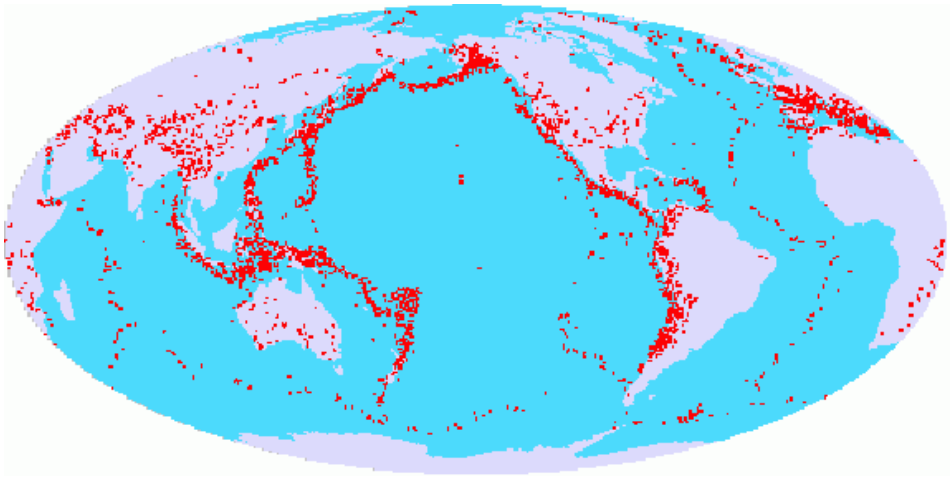

FIG. 1.1 – Distribution globale des séismes durant une période d'un an. On notera que la plupart des séismes se produisent le long des limites de plaques.

des 'sismogrammes', ou réponses impulsionnelles, entre deux stations dont l'une agit comme source et l'autre comme récepteur. Cela signifie qu'il y a autant de trajectoires possibles que de paires de stations. Elles peuvent être localisées partout où l'on peut installer une station, ce qui élimine le problème de distribution des séismes (sources). Les stations pouvant être placées à proximité l'une de l'autre, l'atténuation des hautes fréquences est moins problématique, ce qui permet une imagerie de plus haute résolution.

Comme les séismes se produisent de façon irrégulière, la plupart des stations sismiques enregistrent en continu afin de capter tout évènement. Par conséquent, la plupart du temps elles enregistrent du bruit sismique (fig. 1.2). L'intercorrélation nous permet d'exploiter tous ces enregistrements de bruit, que l'on croyait jusqu'ici inutiles. Cet avantage permet de réaliser une tomographie crustale de haute résolution, même dans des régions asismiques.

Un autre avantage des intercorrélations est qu'elles permettent de 'générer' des sismogrammes à volonté, là ou l'on place deux stations. On peut comparer les sismogrammes pour la même trajectoire à des dates différentes. En mesurant les changements dans les signaux, nous pouvons suivre l'évolution du milieu. Autrement dit, l'intercorrélation accroît la possibilité d'étudier la croûte terrestre. La vitesse sismique reflète les propriétés du milieu telles que température, stress, endommagement subi, etc. Le suivi de ce qui se passe avec les vitesses d'ondes locales lors d'évènements naturels (éruptions volcaniques, séismes, glissements de terrain) peut nous mener à mieux comprendre ces processus.

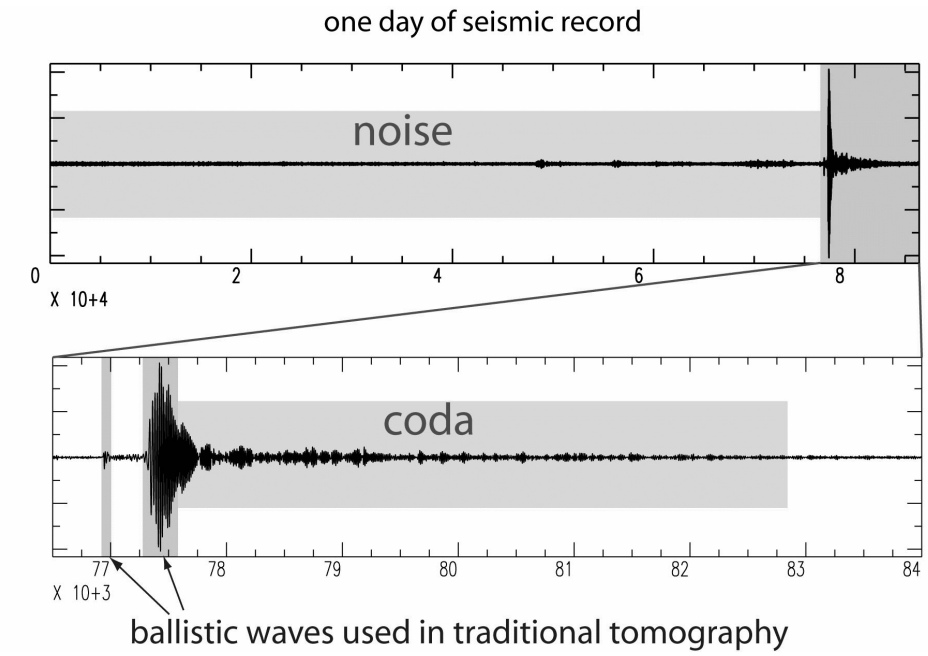

FIG. 1.2 – Exemple d'enregistrement en continu durant une journée incluant un séisme de grande magnitude. 95 % environ de l'enregistrement sont constitués de bruit, 4 % de la coda. Les ondes balistiques utilisées en tomographie traditionnelle ne constituent que 1 % du signal.

1.2 Contexte de cette Thèse

Lorsque j'ai commencé ce travail de thèse, le domaine du suivi temporel des vitesses de propagation sismiques démarrait seulement, avec des résultats prometteurs sur des volcans actifs [Sens-Schönfelder and Wegler, 2006; Brenguier et al., 2008b]. L'objectif de ce travail était d'explorer les limites du suivi temporel en utilisant le bruit ambiant. En particulier, j'ai étudié l'application des méthodes de monitoring à des zones de failles actives.

Le chapitre 2 présente le contexte théorique et historique des intercorrélations de bruit ambiant. Les méthodes employées pour suivre les variations de vitesse sont décrites dans le chapitre 3.

Dans le chapitre 4, nous appliquons ces méthodes de suivi temporel aux données de la faille San Andreas, près de Parkfield, pour voir si l'on peut détecter une variation de vitesse dans une zone de faille lors d'un tremblement de terre.

Dans le chapitre 5, nous explorons les limites des méthodes de suivi temporel dans un environnement de laboratoire contrôlé. Spécifiquement, nous étudions l'importance de la reconstruction complète de la fonction de Green. Le chapitre 6 propose une estimation de la précision des variations de vitesse mesurées.

Sur la base des connaissances acquises dans les deux chapitres précédents, dans le chapitre 7 nous répétons les mesures de variations de vitesse sur les données du chapitre 4. La résolution temporelle des mesures est fortement améliorée. L'influence de la distribution de sources de bruit sur les mesures est également évaluée.

Enfin, dans le chapitre 8, nous testons le suivi temporel sur un ensemble différent de données. Nous étudions la relation entre la distance et les variations de vitesse.

Après la conclusion (chapitre 9), dans le chapitre 10, nous présenterons divers résultats méritant la poursuite des recherches.

Chapitre 2

Theorie : Ondes Sismiques

Contents

2.1 Équation d'Onde 5
2.2 Ondes de la Coda 6
2.3 Fonction de Green 9
2.4 Inter-corrélation 10
2.4.1 Aperçu Historique 10
2.4.2 Inter-corrélation et Renversement de Temps 11
2.5 Bruit Sismique Ambiant 13

2.1 Équation d'Onde

On peut décrire les ondes sismiques comme la propagation de déformations locales dans un milieu élastique. Dans le cas d'un milieu homogène isotrope, la loi de mouvement de Newton peut s'écrire :

$$\frac{\partial^2 \mathbf{u}}{\partial t^2} = \frac{\lambda + 2\mu}{\rho} \nabla (\nabla \cdot \mathbf{u}) - \frac{\mu}{\rho} \nabla \times (\nabla \times \mathbf{u}) + \mathbf{f}, \tag{2.1}$$

où $\mathbf{u}$ représente le déplacement, ρ la densité de masse et $\mathbf{f}$ la fonction source. Les paramètres de Lamé λ et μ décrivent les propriétés élastiques du milieu. Par la suite, nous supposons initialement qe le milieu est homogène, ce qui signifie que λ, μ et ρ sont constants dans tout le milieu. Nous supposons également que le milieu est isotrope : la propagation d'onde est la même dans toutes les directions.

L'analyse de cette équation utilisant la décomposition de Helmholtz nous donne deux vitesses :

$$v_p = \sqrt{\frac{(\lambda + \mu)}{\rho}} \text{ and } v_s = \sqrt{\frac{\mu}{\rho}}. \tag{2.2}$$

Ces deux vitesses correspondent à deux types de propagation d'ondes : les ondes de compression longitudinale (v_p, figure 2.1a) et les ondes de cisaillement transversal (v_s, figure 2.1b). Les ondes de compression se déplacent plus rapidement que les ondes de cisaillement et par conséquent on les appelle ondes 'primaires' ou ondes P. De même, les ondes de cisaillement seront appelées ondes 'secondaires' ou ondes S. Les ondes P sont polarisées selon la direction de propagation, alors que les ondes S sont polarisées perpendiculairement à la propagation.

A l'interface entre le milieu et le vide ou l'air, ces deux types d'ondes interfèrent ce qui produit des ondes de surface. Deux principaux types d'ondes de surface résultent de cette interférence, les ondes de Rayleigh et les ondes de Love. Les ondes de Rayleigh résultent du couplage entre les ondes P et la composante de polarisation dans le plan d'incidence des ondes S (S_V). Il s'ensuit un mouvement rétrograde elliptique dans le plan vertical le long de l'axe de propagation (figure 2.1c). Les ondes de Love résultent de l'interférence constructive des composantes de polarisation horizontale des ondes S (S_H) qui sont emprisonnées entre surface et profondeur. Elles ne se produisent que si la vitesse de propagation des ondes S varie avec la profondeur. Le mouvement des particules qui en résulte est un mouvement de cisaillement horizontal (figure 2.1d).

Comme indiqué ci-dessus, ce sont les ondes P qui se déplacent le plus rapidement et seront enregistrées les premières dans les stations sismiques après un séisme (voir figure 2.2), suivies des ondes S. Les ondes de surface se propagent typiquement plus lentement que les ondes P et S et seront détectées plus tard.

Dans le cas d'un milieu stratifié horizontalement, le sismogramme devient plus complexe. Des arrivées supplémentaires sont enregistrées, qui correspondent à des ondes réfléchies et converties aux interfaces des strates. Il est cependant toujours possible de (modéliser) ces ondes, et elles sont donc utilisables pour l'imagerie.

2.2 Ondes de la Coda

En réalité, la Terre n'est pas un simple milieu homogène et stratifié. Elle présente au contraire des hétérogénéités à toutes échelles. Une partie des ondes générées à la source vont être réfléchies aux interfaces entre les strates, d'autres seront réfractées ou réfléchies lorsqu'elles rencontreront des hétérogénéités dans la croûte terrestre [Aki and Chouet, 1975]. La figure 2.3 propose une illustration schématique de trajectoires possibles. La somme de toutes ces interactions résulte en un champ d'ondes *diffusées*.

Ces ondes diffusées parcourent des distances bien plus longues et arrivent à la station sismique encore plus tard que les ondes de surface. Les ondes diffusées constituent

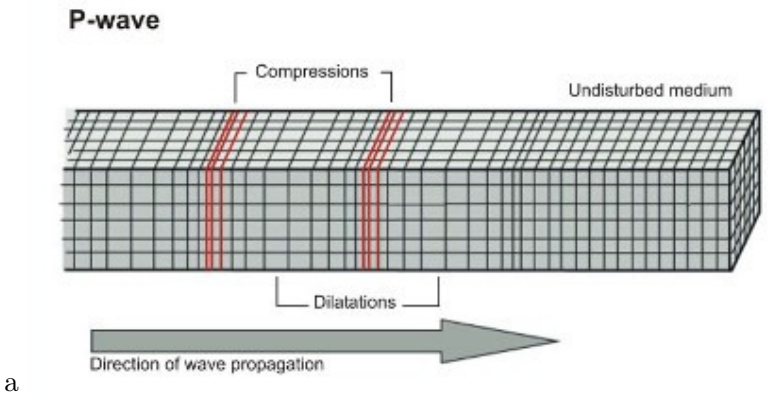

a

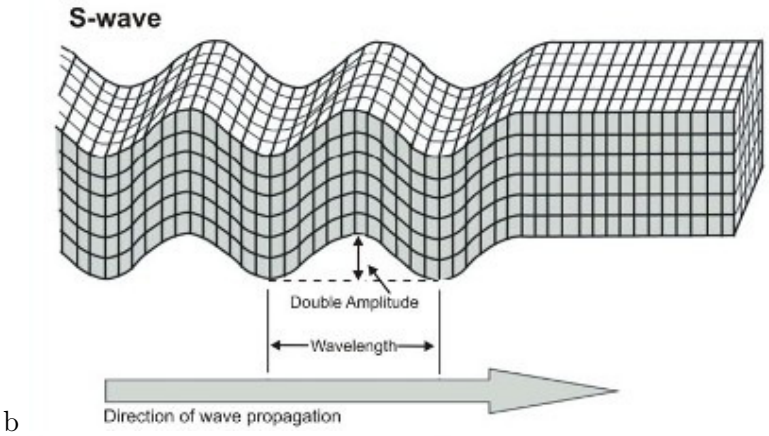

b

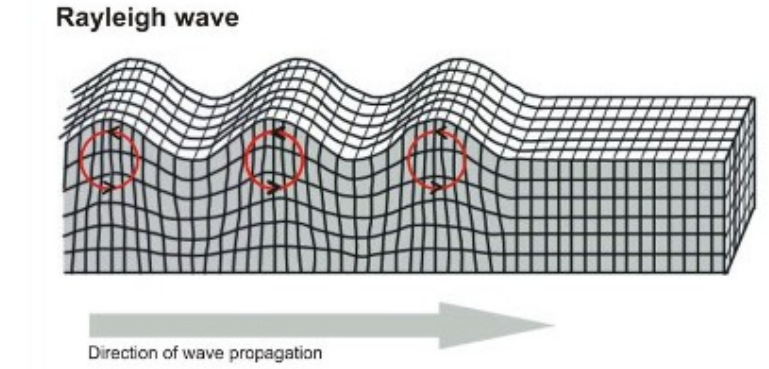

c

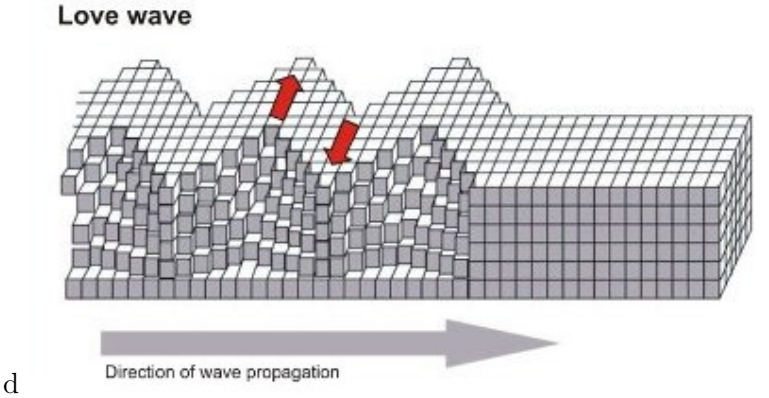

d

FIG. 2.1 – Différents types d'ondes sismiques. Les flèches horizontales indiquent la direction de propagation.

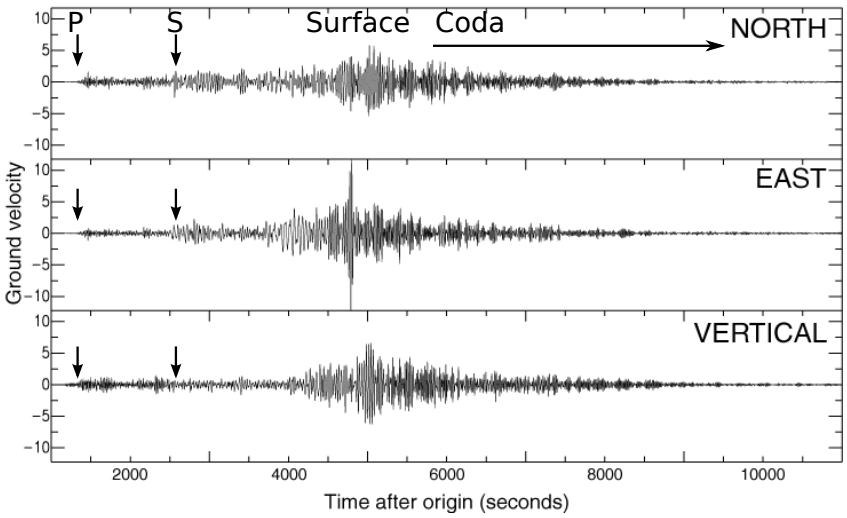

FIG. 2.2 – Exemple de sismogramme (3 composantes) : enregistrement du séisme de Sumatra du 26 décembre 2004 par une station sismique située en Arizona. On peut identifier les ondes P et S ainsi que les ondes de surface, suivi par la coda qui dure plusieurs minutes.

la dernière partie d'un séismogramme (figure 2.2). Par analogie avec la fin d'un morceau de musique, cette 'queue' d'un sismogramme est désignée par le terme *coda*.

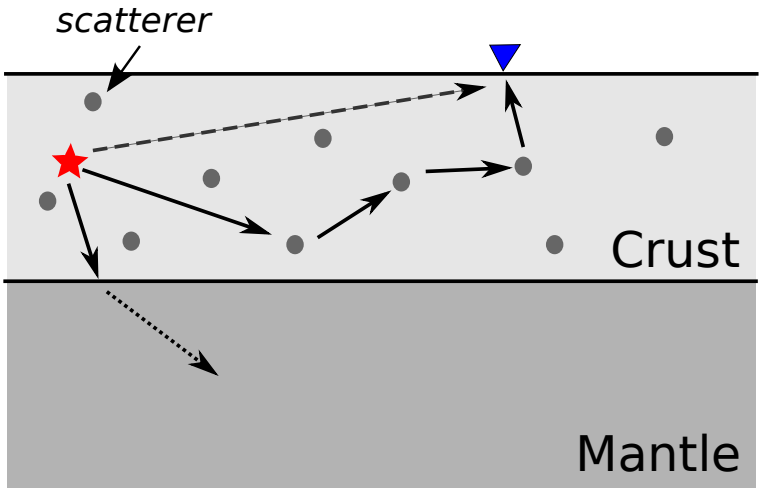

FIG. 2.3 – Illustration de la difusion dans la croûte terrestre. Les ondes seront diffusées par des inhomogenéités dans la croûte (ligne continue). Selon l'angle d'incidence sur la Moho, certaines ondes dans le manteau (ligne pointillée).

Chaque fois que l'onde est réfléchie par un diffuseur, elle change de direction, de phase et d'amplitude. Etant donné le champ d'ondes diffusées, on peut comprendre que la somme de tous ces changements de direction aléatoires conduira finalement à

un champ d'ondes isotrope au niveau du récepteur. De plus, lors de chaque réflexion il se produit une conversion d'un type d'onde en un autre. Il s'ensuit une équipartition de l'énergie entre les différents types d'ondes [Hennino et al., 2001]. Cet état d'équipartition spatiale et énergétique est une propriété importante et utile de la coda.

La coda résultant d'une importante succession de réflexions à partir de diffuseurs, il est impossible de prédire sa forme d'onde a priori. C'est la raison pour laquelle elle est inutilisable en imagerie, et on a longtemps pensé qu'il était impossible de tirer des informations utiles de la coda. Pourtant, aussi aléatoire le signal puisse-t-il sembler, la coda est déterministeÂ : la forme d'onde reste la même d'un enregistrement à l'autre tant que le milieu et la source restent inchangé. Toutefois, la forme d'onde est perturbée dès qu'un diffuseur est modifié. Cet effet s'accentue pour les longues trajectoires, c'est à dire si l'on regarde plus loin dans le signal. Ceci, ajouté au fait que le champ d'ondes a longuement échantillonné le milieu, rend la coda très sensible à de faibles changements dans les propriétés du milieu.

Dans le présent travail nous nous proposons d'exploiter ces caractéristiques de la coda pour mesurer de faibles changements de vitesse dans la croûte terrestre.

2.3 Fonction de Green

La fonction de Green, parfois aussi appelée réponse impulsionnelle, est la solution de l'équation d'onde (2.1) pour une source impulsionnelle. Autrement dit, la fonction de Green décrit le signal qui serait enregistré par le récepteur si la source était une impulsion delta. La fonction de Green contient toute les informations sur les ondes qui se sont déplacées de la source au récepteur, et donc aussi sur le milieu traversé. On peut comprendre l'importance de la fonction de Green pour les sismologues : on peut considérer les sismogrammes comme étant une fonction de Green convolué avec un terme source plus complexe.

Pour déterminer la structure de la croûte terrestre, l'idéal pour les sismologues serait d'utiliser toutes les fonctions de Green des ondes qui la traversent. En pratique toutefois, ce qui se rapproche le plus de la fonction de Green est le sismogramme, qui inclut toujours la signature de la source. Cela peut constituer un problème, car il n'est pas toujours évident de supprimer les caractéristiques de la source. De plus, comme nous l'avons vu dans le chapitre 1, l'occurrence des séismes n'est pas distribuée uniformément dans le temps et l'espace.

2.4 Inter-corrélation

Ces dernières années, on a utilisé en sismologie une façon alternative d'extraire la fonction de Green. On a trouvé que la corrélation d'un champ d'ondes aléatoire, enregistré en deux points, donne la fonction de Green entre ces points [Weaver and Lobkis, 2001].

2.4.1 Aperçu Historique

Aki [1957] a introduit le concept qui consiste à utiliser le bruit de fond sismique pour extraire les courbes de dispersion d'onde de surface, une idée qui conduira au développement de la méthode SPAC. Plus tard, Claerbout [1968] a proposé l'utilisation de l'auto-corrélation de bruit sismique pour en déduire le profil de réflexion sous une station sismique, ce qui, à l'époque, n'a pas été confirmé expérimentalement par des applications.

La première application de la méthode d'inter-corrélation a eu lieu en heliosismologie, oú l'on a utilisé les fluctuations à la surface du soleil pour étudier la propagation des ondes P à l'intérieur de l'astre [Duvall et al., 1993].

Plus tard, lors d'expériences en laboratoire d'acoustique, Weaver and Lobkis [2001] ont montrée que l'auto-corrélation de fluctuations thermiques à la surface d'un bloc d'aluminium correspondaient à la réponse impulsionnelle pour une source et un récepteur placés au même point de mesure. Ils ont aussi montré qu'il était possible d'extraire la fonction de Green dans une cavité fermée réverbérante à l'aide d'une source unique [Lobkis and Weaver, 2001]. D'une certaine façon, l'utilisation de réverbérations pour établir un champ d'ondes aléatoire est similaire à l'utilisation de la diffusion dans un milieu hétérogène. Dans ce travail, nous expliquons la reconstruction de la fonction de Green à l'aide de l'excitation de tous les modes possibles de milieux avec par une même quantité d'énergie. Cela ne peut se faire que dans un système fermé présentant un nombre fini de modes et aucune absorption, tel que ceux considérés dans les expériences.

Ces résultats expérimentaux ont entraîné le développement de diverses interprétations théoriques de la reconstruction de la fonction de Green. Derode et al. [2003b,a] l'ont expliqué par analogie avec le renversement du temps, ce qui permet l'application à un milieu ouvert (voir section 2.4.2)

Snieder [2004] et Roux et al. [2005] introduisent le concept de *zones cohérentes*. Au sein d'un milieu homogène dans lequel les sources sont disposées de façon isotrope autour des récepteurs, ce sont les sources en ligne avec les récepteurs qui contribueront le plus à la fonction de Green. Considérons deux récepteurs désignés par R_A et

R_B, séparés par une distance D. La zone cohérente est définie par les sources situées aux points S satisfaisant l'équation $\frac{\omega}{v}(\|SA - SB\| - D) < \frac{\pi}{3}$, dans laquelle ω est la fréquence centrale du champ d'ondes et v la vitesse de propagation. Les sources situées dans ces régions en forme d'hyperboles interagiront de façon constructive et contribueront donc à la reconstruction de la fonction de Green. Les sources situées à l'extérieur de ces régions contribueront de façon aléatoire, s'annulant mutuellement. Wapenaar [2004] aborde le problème par le théorème de réciprocité, tout en étudiant les cas où ce théorème n'est pas vérifié (p.ex. dans les fluides, Wapenaar and Fokkema [2006]).

Les théories concernant la sismologie présentent la différence majeure qu'il s'agit d'un milieu élastique, mettant en jeu non seulement les ondes P mais aussi les ondes S. Sanchez-Sesma and Campillo [2006] ont établi que pour que l'inter-corrélation fonctionne dans ce cas, le champ d'ondes devait être équipartitionné. Cela peut s'obtenir de deux façons :

– les sources de bruit primaires sont distribuées au hasard spatialement dans le milieu,

– les sources sont localisées, mais le milieu est hétérogène, avec des diffuseurs agissant comme sources secondaires.

Le second critère signifierait qu'il est possible d'utiliser le champ d'ondes diffusées de la coda pour reconstruire la fonction de Green. En effet, Campillo and Paul [2003] ont montré qu'il était possible d'extraire des ondes de surface par corrélation d'ondes coda consécutives à un séisme. Les ondes coda n'étant rien d'autre que des ondes diffusées provenant d'une source localisée, cela correspond à la seconde possibilité ci-dessus. Plus tard, Shapiro and Campillo [2004] ont montré qu'on pouvait aussi utiliser le bruit sismique ambiant.

Depuis, de nombreuses études tomographiques ont été faites à partir fonctions de Green reconstruit à partir de bruit sismique. Par exemple, Shapiro et al. [2005] ont généré une image tomographique de haute résolution de la Californie en utilisant des fonctions de corrélation. D'autres études ont été faites, entre autres, par [Yao et al., 2006, 2008; Yang et al., 2010; Brenguier et al., 2007; Bensen et al., 2008].

2.4.2 Inter-corrélation et Renversement de Temps

Une façon intuitive de démontrer la reconstruction de la fonction de Green est de comparer l'inter-corrélation aux principes de renversement du temps [Derode et al., 2003b].

En renversement du temps acoustique, des récepteurs entourant le milieu enregistrent un train d'ondes. Le signal est ensuite renversé en temps puis retransmis dans le milieu. Les ondes réémises se propagent alors en empruntant les mêmes itinéraires qu'à l'aller, pour se reconcentrer à l'emplacement du signal source [Fink, 1992].

Considérons un milieu ouvert, réciproque, avec une source S émettant une impulsion $e(t)$. Le signal enregistré par le récepteur A est $h_{AS}(t) \otimes e(t)$ oú $h_{AS}(t)$ est la réponse à l'impulsion et $\otimes$ représente la convolution. De même, le récepteur B va enregistrer un signal $h_{BS}(t) \otimes e(t)$ (voir illustration 2.4, à gauche). Sachant que l'inter-corrélation est exprimée par $XC_{xy} = x(t) \otimes y(-t)$, la corrélation des signaux enregistrés en A et en B s'écrit :

$$\begin{aligned} XC_{AB} &= e(t) \otimes h_{AS}(t) \otimes e(-t) \otimes h_{BS}(-t) \\ &= h_{AS}(t) \otimes h_{BS}(-t) \otimes f(t) \end{aligned} \tag{2.3}$$

oú $f(t) = e(t) \otimes e(-t)$. Nous pouvons à présent comparer ce résultat avec un cas de renversement du temps : imaginons que B émette une pulsation qui est enregistrée en S comme réponse à l'impulsion $h_{SB}(t)$. Le signal enregistré est renversé en temps et $h_{SB}(-t)$ est réémis et enregistré à nouveau en A comme $h_{SB}(-t) \otimes h_{SA}(t)$ (voir illustr. 2.4, à droite). On remarquera que, à part le terme source $f(t)$, cette expression est identique à 2.3.

Considérons maintenant le cas oú au lieu d'avoir une source S unique, nous avons un nombre infini de sources entourant les récepteurs A et B. Si A émet une pulsation, elle se propage dans toutes les directions dans le milieu, y compris le long de B, qui enregistre $h_{BA}(t)$. Le train d'ondes continue à se propager vers chacune des sources S, qui enregistrent le signal arrivant, le renversent en temps et le réémettent. Pour raison de réciprocité, les ondes se propagent alors exactement en en sens inverse, et cette fois B enregistre $h_{BA}(-t)$. Nous voyons donc que si nous avons suffisamment de sources S, nous pouvons extraire la fonction de Green de A à B :

$$\sum_{sources} h_{AS}(t) \otimes h_{SB}(-t) = h_{BA}(t) + h_{BA}(-t).$$

Derode et al. [2003b] ont montré qu'il était possible de reconstruire la fonction de Green même lorsque les sources n'entourent pas le milieu, pourvu que le milieu soit multidiffusant. Dans ce cas, les diffuseurs présents dans le milieu agissent comme sources secondaires.

Dans la section 2.4.1, nous avons vu qu'il a été établi en sismologie que la fonction de Green pouvait être reconstruite à partir de corrélation de bruit. Il n'y a dans ce cas aucune source clairement identifiée, mais plutôt un bruit diffus continu. Ce bruit peut être décrit comme un ensemble de sources inconnues distribuées au hasard dans le milieu. Ces sources génèrent en permanence du bruit blanc non corrélé ($n_C(t)$). Or, la corrélation résultant des récepteurs A et B est :

$$\sum_C \sum_{C'} h_{AC}(-t) \otimes n_C(-t) \otimes h_{C'B}(t) \otimes n_{C'}(t). \tag{2.4}$$

Si la durée d'observation ΔT est nettement plus longue que le temps de corrélation du bruit, l'expression $n_C(-t) \otimes n_{C'}(t)$ converge vers $\delta(t)\delta(CC')$. De plus, si les sources de bruit sont distribuées partout dans le milieu, elles peuvent exciter chaque mode indépendamment, ce qui aboutit à l'équipartition. On voit que l'équation 2.4 se réduit alors à l'équation 2.3, ce qui prouve qu'il est possible de reconstruire la fonction de Green à partir de la corrélation.

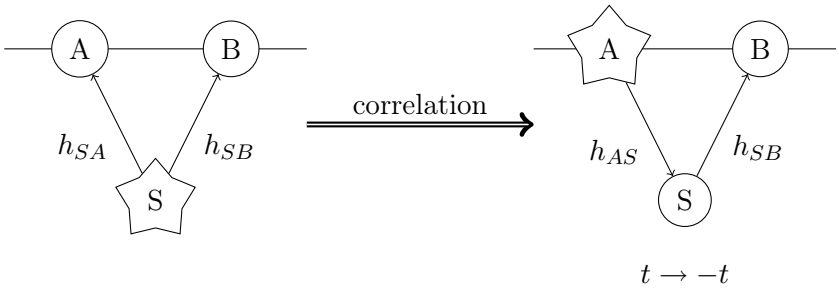

FIG. 2.4 – à gauche : corrélation des signaux enregistrés en A et B. Cette opération est équivalente à (à droite) : émettre une pulsation en A, l'enregistrer en S, la renverser en temps, la réémettre et l'enregistrer en B.

2.5 Bruit Sismique Ambiant

En sismologie 'classique', on n'utilise que les signaux des séismes. Toutefois, comme nous l'avons indiqué dans le chapitre 1, l'activité sismique sur la Terre n'est pas répartie uniformément. Certaines régions présentent une activité sismique quasi nulle et sont, par conséquent, difficiles à étudier à l'aide des méthodes classiques. En plus, on ne connaît jamais à l'avance le moment et le lieu des séismes. Afin d'accumuler suffisamment de signaux utiles, des réseaux sismiques doivent parfois rester déployés pendant de nombreuses années.

Dans la section précédente, nous avons vu qu'un champ d'onde aléatoire, tel que ce bruit sismique ambiant, peut être utilisé pour reconstruire la fonction de Green

d'un milieu. Idéalement, les sources de bruit devraient entourer les récepteurs utilisés pour la corrélation. Par conséquent, il est important de connaître l'origine du bruit. Un certain nombre d'études ont été faites dans le passé [Friedrich et al., 1998; Nishida et al., 2002; Stehly et al., 2006] pour tenter de caractériser le bruit sismique ambiant. On sait depuis au moins Gutenberg [1936] que l'intensité du bruit évolue avec l'activité meteorologique et l'intensité de la houle océanique. Friedrich et al. [1998] ont trouvé que la majeure partie de l'énergie du bruit est contenue dans les ondes de surface. Ces observations suggèrent que le bruit est généré à la surface de la Terre, plus spécifiquement dans les océans.

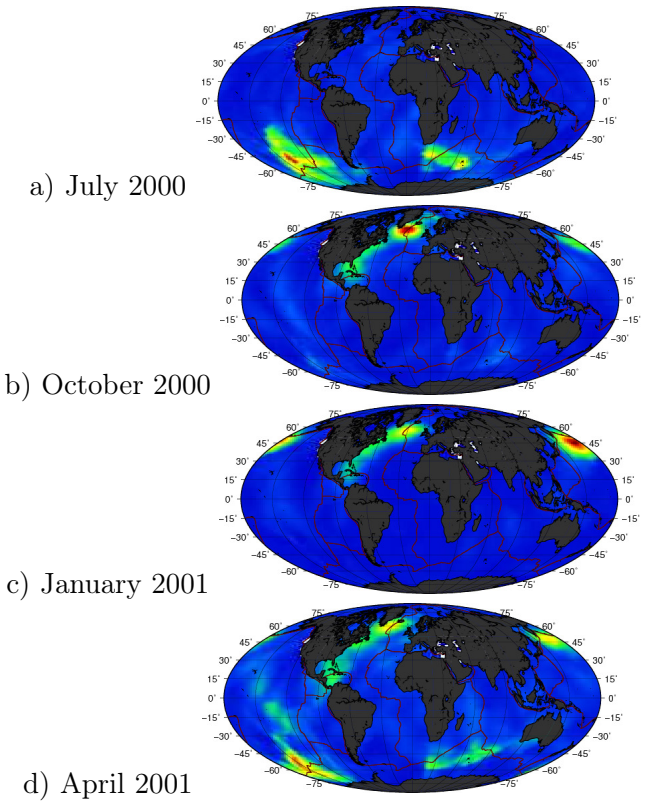

a) July 2000

b) October 2000

c) January 2001

d) April 2001

Fig. 2.5 – Variation saisonnière des sources de bruit (ondes P) dans le pic microsismique sécondaire [0.1 0.3]Hz. De Landès et al. [2010].

Un spectre typique de bruit sismique ambiant est représenté dans figure 2.6. L'origine du bruit est liée à la fréquence [Bonnefoy-Claudet et al., 2006] :

– Pour des fréquences supérieures à 1 Hz, le bruit résulte essentiellement de l'activité humaine, comme la circulation, les usines.

– Enfin, sur la figure 2.6 on peut voir que l'essentiel de l'énergie du bruit se concentre dans la période de 5–20 secondes. Cette partie du spectre présente deux pics, l'un très distinct à 7 s, l'autre moins à 14 s. Ces pics, dénommés 'pics microsismiques primaire et secondaire', sont liés à l'activité de la houle océanique. La fréquence

du pic primaire à 14s correspond à la fréquence dominante des vagues océaniques. La période du pic secondaire est exactement la moitié de celle du pic primaire. Longuet-Higgins [1950] suggèrent que le bruit à 7 s a pour origine les différences de pression sur le fond de l'océan, résultant de l'interaction non linéaire des vagues océaniques.

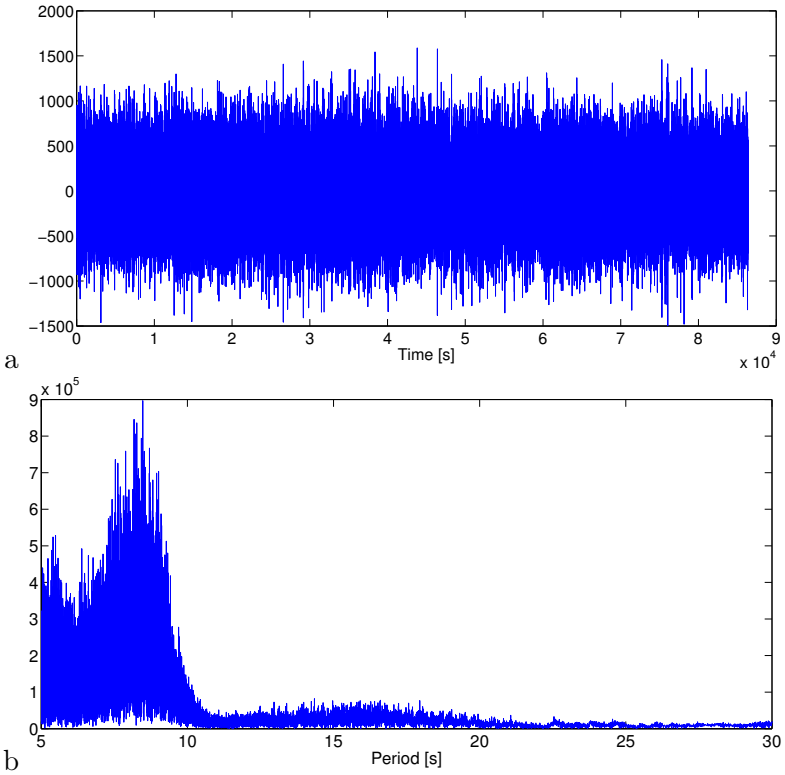

FIG. 2.6 – (a) Enregistrement d'une journée (le 15 janvier 2005) de bruit de fond sismique par la station BFO en Allemagne. (b) Transformée de Fourier de ce même enregistrement. Le pic de 7 secondes domine le spectre, le pic de 14 s est plus modéré.

Stehly et al. [2006] ont montré que le bruit ambiant pour des périodes d'environ 5 – 10 secondes est directif et stable dans le temps. Le bruit pour des périodes plus longues (10 – 20 secondes et 20 – 40 secondes) est moins directionnel mais présente de fortes variations saisonnières. Pour des périodes plus longues, Landès et al. [2010] ont confirmé ce résultats en utilisant les ondes P pour localier les sources de bruit sismique. Ils ont trouvé que le bruit à 10 – 20 secondes est générée par des sources localisées correspondant aux tempêtes océaniques (voir figure 2.5).

Nous savons que ce type de distribution de source anisotrope n'est pas idéale pour la reconstruction de la fonction de Green par intercorrélation. Néanmoins, des études ont montré que les arrivées directes et les ondes de surface dans ces fonctions de corrélation sont suffisamment bien reconstruites pour l'utilisation en imagerie (par exemple Shapiro et al. [2005]).

En outre, il a été suggéré que la coda de la fonction de Green était partiellement reconstruite dans les intercorrélations de bruit. Le raisonnement utilisé est que, si la coda des intercorrélations contenaient de l'information physique, elle pourrait être corrélée à nouveau avec succès. Ce test a été effectué par Stehly et al. [2008], qui ont montré que la corrélation de la coda de la corrélation ('C^3') permet de remonter aux arrivées directes.

Les avantages d'utiliser les inter-corrélations de bruit au lieu des signaux de tremblements de terre sont nombreux. L'inter-corrélation de bruit permet d'extraire les fonctions de Green entre deux stations sismiques. La nouvelle possibilité de résolution d'image ne dépend plus de la distance entre séisme et station, mais de la distance entre stations. Une fois que l'objectif de l'imagerie est connu, on peut concevoir un réseau sismique en fonction des critères spécifiques.

De plus, nous pouvons calculer les fonctions de Green *quand* nous le souhaitons. Cela ouvre des possibilités dans le contrôle sismique dont nous parlerons dans le chapitre suivant.

Chapitre 3

Théorie : Monitoring

Contents

3.1 Changement de Vitesse 17
3.2 Méthode des Doublets 18
3.2.1 Utilisation de Corrélations de Bruit 20
3.3 Méthode de Stretching 21

3.1 Changement de Vitesse

En partant de l'imagerie utilisant les inter-corrélations, voyons si nous pouvons mesurer un *changement* du milieu. Dans ce travail, nous nous intéresserons principalement aux changements dans la vitesse de propagation sismique.

Suivre de minuscules changements dans les propriétés de la croûte peut conduire à une meilleure compréhension des processus dynamiques en jeu dans les séismes et les failles. Historiquement, la recherche de faibles changements crustaux comme précurseurs d'un tremblement de terre a motivé l'étude des changements de vitesse sismique.

Chaque sismogramme contient des informations relatives aux propriétés élastiques du milieu traversé. Considérant deux sismogrammes ayant pour origine la même source et enregistrés par le même récepteur, toute différence entre les deux ne peut être due qu'à des changements dans les propriétés crustales.

Un changement global dans la vitesse de propagation dans le milieu se traduira par de minuscules glissements de phase dans la forme d'onde. Dans le schéma (figure 3.1), l'onde 'rouge' a traversé la première un milieu donné. A un moment ultérieur, après une légère augmentation de vitesse, l'onde 'noire' va passer. L'onde noire se déplacera dans le milieu moins vite que l'onde rouge, ce qui aura pour conséquence d'étirer la forme d'onde. L'axe de temps de la forme d'onde noire se compare à celle de l'onde rouge comme $t(1 + dV/V)$, où dV/V représente le changement relatif de vitesse.

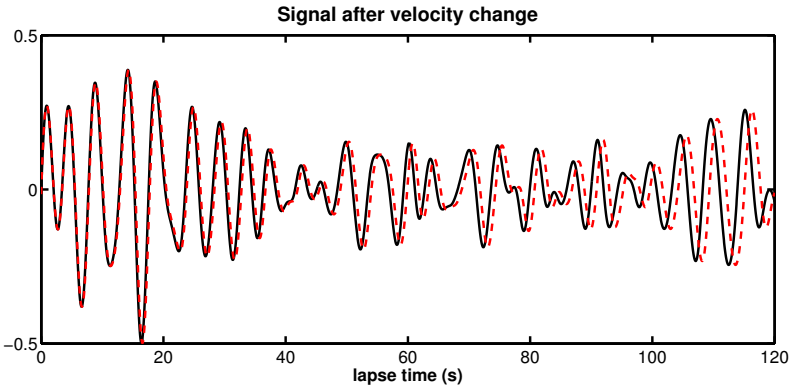

FIG. 3.1 – Un signal avant (rouge) et après (noir) un changement de vitesse dans le milieu.

Le changement de vitesse de propagation entraîne des retards de phase légers au bout d'un court instant, et plus importants pour des temps de trajet plus grands. Autrement dit, plus le champ d'onde passe de temps dans le milieu, plus l'effet de retard de phase sera prononcé et plus il sera facile à mesurer. C'est pourquoi nous pouvons tirer avantage du processus de diffusion décrit en section 2.2. La durée de la propagation dans le milieu des ondes diffusées de la coda est longue. Par consequent, la coda a accumulé plus de retard, a cause d'une vitesse d'onde plus faible, que les ondes directes.

Une façon de mesurer un changement de vitesse est de comparer un signal qui corréspond à la situation initiale (le signal de *référence*) au signal enregistré après le changement. Ces signaux peuvent soit être d'origine active (p.ex. séismes, explosions), où passives (corrélations de bruit). Une discussion de ces possibilités suit dans la section 3.2). Il existe principalement deux méthodes pour mesurer les changements de vitesse 'a partir de la forme d'onde : la méthode des *doublets* (qui sera traité dans section 3.2) et la méthode de *stretching* (section 3.3).

3.2 Méthode des Doublets

Dans le passé, on a pu mesurer des changements dans les propriétés crustales grâce à des signaux de séismes répétés présentant des formes d'onde presque identiques. Ces séismes qui se produisent au même endroit, avec le même mécanisme à la source, à des dates différentes, sont couramment appelés 'doublets'. A partir de ces séismes répétés, Poupinet et al. [1984] ont élaboré une méthode pour mesurer les changements de vitesse dans le milieu en recherchant les différences entre les deux formes d'onde.

On compare le signal à une référence qui correspond à l'état initial. Dans ce qui suit, 'référence' désigne l'état initial et 'signal' le signal modifié à un moment ultérieur.

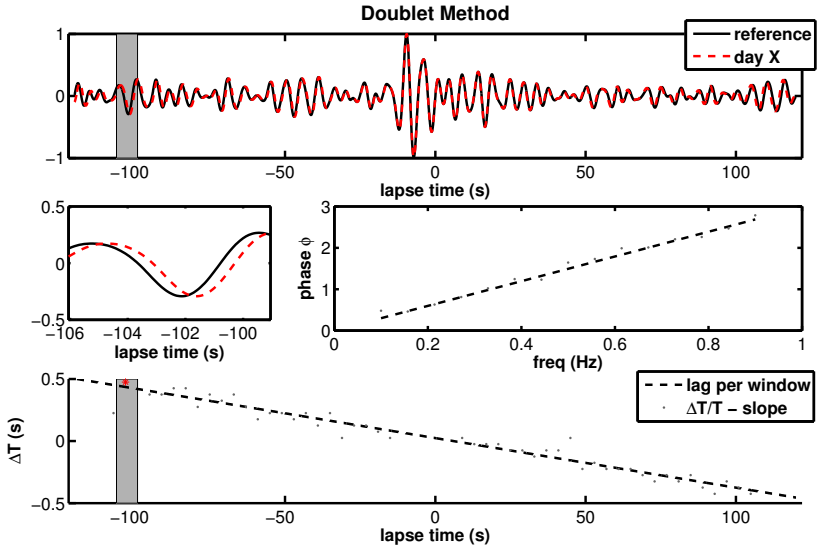

FIG. 3.2 – Illustration de la méthode de doublets. En haut : le signal de réference (noir) et le signal comparé (rouge). La partie grise est agrandi au centre. Centre, à droite : régression linéaire dans la distribution de phase et fréquence. En bas : relation linéaire entre le delai et le temps de trajet.

Une fenêtre mobile d'une longueur d'environ 2 périodes est translatée le long du signal. Dans chaque fenêtre, on calcule le délai du signal par rapport à la référence.

On peut mesurer ce délai δt dans le domaine temporel par le pic de corrélation entre les deux signaux. Cependant, il est généralement plus exact de mesurer le décalage de temps dans le domaine fréquentiel. Il suffit de calculer le inter-spectre :

$$S(f) = A_2 * (f) A_1(f) \tag{3.1}$$

où A_1 et A_2 sont les transformées de Fourier du signal fenêtré dans le temps, et $*$ représente le conjugué complexe. Le retard, exprimé en phase, de chaque fréquence peut être dérivé directement de cet inter-spectre. Pour un décalage de temps δt, la transformé de Fourier du signal est multiplié par $\exp^{i\omega\delta t} = \exp^{i\phi}$. Il existe donc une relation linéaire entre la phase ϕ et le décalage : $\phi = \omega\delta t$. Ainsi, pour déterminer le delai, on peut ajuster une régression linéaire à la distribution en fréquence et délai mesurée (voir figure 3.2, au centre). Cette façon de mesurer le délai permet une résolution temporelle supérieure au pas d'échantillonnage [Poupinet et al., 2008].

Une fois que l'on a déterminé le délai pour chaque fenêtre de temps, on peut le tracer

en fonction du temps de trajet, voir figure 3.2 (en bas). Comme nous l'avons vu dans la section 3.1, dans le cas d'une variation homogène de vitesse le retard temporel du champ d'onde augmente linéairement avec le temps de trajet. Pour extraire la variation de vitesse relative entre le signal et la référence, il suffit donc de calculer la pente de cette distribution délai – temps de trajet : $dt/t = -dV/V$.

Au commencement, les signaux utilisés avec cette méthode étaient ceux de doublets sismiques. L'utilisation de tels doublets présente cependant plusieurs inconvénients.

Tout d'abord, les critères que doit remplir une paire de séismes afin de pouvoir être utilisée pour la recherche de variations sont stricts : ils doivent avoir lieu au même endroit, avec le même mécanisme à la source. On peut difficilement établir si l'on a affaire à une réelle paire de séismes, une relocalisation très précise étant primordiale.

De telles paires de séismes sont extrèmement rares, et quand elles se produisent il s'agit souvent d'évènements de faible magnitude. Il est encore plus rare qu'elles conviennent à l'étude d'effets cosismiques, c.a.d. qu'il s'agisse d'un doublet avec un évènement avant et un après le séisme de grande magnitude.

Enfin, les doublets sismiques présentent la même limitation que tous les autres séismes en ce sens qu'ils ne se produisent que dans les régions actives sismiquement. Cela restreint fortement les régions où il est possible d'appliquer la méthode des doublets.

Une autre façon d'obtenir des sources répétées parfaitement similaires est de procéder de façon active en utilisant des sources artificielles, comme les explosions [Li et al., 2007]. Cette technique est cependant très onéreuse et difficile à mettre en œuvre en terrain difficilement accessible. En plus, la puissance disponible, doc le volume échantillonée, est très limitée.

3.2.1 Utilisation de Corrélations de Bruit

Grâce aux corrélations de bruit, nous pouvons construire nos propres fonctions de Green indépendamment de la survenue de séismes. Chaque récepteur/capteur devient une source virtuelle, répétitive. La méthode des doublets s'applique de la même façon à ces 'sismogrammes virtuels'.

Par exemple, on peut corréler le bruit accumulé durant un mois pour obtenir une bonne fonction de Green. Cette opération est répétée pour le bruit accumulé le mois suivant, ce qui donne une autre fonction de Green. Si le milieu n'a pas subi de modification au cours de ces deux mois, les signaux seront identiques. Cependant, s'il s'est produit une modification, cela s'exprimera par un léger changement dans

la forme d'onde. La comparaison des fonctions de Green correspondant à des dates différentes permet de détecter de tels changements dans le milieu. Nous verrons que la convergence vers la fonction de Green n'est pas requis en pratique (voir chapitre 5).

3.3 Méthode de Stretching

Une autre façon de mesurer les variations de vitesse relative est d'appliquer la méthode de *stretching* décrite p.ex. par [Lobkis and Weaver, 2003; Sens-Schönfelder and Wegler, 2006].

Dans cette méthode, on utilise toute la partie coda de la corrélation. La fenêtre temporelle utilisée commence après les arrivées directes et les ondes diffusées localement, et s'étend idéalement jusqu'au point où la coda disparaît dans le bruit de fond. En supposant qu'un signal a subi un changement de vitesse globale dV/V, il aura subi, par rapport à la référence, un étirement ou une compression d'un facteur $t(1 \pm \varepsilon)$, ou $\varepsilon = dV/V$.

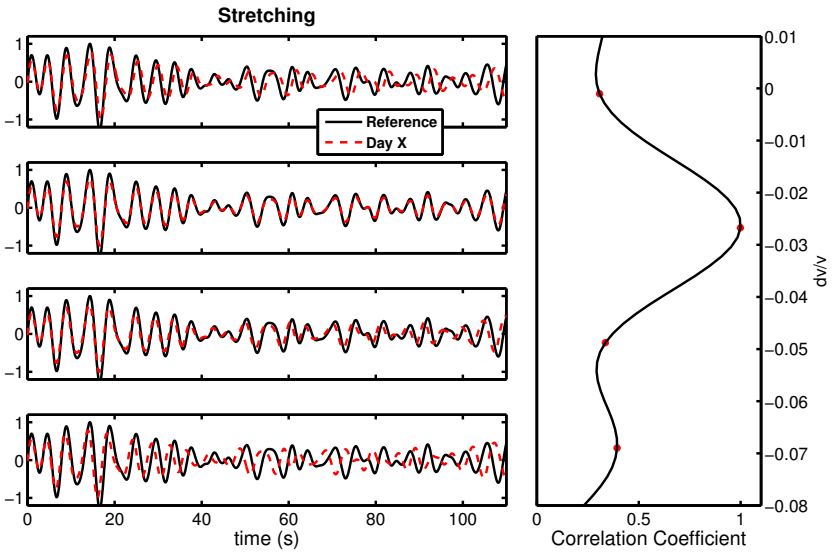

FIG. 3.3 – Illustration de la methode de stretching. A gauche : le signal (en rouge) est etiré pour differentes valeurs de ε. Le coefficient de correlation du signal et la reference (en noir) sont calculés pour chaque test (a droite).

Pour extraire la valeur correcte de dV/V, on interpole toute la fenêtre temporelle du signal en question à $t(1+\varepsilon)$, pour diverses 'valeurs test' de ε. Pour chaque valeur de ε, on calcule le coefficient de corrélation entre le signal étiré $h[t]$ et la référence

$h_0[t]$.

$$CC(\varepsilon) = \frac{\int_{t_1}^{t_2} h\left[t(1-\varepsilon)\right] h_0[t]dt}{\sqrt{\int_{t_1}^{t_2} h^2\left[t(1-\varepsilon)\right] dt. \int_{t_1}^{t_2} h_0^2[t]dt}}, \tag{3.2}$$

ou t_1 et t_2 sont le début et la fin de la coda utilisé.

Le coefficient de corrélation va augmenter au fur et à mesure que la valeur de ε approchera la valeur exacte de dV/V, pour atteindre un maximum quand elles sont parfaitement égales, et décroître lorsque la valeur test de ε dépasse la valeur exacte dV/V. Le changement de vitesse réel correspond au facteur d'étirement ε pour lequel le coefficient de corrélation est maximal.

Si les formes d'onde de la référence et du signal étiré sont exactement les mêmes, le coefficient de corrélation maximum obtenu aura la valeur 1. Une valeur du coefficient de corrélation $CC < 1$ reflete un changement des sources de bruit ou des diffuseurs dans le milieu.

Dans le chapitre suivant, j'appliquerai les méthodes décrites ci-dessus à des données sismologiques afin d'évaluer si un changement peut être observé sur une zone de faille active - celle de Parkfield, Californie.

Chapitre 4

Parkfield I : Velocity monitoring on an active fault zone

Contents

4.1 Summary 23
4.2 Postseismic relaxation along the San Andreas fault 25
4.3 Introduction 25
4.4 Data Used 26
4.5 Noise correlation Processing 26
4.6 Stability of noise correlation 28
4.7 Clock Corrections 28
4.8 Velocity Variation Measurement 29
4.9 Results 30
4.10 Non-volcanic Tremor 33
4.11 Conclusion 34
4.12 Questions Raised 34

4.1 Summary

In this chapter, the methods described in chapter 3 are applied to seismological data. The objective is to evaluate velocity changes in the Earth's crust by using ambient noise correlations. In the first place, we need to choose a place and a time where we expect a change to occur. An obvious case would be an active fault zone, with an earthquake occurring during the measurements. Prior studies using active methods (such as explosions or doublet earthquakes) have observed velocity changes in such cases. Most studies observe postseismic velocity increases of the order of $\sim 1\%$ after large seismic events.

Poupinet et al. [1984] use doublet earthquakes to measure a 0.2% S-wave velocity decrease associated with the 1979 M5.9 Coyote Lake earthquake. On the Landers, California fault zone, Li et al. [1998] measure a 0.5% to 1.5% increase in seismic

velocity during the period following the 1992 M7.2 Landers earthquake. Later, the velocity increase is reversed as the 1999 M7.1 Hector Mine event occurs 20 km away [Vidale and Li, 2003]. Similarly, Li et al. [2007] find a 2.5% decrease occurred in seismic velocity between recordings before and after the 2004 M6.0 Parkfield event, followed by a $\sim 1\%$ postseismic velocity increase in the next 4 months. Using repeated explosions, Nishimura et al. [2005] find the S-wave velocity decreases by $0.3\% - 1.0\%$ in the 15 km region surrounding the 1998 M6.1 Iwate event hypocenter.

These velocity decreases, which seem to be coseismic, are generally associated with stress changes or damage in the fault zone. After the event, as the stress is slowly recovering after the earthquake stress drop, the velocity gradually recovers to the original level.

One drawback of the active techniques used in these studies is that they only give us a snapshot of the situation with irregular sampling in time. The use of ambient noise correlations could allow us to follow the continuous evolution of the velocity changes in a fault zone.

To measure velocity changes with ambient noise correlation, we need an active fault zone with continuous measurements of the ambient noise. Parkfield, California is a good candidate for this, as it is among the most instrumented regions worldwide.

Since 1857, six earthquakes of at least M6 have occurred on the section of the San Andreas fault near Parkfield. In 1985, the USGS predicted another M6 event would occur at Parkfield by 1993 [Bakun and Lindh, 1985]. In an effort to capture as much information as possible of this event, the area was heavily instrumented as part of the Parkfield Prediction Experiment (PPE). When the earthquake finally occurred in 2004, it was recorded by creepmeters, GPS, strainmeters, magnetometers, pore presssure sensors, and finally an array of 13 borehole seismometers. This makes the 2004 Parkfield event into one of the best recorded and consequently most studied earthquakes ever.

In the following, we apply noise correlation monitoring to the Parkfield data and observe a coseismic velocity drop of 0.1% for the Parkfield event, as well as a 0.04% drop coinciding with the San Simeon event some 50 km away. The velocity recovery after the Parkfield event follows the trend of GPS measurements closely, indicating tectonic reloading.

The apparent correlation to non-volcanic tremor measurements in the area suggests that the velocity change observed is linked to a phenomenon occurring deeper than superficial fault zone damage.

4.2 Postseismic relaxation along the San Andreas fault at Parkfield from continuous seismological observations

Authors :
F. Brenguier, M. Campillo, C. Hadziioannou, N.M. Shapiro, R.M. Nadeau, E. Larose

Abstract

Seismic velocity changes and non-volcanic tremor activity in the Parkfield area in California reveal that large earthquakes induce long term perturbations of crustal properties in the San Andreas fault zone. The 2003, San Simeon and 2004, Parkfield earthquakes both reduced seismic velocities measured from correlations of the ambient seismic noise and induced an increased non-volcanic tremor activity along the San Andreas fault. Following the Parkfield earthquake, velocity reduction and non-volcanic tremor activity remained elevated for more than three years and decayed over time similarly to afterslip derived from GPS measurements. These observations suggest that the seismic velocity changes are related to coseismic damage in the shallow layers and to deep co- and postseismic stress relaxation within the San Andreas fault zone.

4.3 Introduction

Information about the stress variations in deeper parts of continental faults can be obtained by studying source properties of micro earthquakes [Allmann and Shearer, 2007]. Changes in seismic velocities measured using repeated natural and active seismic sources can also provide information about rock damage and healing at depth after large earthquakes [Vidale and Li, 2003; Li et al., 2003] or about stress changes in seismogenic zones [Niu et al., 2008]. The main limitation of these types of measurements, however, are the episodic nature of their seismic sources, which prevents continuous monitoring of crustal properties.

Here we use continuous measurements of ambient seismic noise to recover continuous variations of seismic velocities within the crust along the San Andreas Fault (SAF) near Parkfield, CA. With this approach the cross-correlation function of ambient seismic noise computed between a pair of receivers converges toward the response

of the Earth between the receivers (the so-called Green's function) [1]. Essentially this function represents the seismogram that would be recorded at one of the receivers if a source were acting at the second [Shapiro et al., 2005; Campillo, 2006]. The temporal evolution of the crust is then tracked by computing cross-correlation functions at different dates for the same receiver pair and measuring the changes between the correlation functions [Sens-Schönfelder and Wegler, 2006; Wegler and Sens-Schöenfelder, 2007; Brenguier et al., 2008b].

4.4 Data Used

To monitor variations in seismic velocity along the San Andreas fault at Parkfield, we used more than 5 years of continuous seismic noise data recorded by 13 short-period seismological stations of the Berkeley High Resolution Seismic Network [2]. These stations are installed in boreholes at depths of 60 to 300 m, thus reducing locally generated noise and effects of temperature variations and precipitation (figure 4.1).

We analyzed data from January 2002 to October 2007, spanning the times of two major earthquakes that occurred within a 100 km radius of Parkfield : the $M_w = 6.5$ San Simeon Earthquake of 22 December 2003 whose epicenter was located 60 km west of Parkfield and the $M_w = 6.0$ Parkfield Earthquake of 28 September 2004. For every possible pair combination of stations we computed the daily cross-correlation of seismic noise using the procedure of Brenguier et al. [2007], yielding 91×2140 days $= 194,740$ cross-correlation and auto-correlation time functions. A *Reference Green function* (RGF) was computed for each station pair by stacking the daily cross-correlations for the entire 2140 day period.

4.5 Noise correlation Processing

We first select the seismic data by 24-hour intervals and clip the amplitudes above 10 times the average rms amplitude as a first step to avoid time localized strong energetic signal principally due to earthquakes. We then apply spectral whitening between 0.08 and 2.0 Hz and one-bit normalization in the time domain in order to converge toward a stationary data set. We finally correlate these 24-hour interval time series for every possible receiver pair [Bensen et al., 2007; Brenguier et al., 2007]. Most of the contribution by earthquakes and tremors is removed by this

[1] Since this paper was published, we have realized that the correlations functions have not yet converged to the Green's function. See chapter 5

[2] More details concerning the Parkfield HRSN can be found at `http://seismo.berkeley.edu/bdsn/hrsn.overview.html`

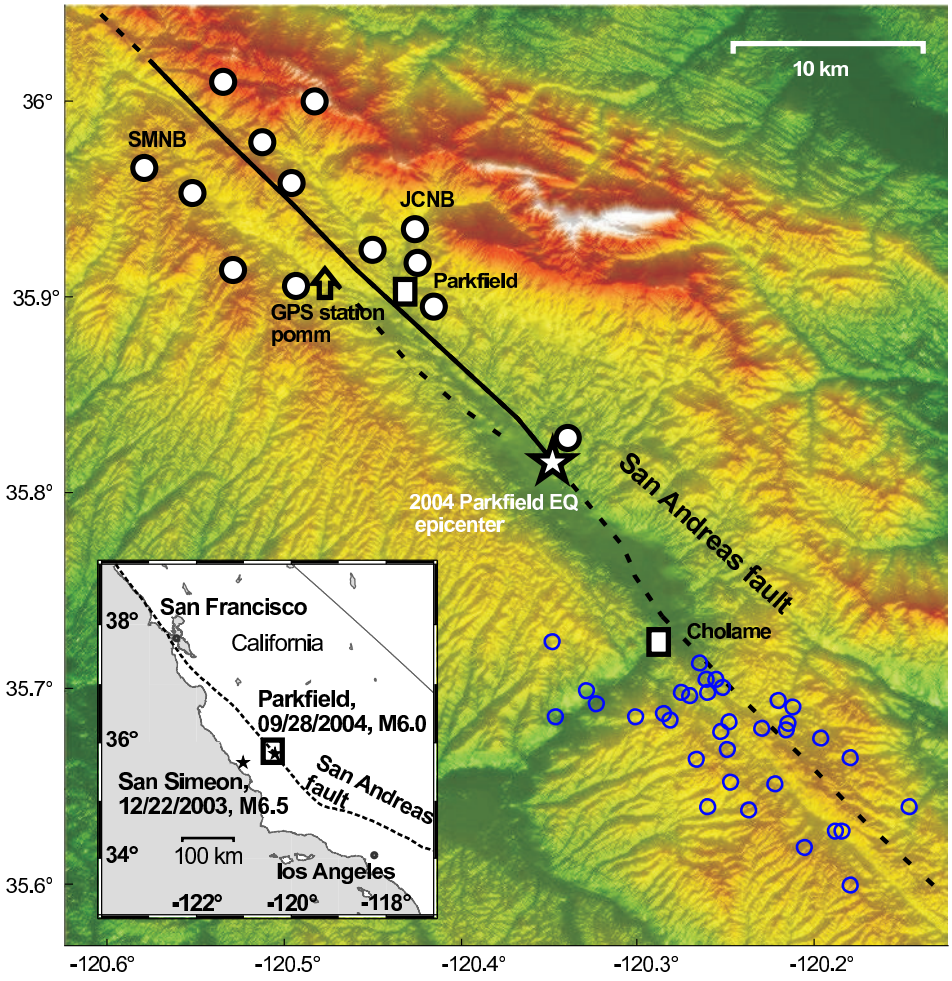

FIG. 4.1 – Location of the High Resolution Seismic Network (HRSN, white and black circles) near Parkfield, California and location of the 2003, San Simeon and 2004, Parkfield earthquakes. The black solid line indicates the surface projection of the 2004 Parkfield earthquake rupture and afterslip extent. The blue circles indicate the epicenters of non-volcanic tremors detected by Nadeau and Dolenc [2005]. The black box on the inset figure corresponds to the studied area. The digital elevation model (DEM) plot was obtained from the USGS National Map Seamless Server, http://seamless.usgs.gov, and Luis [2007].

processing, as their energy is mostly contained in a higher frequency band than the one considered here.

The current cross-correlation functions are stacked into 30-day stacks while moving the stack window by a day at a time. The reference cross-correlation functions are stacked over the all time period. In order to retrieve high signal to noise ratio reference stacked cross-correlation functions, we only select correlation functions for which the average energy of the reconstructed direct waves is 1.5 times higher than the average energy of the noise part of the correlation functions. By this procedure, we reject 74 % of the cross-correlation functions. The details of the relative velocity change measurements is described in Brenguier et al. [2008b] and in section 3.2.

4.6 Stability of noise correlation

We analyze the stability of the correlations with the date d over the 2002-2007 period range. For each set of N = 30 consecutive days (time window centered around the date d) and each couple of stations, we process the N correlations (one for each day) and then evaluate the remnant level of fluctuations :

$$\sigma(d,\tau) = \sqrt{\frac{\langle C^2(\tau)\rangle - \langle C(\tau)\rangle^2}{N-1}} \tag{4.1}$$

where $\langle . \rangle$ represents an average over N sub-records. We estimate a Signal to Noise ratio (SNR) for the correlation functions by comparing the mean amplitude of the average correlations (30 days moving window averaging) to this level of fluctuation (figure 4.2). The strong increase in SNR in 2003 corresponds to an increase of + 20 dB of the seismic station pre-amplification gain.

Correlations are found to be quite stable over the entire period of interest, and fluctuations show a relative amplitude that arbitrarily varies between 10 % and 20 %. This means that at least 93 % of the energy of the correlations is stable for a 30 day moving window average, which can be interpreted in terms of spatial and temporal noise structure stability. It is worth noting that the fluctuation level is not correlated with the measured evolution of velocity changes.

4.7 Clock Corrections

The 30-day stacked correlations shown in figure 4.3A exhibit variations due to the seasonal pattern of the location of noise sources [Stehly et al., 2006; Kedar and

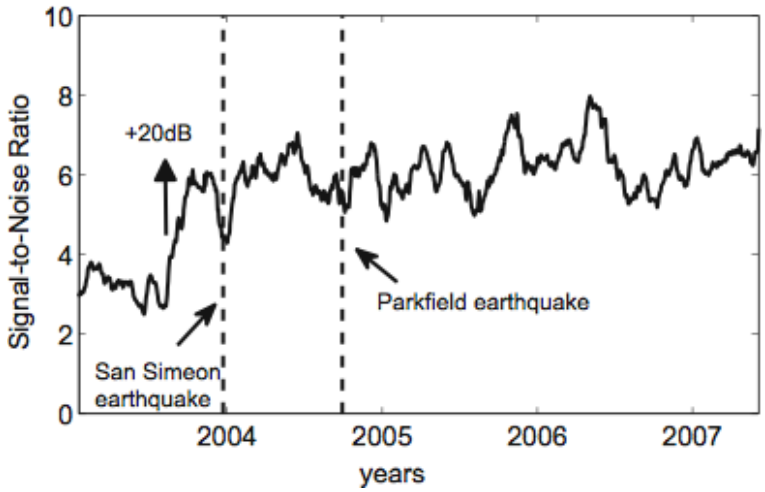

FIG. 4.2 – Correlation function Signal to Noise Ratio (SNR) averaged over SNR's calculated for all receiver pairs used in the analysis of seismic velocity changes. The arrow indicating + 20 dB corresponds to the seismic station pre-amplification gain.

Webb, 2005]. Because these seasonal variations mainly affect the direct waves, we did not make differential time measurements for these waves. We also investigated the accuracy of the station clocks by analyzing the temporal symmetry of the correlation functions [Stehly et al., 2007] and correcting for the detected errors (section **??**).

We extended the procedure described in Stehly et al. [2007] to detect clock jumps without reference to a propagation model. After measuring the delays between every pair of stations, an inverse procedure is used to retrieve the individual station corrections. We found several jumps that are as large as 30 ms. They are not simultaneous with the main changes of velocity associated to the occurrence of the San Simeon and Parkfield earthquakes. We correct these clock jumps by shifting the correlation functions and performing a new doublet analysis.

Finally, following Brenguier et al. [2008b], we averaged the measured time shifts for each time τ over all station pairs to increase the measurement accuracy.

4.8 Velocity Variation Measurement

The velocity changes were determined by measuring time delays between the RGF and 30-day stacks of cross-correlation functions in the frequency range, [0.1-0.9] Hz [Poupinet et al. [1984]; Brenguier et al. [2008b] ; section 3.2, figure 4.3B]. If the medium experiences a spatially homogeneous relative seismic velocity change $\Delta V/V$, the relative travel time shift $(\Delta\tau/\tau)$ between a perturbed and reference Green function is independent of the lapse time (τ) at which it is measured and

$\Delta V/V = -\Delta\tau/\tau = \text{const}$. Therefore, when computing a local time shift $\Delta\tau$ between the reference and a chosen cross-correlation function in a short window centered at time τ, we would expect that $\Delta\tau$ should be a linear function of τ. By measuring the slope of the travel time shifts $\Delta\tau$ as function of time τ, we then estimated the relative time perturbation $(\Delta\tau/\tau)$, which is the opposite value of the medium's relative velocity change $(\Delta V/V)$.

4.9 Results

After the San Simeon earthquake, the seismic velocity along the SAF at Parkfield decreased by 0.04% (figure 4.4). This is consistent with measurements using active sources and fault guided waves that are associated to other earthquakes [Vidale and Li, 2003; Li et al., 2003; Rubinstein and Beroza, 2005]. Creepmeter and GPS measurements show that there was no significant slip detected along the SAF in the Parkfield area following the San Simeon earthquake [3]. This suggests that the velocity change we detect may be related to coseismic damage in the shallow layers caused by strong ground shaking ($\sim$ 0.15 g) from this quake[4]. By 7 months after the quake, velocities in the Parkfield area appear to have returned to their pre-earthquake levels.

Kinematic and dynamic rupture inversions as well as GPS and INSAR measurements showed that the Parkfield mainshock released a maximum stress of 10 Mpa and that the average slip was about 0.5 m [Ma et al., 2008]. The Parkfield mainshock was also followed by postseismic afterslip that is still ongoing and broadly distributed between the surface and a depth of 12 km [Johnson et al., 2006; Freed, 2007]. Immediately after the Parkfield earthquake, velocities decreased by 0.08% and postseismic velocities remained low for almost 3 years (figure 4.4). The long term decay of the relative velocity perturbation was very similar to the relaxation curve associated with the along-fault displacement deduced from GPS measurements [Johanson et al., 2006; Freed, 2007]. Therefore, our hypothesis is that the evolution of the observed seismic velocity changes after the Parkfield earthquake was governed by the postseismic stress relaxation within deeper parts of the fault zone and the surrounding region.

[3] More details concerning the U.S. Geological Survey (USGS) deformation network at Parkfield can be found at `http://earthquake.usgs.gov/research/parkfield/deform.php`

[4] The apparent correlation with nonvolcanic tremor activity detailed in section 4.10 suggests some influence on processes at greater depths.

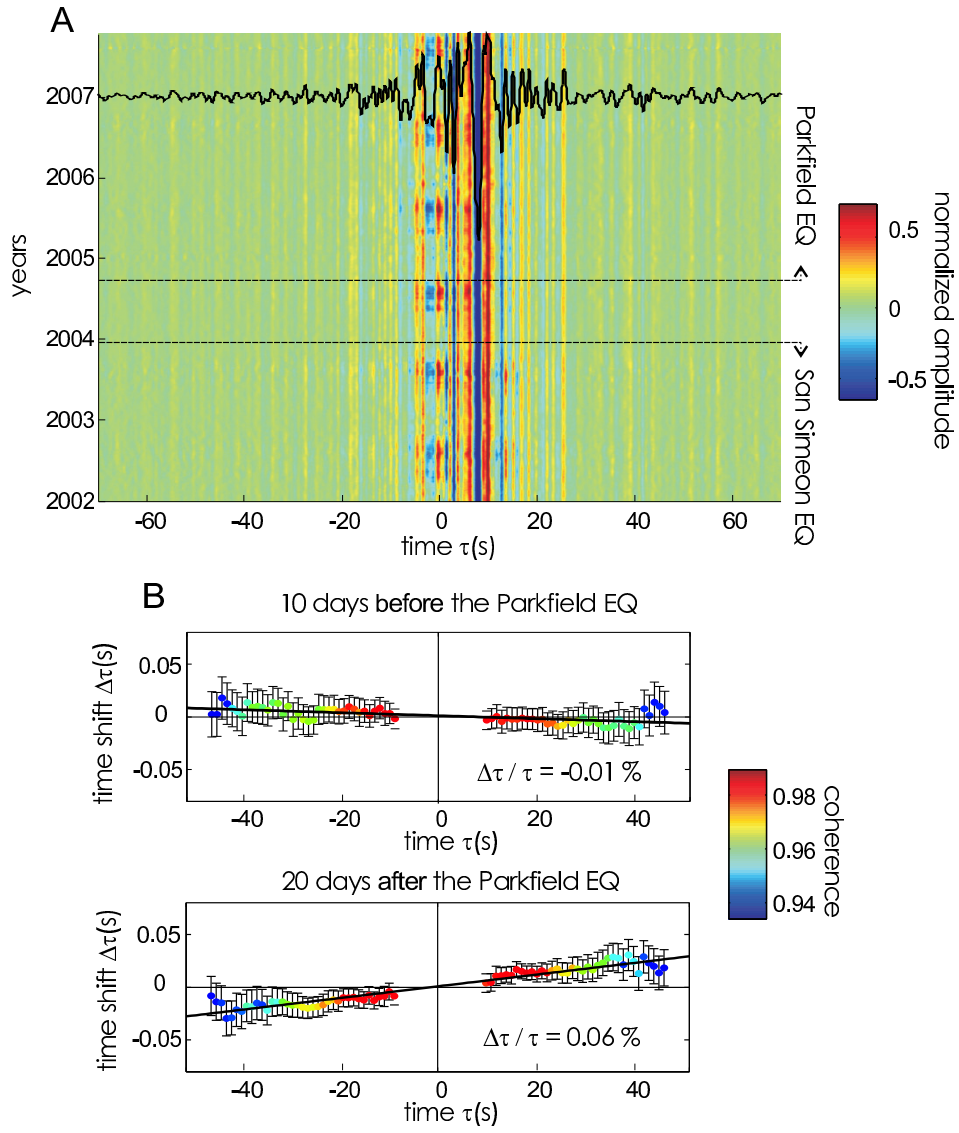

FIG. 4.3 – Relative travel-time change measurements ($\Delta\tau/\tau$). (A) 30 day stacked cross-correlation functions (CCF) for receiver pair JCNB-SMNB. The black curve represents the reference stacked cross-correlation function. The CCFs are filtered between 0.1 and 0.9 Hz and normalized in amplitude. (B) Time shifts averaged over 91 receiver pairs and coherence measured between the reference stacked and 30 day stacked cross-correlation functions (frequency band, 0.1-0.9 Hz).

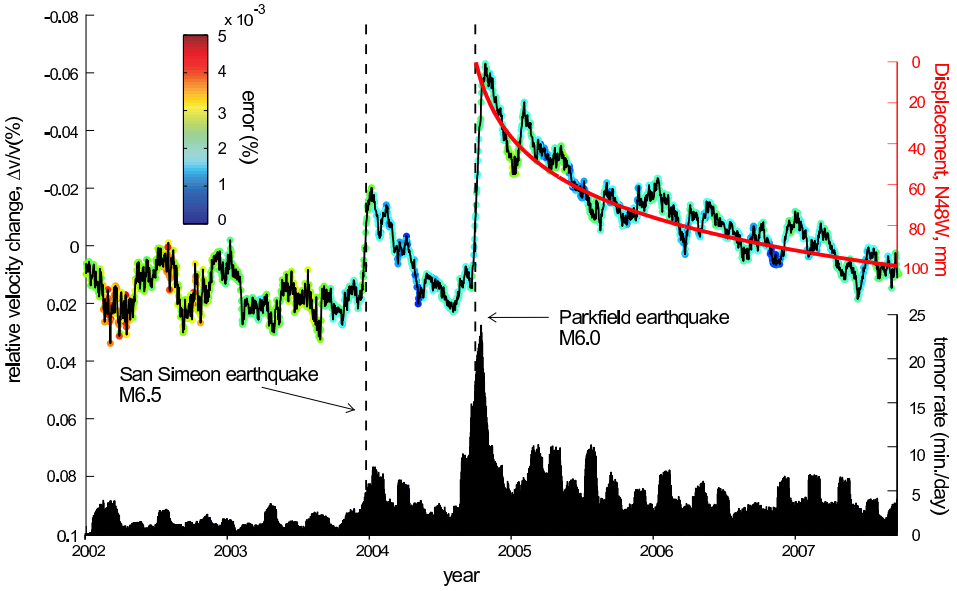

FIG. 4.4 – Seismic velocity changes, surface displacements from GPS and tremor activity near Parkfield. The red curve represents the postseismic fault-parallel displacements along the San Andreas fault as measured by GPS at station `pomm` (figure 4.1). The tremor rates are averaged over a centered 30-day length moving time-window. More details concerning the USGS GPS network at Parkfield can be found at `http://quake.usgs.gov/research/deformation/twocolor/pkf_continuous_gps.html`.

4.10 Non-volcanic Tremor

Detections of nonvolcanic tremor (NVT) in the Cholame-Parkfield region of California are carried out using twenty sample-per-second (sps) continuous data channels from 8 stations of the borehole High Resolution Seismic Network (HRSN) near Parkfield California.

Continuous data amplitudes are first normalized to account for instrument gain differences and then 3 to 8 Hz band-pass filtered. Two sps root mean squared (RMS) envelope seismograms of these data are then generated using a 201 sample boxcar window. Diurnal variations in background noise levels corresponding to cultural activity can often exceed 300 % in the HRSN data. To compensate for this, daily background noise level corrections are applied to each of the RMS seismograms. Noise level corrections for each channel are determined empirically using a 28 day median average correction for each 0.5 second sample of the day, and the corrections are recalculated seasonally to help account for minor seasonal variations that take place.

Following the noise level corrections, RMS seismograms are normalized to the 10 percentile amplitude level for the day being processed. The median amplitudes among the 8 envelope seismograms for each 0.5 second sample are then used to form a time series of amplitude transients (i.e., summary envelope) for the Parkfield-Cholame area. Detections for potential NVTs are then made when summary envelope amplitudes remain 300 % above the 10 % background level continuously for 3 minutes or longer.

The pre-envelope 3 to 8 Hz filtered data were then visually inspected to discriminate between NVT signal and amplitude transient artifacts. The visual inspection requires temporal coherence of secondary amplitude fluctuations among several stations. It also identifies and excludes coherent non-NVT activity such as earthquake swarms, unusual cultural noise signals (e.g., the SAFOD deep drilling project at Parkfield), and occasional multi-station artifacts that can occur during network operations.

Of the 1705 potential detections made for the 2002-2007 period (inclusive), approximately 7.8 % were excluded during the visual inspection, yielding 1577 NVT detections for the region. Also excluded from the analysis are data for the hours of the day following the 22 December 2003, M6.5 San Simeon and 28 September 2004, M6.0 Parkfield California mainshocks and for the entire two days following these events.

Data for these periods was dominated by amplitude transients from 1000 seconds of frequently overlapping aftershock signals making accurate NVT detections difficult.

The total duration of the 1577 NVT detections for the 2002-2007 period was 8962 minutes, with the median and interquartile range of detection duration per event being 4.68 and 3.17 minutes respectively.

Observation of non-volcanic tremors in the vicinity of the Parkfield area supports this hypothesis (figure 4.4). We considered the 30-day averaged rate of tremor activity in the Cholame-Parkfield region computed using continuous records from the HRSN for the period 2002 through 2007. These tremors are estimated to have occurred between 20 and 40 km depth [Nadeau and Dolenc, 2005], similarly to the Episodic Tremor and Slip phenomena on subduction zones [Obara, 2002; Rogers and Dragert, 2003]. There is a clear evidence of triggering of tremor activity by both the San-Simeon and Parkfield earthquakes. Following the Parkfield earthquake, tremor activity remained elevated and has yet to return to its pre-event level similarly to the seismic velocity changes. This observation supports our hypothesis that both seismic velocity changes and tremor activity following the Parkfield EQ are related to postseismic stress relaxation and corresponding slow slip. We also propose that the increased NVT activity following the San Simeon EQ may be related to slow slip at depth in response to small stress variations induced by the passing of seismic waves from the M6.5 event [Rubinstein et al., 2007b].

4.11 Conclusion

Differences in the evolution of seismic velocities following the San Simeon and the Parkfield earthquakes indicate that two different physical mechanisms may be responsible for the changes in crustal properties : 1) damage of shallow layers and fault zone caused by the strong ground shaking and 2) coseismic stress change followed by the postseismic relaxation. These results demonstrate that measuring small velocity perturbations from correlations of seismic noise can be a useful tool for studying the continuous time evolution of the stress regime in the vicinity of seismogenic faults.

4.12 Questions Raised

In this chapter we have seen that it is possible to use the signals generated with ambient noise cross-correlation to monitor velocity changes. The question now arises as to how reliable these measurements are.

One question concerns the temporal resolution : one of the criteria for a cross-correlation to converge to the Green's function is time integration. For this reason, averages over 30 days of noise were used in the study. However, this limits the

temporal resolution of the velocity change measurements. Is the observed velocity drop exactly coseismic or not ? In chapter 7, an improvement on the resolution is presented.

Another criterion for convergence is the isotropic distribution of noise sources. However, on the Earth, and at the frequencies used, the noise is primarily generated by oceanic waves (section 2.5). These oceanic sources are spatially localized, and moreover change during the year. The effect of this seasonal variation is visible in figure 4.3, where the direct waves of the cross-correlation vary in amplitude over the course of the years. From this, it is clear that the signals used have not converged completely to the Green's function. Regardless, it seems possible to use these signals for monitoring purposes. In the next chapter, I use laboratory experiments to investigate the limits of using a cross-correlation function which is deliberately not equal to the GF, specifically for the application to monitoring.

Chapitre 5

Laboratory experiments : Testing the limits of monitoring

Contents

5.1 Summary **37**
5.2 Stability of monitoring **39**
5.3 Introduction **39**
5.4 Methodology **41**
5.4.1 Motivations for doing analogous laboratory experiments . . . 41
5.4.2 Scattering properties of the medium 42
5.5 Comparison of data processing techniques **43**
5.5.1 Active experiment : high quality data. 43
5.5.2 Active experiment : low quality data 47
5.5.3 Advantages and drawbacks of both techniques 49
5.6 Monitoring with the correlation ? **51**
5.7 Influence of noise source stability **53**
5.8 Discussion and Perspectives **56**
5.9 Calculations **57**
5.9.1 High Quality Data 57
5.9.2 Low Quality Data 59
5.10 Questions Raised **60**

5.1 Summary

In the previous chapter, we have seen that in practice, the Green's function is not completely reconstructed. Even when a cross-correlation is averaged using years of noise, some fluctuations remain around the Green's function. The ratio between these fluctuations and the Green's function amplitude is expected to scale with the square root of the amount of data used in the cross-correlation (see Larose et al. [2004]; Snieder [2004]; Sabra et al. [2005b]). In addition to this limit, the correlation

will never converge completely as there will always be some signature left of the spatial distribution of sources.

Unlike in seismology, in a laboratory experiment the sources, receivers and medium can be controlled and varied independently. In the following, I take advantage of this controlled environment. A laboratory experiment is set up to test the limits of the application of dV/V monitoring techniques using badly reconstructed 'Green's functions'.

Measurements done in an active setup are compared to those done in a passive, or cross-correlation setup. We assume that the Green's function is retrieved in the active case. In the passive case, the noise source distribution is far from isotropic, and the cross-correlation is integrated over a short time. In other words, the cross-correlations calculated in the passive case will deliberately not converge to the Green's function.

The global velocity of the medium is varied throughout the experiment by changing its temperature. While it changes, dV/V measurements are performed on the signals from the active and passive setup. When all the noise sources are kept stable, the velocity change measured using the Green's function and the cross-correlation are practically the same (see figure 5.9). However, when the noise sources are varied from one measurement to the next, the dV/V measurements from the passive case start diverging.

5.2 Stability of Monitoring Weak Changes in Multiply Scattering Media with Ambient Noise Correlation : Laboratory Experiments.

Authors :
C. Hadziioannou, E. Larose, O. Coutant, P. Roux and M. Campillo

Abstract

Previous studies have shown that small changes can be monitored in a scattering medium by observing phase shifts in the coda. Passive monitoring of weak changes through ambient noise correlation has already been applied to seismology, acoustics and engineering. Usually, this is done under the assumption that a properly reconstructed Green function as well as stable background noise sources are necessary. In order to further develop this monitoring technique, a laboratory experiment was performed in the 2.5MHz range in a gel with scattering inclusions, comparing an active (pulse-echo) form of monitoring to a passive (correlation) one. Present results show that temperature changes in the medium can be observed even if the Green function (GF) of the medium is not reconstructed. Moreover, this article establishes that the GF reconstruction in the correlations is not a necessary condition : the only condition to monitoring with correlation (passive experiment) is the relative stability of the background noise structure.

5.3 Introduction

In order to image a complex medium the impulse response, or Green function (GF), of that medium is needed. Classically, the impulse response is retrieved by active means : a signal generated at one point (*e.g.*, an earthquake) is recorded at another (a passive receiver like a seismic station), and this record is treated as the band-pass filtered GF. Over the last fifteen years, developments in helioseismology [Duvall et al., 1993] and in acoustics [Weaver and Lobkis, 2001; Lobkis and Weaver, 2001] showed that information about a medium can be extracted from diffuse (coda) waves or ambient background noise. Since then, seismologists are turning to this *passive imaging* technique [Larose et al., 2006]. In this latter case the seismic coda [Campillo and Paul, 2003] or seismic noise [Shapiro and Campillo, 2004] is correlated to reconstruct the GF, either by averaging over space, time, or both. *Passive imaging* requires some assumptions : one needs uniformly distributed noise sources and/or long enough record duration to get the correlation function to converge to the GF.

Monitoring dynamic media is a separate issue and, as we will see, is based on different (and weaker) assumptions. In the 80's, Poupinet et al. [1984] proposed to use coda waves to monitor velocity changes in scattering media (the after-mentioned *doublet* technique). At first glance, coda waves might appear as a jumbled mess of wave arrivals. In fact, they consist of the waves which have described long, scattered paths through the medium, thereby sampling it thoroughly. As a result, these scattered waves are more sensitive to small variations than the ballistic waves. For this reason, the information in the coda can be exploited to monitor small changes in a medium. This technique, analogous to Diffuse Wave Spectroscopy (DWS, Pine et al. [1988]) in optics, was later named *coda wave interferometry* (CWI, Snieder et al. [2002]). It tracks the tiny phase changes in the coda that are caused by velocity changes in the medium. A major issue of the *doublet* technique is that it requires stable reproducible sources, which are hardly available in seismology. Thus, a more recent idea was to combine noise-based *passive imaging* with the *doublet* technique [Sabra et al., 2006; Sens-Schönfelder and Wegler, 2006; Sens-Schönfelder and Larose, 2008; Brenguier et al., 2008b]. First, one correlates the background noise between two receivers. Second, one analyzes small phase changes at large lapse times (coda) in the correlations. This forms the basis of *passive monitoring* (or passive image interferometry [Sens-Schönfelder and Wegler, 2006]) with seismic noise. Noise based *passive monitoring* seems to simultaneously require two conditions. First : a homogeneous distribution of sources in space, and second : temporal stability of these sources.

In seismology, most of the noise (between 0.01 and 1 Hz) generated in the oceans [Rhie and Romanowicz, 2004; Stehly et al., 2006] shows strong spatio-temporal variabilities. This feature is in favor of *passive imaging* as long as records are long enough (duration of the order of a year) to average over a large distribution of sources. But to *passively monitor* dynamic phenomena over a few days or less, this feature seems very unfavorable. In this paper, we investigate the effect of these non-ideal conditions on the reliability of *passive monitoring*. We will also examine if the GF reconstruction in the correlation is a necessary condition to perform *passive monitoring*. To that end, we test the *passive monitoring* technique under degraded conditions in a controllable (laboratory) environment. In section 5.4 of the present paper, we describe the experimental setup and our motivations to do small-scale seismology. In section 5.5, we compare two different data processing procedures to extract velocity variations from the coda wave. One is the *doublet* technique introduced twenty years ago. The other, referred to as *stretching*, was developed more recently [Lobkis and Weaver, 2003; Sens-Schönfelder and Wegler, 2006; Larose and Hall, 2009]. Advantages and drawbacks of both procedures are discussed. We also investigate the robustness of these procedures when noise is introduced in the signal. In section 5.6, we investigate if *passive monitoring* is still possible when the GF is not properly reconstructed in the correlations. Finally, in section 5.7, we test the robustness of *passive monitoring* in the case of temporally changing distribution of

sources.

5.4 Methodology

5.4.1 Motivations for doing analogous laboratory experiments

	Seismology	Ultrasound
Wavelength	km	mm
Frequency	mHz - Hz	MHz
Total size	10^3 km	m
Total duration	month-year	min

TAB. 5.1 – Comparison of the physical parameters between seismology and ultrasound.

Seismology is based on the observation and processing of natural vibrations. In a passive field experiment where seismic waves originate from earthquakes, scientists are facing two simultaneous problems. They neither know the source location with sufficient precision, the source mechanism nor the medium of propagation. It is therefore very complex to image the source and the medium at the same time. By reproducing some features of the seismic propagation in the lab and employing controlled sources and sensors, we can focus our efforts on the physics of the wave propagation and develop new methods more comfortably. In laboratory-scale seismology, we control for instance the size of the medium, the scattering properties, and the absorption. We are then able to adjust one parameter at a time and test the physical models and imaging techniques we develop. But the main reason for carrying out analogous ultrasonic experiments is more tactical : it is related to the order of magnitude of the physical parameters as recalled in Table 5.1. Ultrasonic wavelengths are on the order of a millimeter, meaning that experiments are physically easy to handle. Additionally, the duration of a single ultrasonic experiment is very short (one minute) compared to seismology where we have to wait for earthquakes (year). This characteristic allows us to achieve many more experiments in the lab, and test many parameters over a wide range of magnitudes. In the view of testing processing technique to monitor weak changes, it is also of first importance to perfectly control the origin of the change in the medium. This is quite convenient in the laboratory, but almost impossible in a natural environment. These are the reasons why several seismology laboratories have decided to develop analogous experiments for methodological developments [Snieder et al., 2002; Fukushima et al., 2003; van Wijk et al., 2004; Larose et al., 2005b]. Our article presents one analogous ultrasonic experiment not only devoted to the study of the physics of wave propagation in heterogeneous media, but also to the development of new techniques applicable to seismic waves in geosciences.

5.4.2 Scattering properties of the medium

We perform the experiment on a 80 mm×64 mm block of Agar-Agar gel which consists of 95% water and 5% Agar (by weight). 8.5% of the volume of the gel consists of small air bubbles, with diameters between 100 μm and 1 mm. These bubbles render the medium multiply scattering. The source emits a pulse at 2.5 MHz (100% frequency bandwidth). For simplicity, we neglect the electronic noise in the experiment. Since shear waves are strongly attenuated, we assume that only P-waves are propagating in the medium and are eventually recorded. To estimate the scattering properties of the medium, we performed several experiments in the transmission configuration for several medium thickness. From the attenuation of coherent plane wave, we obtain an estimation of the elastic scattering mean free path averaged in the working frequency band : $\ell_e \approx 3.5mm$. Since the scatterers' size is smaller or of the order of the wavelength, scattering is isotropic and we expect a transport mean free path $\ell^\star$ of the same order. In figure 5.1 we plot an example of a diffuse record transmitted through 64 mm of our heterogeneous medium. A theoretical fit is obtained from the two-dimensional (2D) diffusion equation (including reflections from the sides) and plotted as a broken black line. The diffusion constant is $D = v_P\ell^\star/2$ and we assume $\ell_e \approx \ell^\star$. The absorption length ℓ_a is the fit parameter, the best fit is obtained for $\ell_a = 200$ mm. This corresponds to an absorption three times stronger than in pure water [Zagzebski, 1996] which is due to dissipation by the agar material.

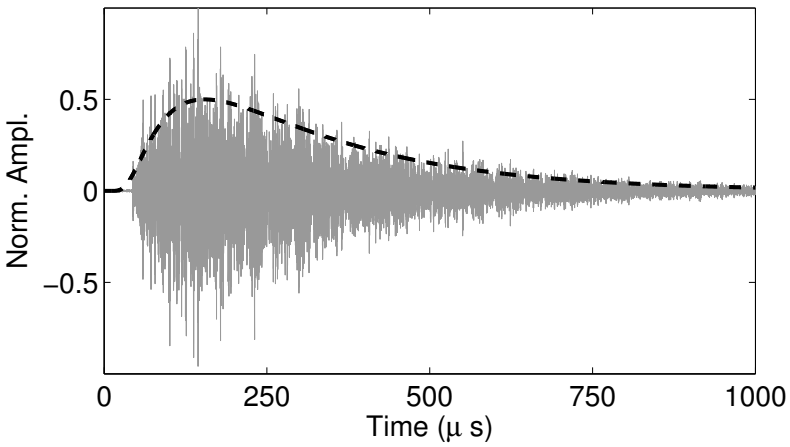

FIG. 5.1 – Gray line : acoustic field transmitted through the 64 mm thick bubble-gel mixture (in normalized amplitude). Black broken line : 2D diffusion equation for $\ell^\star = 3.5$ mm and $\ell_a = 200$ mm.

5.5 Comparison of data processing techniques

Two processing techniques have been proposed in the literature to estimate relative velocity changes dV/V in the diffuse coda. The first one, called the seismic *doublet* technique, was developed for geophysical purposes about twenty years ago [Poupinet et al., 1984]. The idea is to measure a time-shift between two different records in limited time-windows centered at t in the coda. By repeating this procedure at different times t, it is possible to plot the delay δt versus t. The velocity variation is simply the average slope of $\delta t(t)$: $dV/V = -\delta t/t$. Doing so, we implicitly assume that the time-shift is constant within the considered time-window, which might be not the case. This processing found remarkable applications in geophysics, including recent developments in volcano eruption prediction [Brenguier et al., 2008b] and active fault monitoring [Brenguier et al., 2008a].

Another idea [Lobkis and Weaver, 2003; Sens-Schönfelder and Wegler, 2006] is to interpolate the coda at times $t(1-\varepsilon)$ with various relative velocity changes ε. This corresponds to stretching the time axis. The actual velocity change is obtained when the interpolated coda best fits the original data. Because we do not assume a constant time-shift in the considered time window [0 T], we can process the whole data at once, which is expected to result in a more stable, and thus more precise, estimation of dV/V. One drawback is that this latter processing assumes a linear behavior $\delta t(t)$ versus t, or a constant relative velocity change $dV/V = \varepsilon$, which is sometimes not the case in complex heterogeneous media. No quantitative comparison between these two techniques have been established in the literature. In the following section, we propose to test both techniques on the same data set, and analyze their sensitivity to the SNR of the records.

5.5.1 Active experiment : high quality data.

In this experiment, we attach a set of transducers on one side of the gel which act as both sources and receivers of the signal (figure 5.2-left). The source emits a 2.5 MHz pulse. The signal is collected on the same transducer (R) in the pulse-echo configuration. This procedure is repeated on 7 different channels. As the gel contains a large amount of scatterers, the emitted waveform is multiply scattered before reaching the transducer again. A typical ultrasonic record is plotted in figure 5.1. Note that the early $5\mu s$ are muted for technical reasons. This record is composed of the GF of the air-gel mix sample $G(R,R,t)$ and the source wavelet $e(t)$:

$$h_0(t) = G_0(R,R,t) \otimes e(t) \tag{5.1}$$

where $\otimes$ stands for convolution. This experiment is repeated 4 times while the temperature of the medium slowly increases by about 0.8°C, as measured by a digital

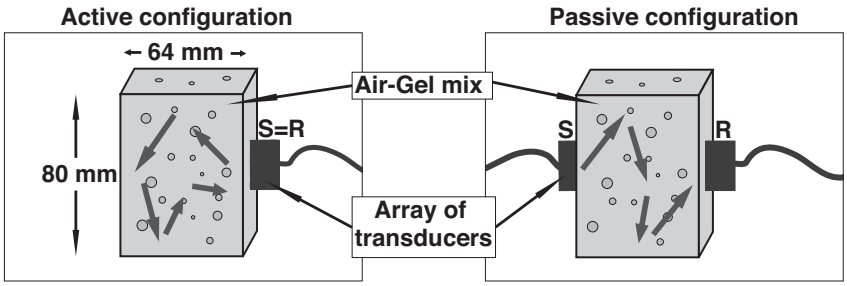

FIG. 5.2 – Experimental setup. Left : the active experiment in the pulse-echo configuration. Right : the passive experiment in the transmission configuration before auto-correlation.

thermometer placed beneath the gel. We assume that the first effect of a temperature change is to stretch the record in time by $\varepsilon_k = dV/V$, and to additionally slightly distort it [Lobkis and Weaver, 2003]. This weak distortion, noted $f(t)$, is not studied here, although it contains precious information about the medium and its evolution. An example of two records is displayed in figure 5.3. After a (small) temperature change, the record rewrites :

$$h_k(t) = G_k(R,R,t) \otimes e(t) \tag{5.2}$$
$$= [G_0(R,R,t(1+\varepsilon_k)) + f(t)] \otimes e(t) \tag{5.3}$$

For each temperature k, the record $h_k(R,R,t)$ is compared to the reference waveform $h_0(R,R,t)$ to evaluate the relative velocity change in the gel sample. Two processing techniques have been proposed in the literature to estimate dV/V : the *doublet* technique and the *stretching* technique.

5.5.1.1 Doublet technique

The doublet technique also known as cross-spectral moving-window technique (CSMWT, Frechet et al. [1989]), computes the phase shift between records for consecutive, overlapping time windows. For a given window, the time shift is assumed to be constant and is estimated in the frequency domain by measuring the Fourier cross-spectrum phase. This estimator uses an accurate, unbiased Wiener filter technique [Jenkins and Watts, 1969] and produces an estimate whose confidence interval is controlled by the coherence values in the frequency band used for the analysis. The method can then measure arbitrary time-shifts between two records with enough similarity (or coherence). The key parameter in this analysis is the Fourier transform window length. The length choice is a trade-off between shift estimate accuracy, and the

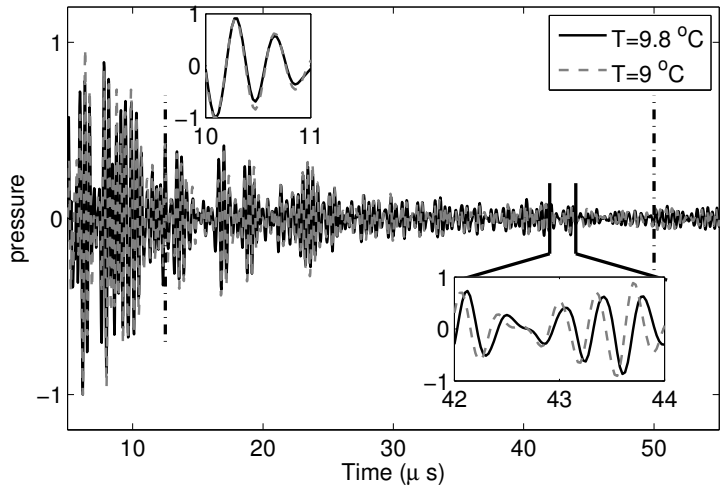

FIG. 5.3 – Example of two records $h_0(t)$ and $h_3(t)$ acquired at the same position (same transducer) but at two different dates. Between the two acquisitions, the temperature has increased by 0.8°C, which is hardly visible in the early part of the record (inset between 10 and 11 μs) but very clear in the late coda (inset between 42 and 44 μs).

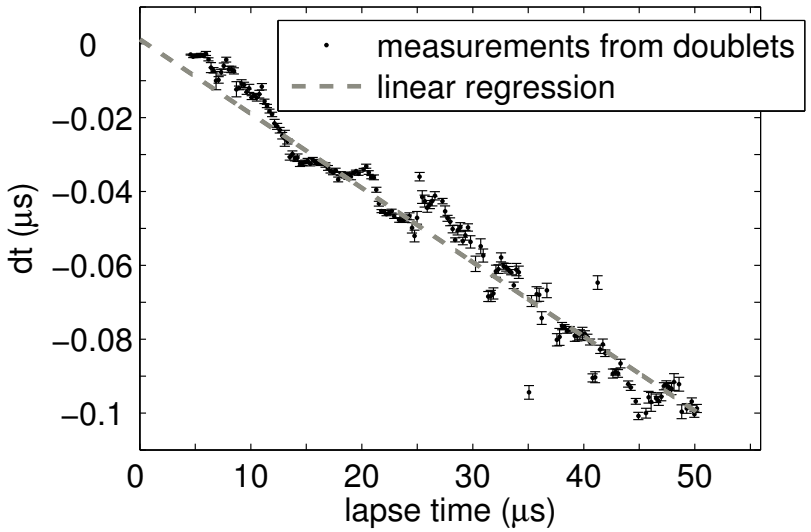

FIG. 5.4 – Delay time evaluated for different lapse times in the coda from the *doublet* code. The broken line is the linear trend whose slope yields dV/V between $k = 0$ and $k = 3$.

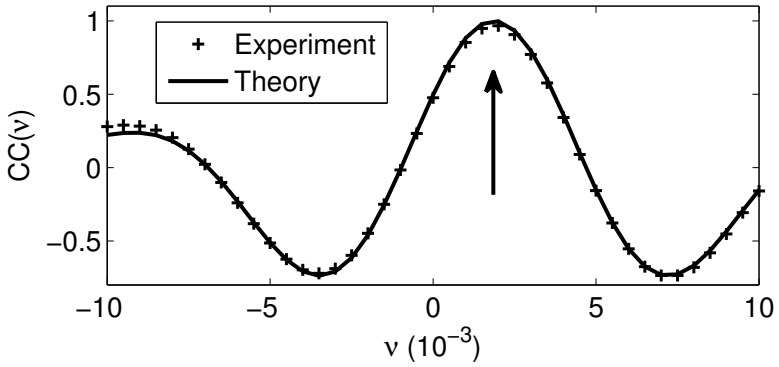

FIG. 5.5 – The correlation coefficient $CC(\varepsilon)$ is evaluated at two temperatures for $k = 0$ & $k = 3$ in the $[12.5\ \mu s - 50\ \mu s]$ range. The maximum, obtained for a relative velocity change of $\varepsilon_3 = 1.86\ 10^{-3}$, is indicated by the vertical arrow. It corresponds to an increase of temperature of 0.8°C. Theory is from Eq. 5.5.

time resolution of possible temporal variations.

We use this *doublet* technique to compute the time shift between the records. The time shift between the two different records is measured in the coda between 12.5 and 50 μs. If the velocity changes homogeneously in the medium, the propagation time will vary proportionally to the propagation distance, producing a phase shift between records varying linearly with lapse time. The relative velocity change can be retrieved by measuring the slope of the phase shift as a function of lapse time, as shown in figure 5.4.

5.5.1.2 Stretching interpolation technique

In the *stretching* technique, the coda $h_k(R, R, t)$ is interpolated at times $t(1 - \varepsilon)$ with various relative velocity changes, ε, in the $[t_1 - t_2]$ time window. ε_k is therefore the ε that maximizes the cross-correlation coefficient :

$$CC_k(\varepsilon) = \frac{\int_{t_1}^{t_2} h_k\left[t(1-\varepsilon)\right] h_0[t]dt}{\sqrt{\int_{t_1}^{t_2} h_k^2\left[t(1-\varepsilon)\right] dt \cdot \int_{t_1}^{t_2} h_0^2[t]dt}} \tag{5.4}$$

An example of correlation coefficient is plotted in figure 5.5. If we assume that h_0 and h_k are stationary waveforms [1] and are well described by Eqs. 5.1 & 5.2, we have a theoretical estimation of CC :

[1] The stationary assumption is done for the sake of simplicity of the calculation. Nevertheless, the main conclusions of the article also apply to non-stationary waveforms as decaying coda.

$$CC_k(\varepsilon) = \frac{A}{\int_{\Delta\omega} \rho(\omega) d\omega} \int_{\Delta\omega} \frac{\rho(\omega) \sin(\omega\ \varepsilon t_2) - \sin(\omega\ \varepsilon t_1)}{\omega\varepsilon\,(t_2 - t_1)}\, d\omega + B(\varepsilon) \tag{5.5}$$

which in the simple case of $t_1 = 0$ and $t_2 = T$ simply reduces to :

$$CC_k(\varepsilon) = A\ \frac{\int_{\Delta\omega} \rho(\omega)\ \text{sinc}\quad (\omega\,(\varepsilon - \varepsilon_k)\,T)\, d\omega}{\int_{\Delta\omega} \rho(\omega) d\omega} + B(\varepsilon) \tag{5.6}$$

with ω the pulsation, $\Delta\omega$ the bandwidth, $\rho(\omega)$ the power spectrum density. The constant A depends on the variance of G, noted $\langle G^2 \rangle$ and the variance of the additional fluctuations, noted $\langle f^2 \rangle$[2],

$$A = \frac{\sqrt{\langle G^2 \rangle}}{\sqrt{\langle G^2 \rangle + \langle f^2 \rangle}} \tag{5.7}$$

$B(\varepsilon)$ is a random process of zero mean and standard deviation :

$$\sqrt{\langle B^2 \rangle} = \sqrt{\frac{2\pi}{T\Delta\omega}}\, \frac{\sqrt{\langle f^2 \rangle}}{\sqrt{\langle G^2 \rangle + \langle f^2 \rangle}} \tag{5.8}$$

The term containing the sinc function is represented by the crosses in figure 5.5 & 5.6, and the fluctuations ($\sqrt{\langle B^2 \rangle}$) around this average are in gray. If the amplitude of the sinc function is much greater than the fluctuations, $A \gg \sqrt{\langle B^2 \rangle}$, the maximum of the cross-correlation coefficient CC_k is obtained for $\varepsilon = \varepsilon_k$, which provides the relative velocity change for the given state k. It is interesting to note that the peak of the sinc function is visible even if the distortion $f(t)$ (or electronic noise $n(t)$, see next subsection) are strong. In such a case, increasing the integration time T or the frequency bandwidth $\Delta\omega$ can reduce the fluctuations B. This is a crucial advantage of the present technique compared to the *doublet* technique in the case of noisy or distorted data.

5.5.2 Active experiment : low quality data

To mimic a practical situation where data includes additional noise (instrumental or electronic), we add a random δ-correlated noise $n(t)$ of zero mean to the signals $h(t)$ in Eq. 5.1 & 5.2. For simplicity, we neglect the distortion f_k in the considered time-window, and assume a stationary noise :

$$\langle n_0^2 \rangle = \langle n_k^2 \rangle = \langle n^2 \rangle \tag{5.9}$$

[2]For derivation, see section 5.9.1

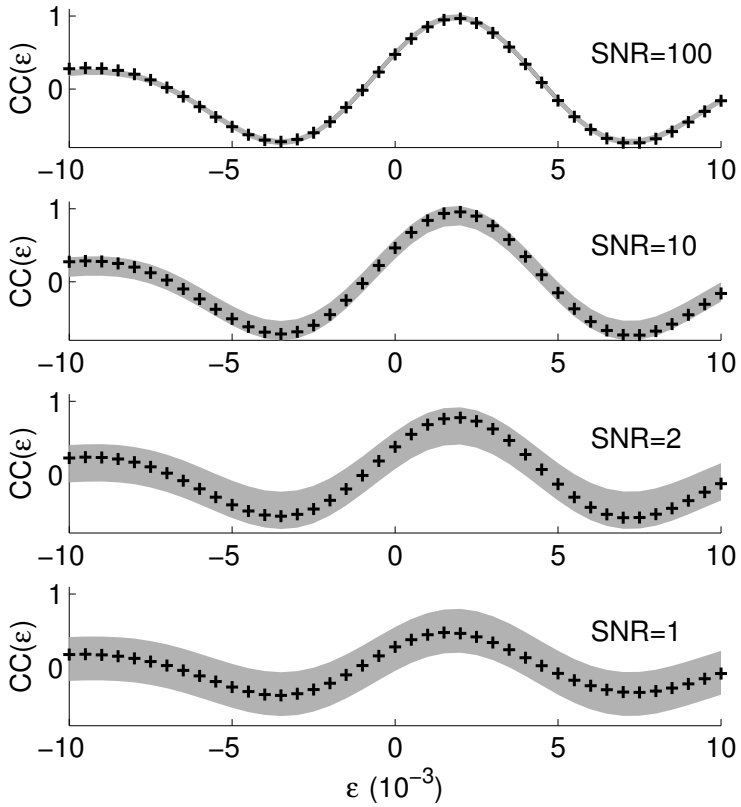

FIG. 5.6 – The correlation coefficient $CC(\varepsilon)$ is evaluated at two temperatures $k = 0$ & $k = 3$ in the $[12.5\ \mu s - 50\ \mu s]$ range, for various signal-to-noise ratio SNR. Crosses indicate experimental data. The gray background indicates expected fluctuations (Eq. 5.11) around the theory (Eq. 5.10). The proper velocity change ε_3 is found in all cases, though a slight difference is visible for SNR=1.

then we get a similar expression as Eq. 5.7 & 5.8, with[3] :

$$A = \frac{\langle h^2 \rangle}{\langle h^2 \rangle + \langle n^2 \rangle} \tag{5.10}$$

and

$$\sqrt{\langle B^2 \rangle} = \sqrt{\frac{2\pi}{T\Delta\omega}} \frac{\sqrt{\langle n^2 \rangle + 2\langle n^2 \rangle \langle h^2 \rangle}}{\langle h^2 \rangle + \langle n^2 \rangle} \tag{5.11}$$

The velocity change is measured again for signal-to-noise (SNR) ranging from 1 to 100 (figures 5.7). For a SNR of 100 and 10, we find the same results for the *stretching* and for the *doublet* technique. However, if the SNR is decreased to 2, the velocity variations measured from the *doublet* technique are not accurate at all, while they remain relevant with the stretching technique. This establishes the *stretching* technique as a more stable processing procedure for noisy records. Note that the connection between the fluctuation of the waveforms and the error in the estimation of $dV/V = \varepsilon$ is shown in Appendix ANevertheless, this error can be visually estimated by the gray area around the theoretical curve (crosses) in figure 5.6.

5.5.3 Advantages and drawbacks of both techniques

The *doublet* technique (CSMWT) has been used successfully for more than 20 years to efficiently retrieve small velocity changes in the medium [Poupinet et al., 1984; Snieder et al., 2002; Brenguier et al., 2008b]. This technique does not suffer from change in amplitude of the waveform, including the coda decay, and the processing is very fast. It also manages clock errors in origin time without further processing, which is a central issue in active and passive field experiments [Stehly et al., 2007]. It also allows to select a given time window in the data.

The *stretching* technique is more recent. It is based on a grid-search for ε, and is found to be slightly more time consuming in terms of computer processing. A noticeable disadvantage of this latter technique is also that it assumes a linear stretching of the waveform, which is not valid for media with heterogeneous changes (including the Earth). The main interest of the *stretching* technique versus the *doublet* one is its stability toward fluctuations (noise) in the data, as mentioned in the previous section and demonstrated by fig. 5.7. This provides an opportunity to increase the sensitivity of detection of weak changes in the earth's crust with seismic waves [Brenguier et al., 2008b,a].

[3] For the derivation, see section 5.9.2

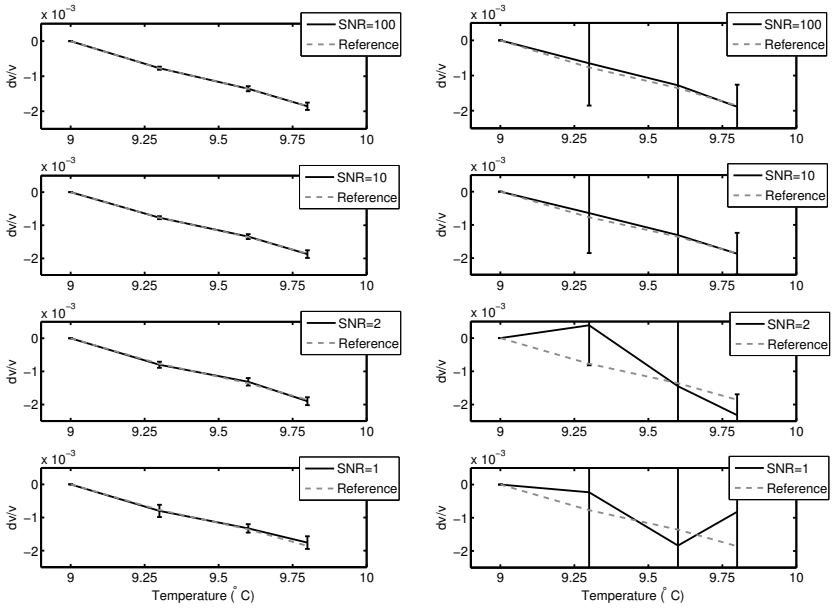

Stretching technique *Doublet* technique

FIG. 5.7 – Relative velocity changes evaluated from the *stretching* (left) and for the *doublet* (right) technique for various SNR. The actual dV/V is satisfiyingly retrieved for any SNR$\geq$ 1 with the first technique, not with the second.

5.6 Active and passive experiment : Monitoring with the correlation ?

Most previous authors suggested that monitoring weak changes in the earth with ambient seismic noise correlation is based on the assumption that those correlations yield the actual GF of the medium. Thus, the late part of the correlation is interpreted as the coda of the reconstructed impulse response. Is this assumption actually necessary to monitor the changing earth with good accuracy ? We address the question in the present section by comparing relative velocity changes measured either in the autocorrelations of records from distant noise sources (the passive experimental setup), or in pulse-echo data (the active experimental setup).

In the passive experiment, transducers are attached at opposite sides of the gel (figure 5.2-right). On one side, 16 sources (S) are acting to mimic a distribution of noise sources. Impulse responses are recorded by the 7 receiving transducers (R) and consecutively convolved by a white noise to mimic acoustic (or seismic) ambient noise. Then they are autocorrelated at each receiver. Note that the precise knowledge of the noise source position is unnecessary : the source position has no effect on the velocity change estimation. If the noise sources were uniformly distributed and the coda records long enough, these correlations averaged over sources should result in the GF for the medium [Weaver and Lobkis, 2001]. However, the records used in this experiment are of finite duration, and the auto-correlation has not converged to the Green function yet. This can be seen visually in figure 5.8, where the autocorrelation is plotted alongside the (time derivative of the) reference Green function obtained in the active experiment. The fact that the two signals are uncorrelated is confirmed by the low value of the coherence between them (2%).

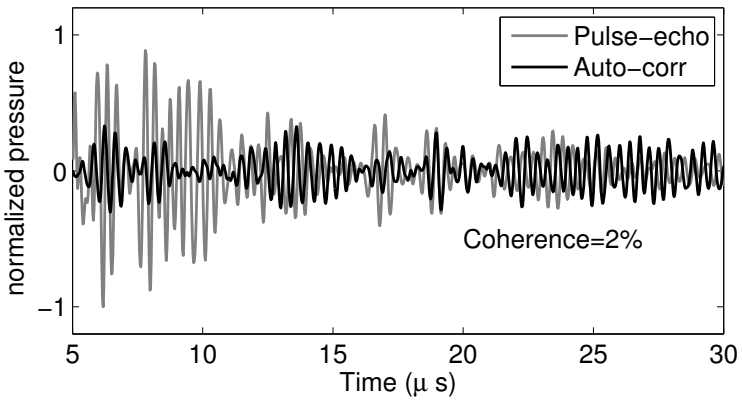

FIG. 5.8 – Comparison of the pulse-echo data $h(R,R,t)$ obtained in the active experiment and the average autocorrelation $\partial_t h(S,R,t) \times h(S,R,t)$.

The noise signals from each source are emitted at consecutive times. To emulate a signal coming from multiple sources at once, the signals recorded from each source i are stacked :

$$h_k(t) = \sum_i G_k(S_i, R, t) \otimes n_i(t), \tag{5.12}$$

where the subscript k holds for temperature. The velocity variations are then computed using the autocorrelation of this total signal.

$$C_k(t) = h_k(t) \times h_k(t). \tag{5.13}$$

The velocity variations for each execution k of these experiments are displayed in figure 5.9, alongside those found with the active experiment. The acquisitions run over about 25 minutes, over which the temperature has increased by about 0.8°C. Within the errors, the velocity variations found with the autocorrelation are the same as those found with the reference GF.

Until now, the analysis was based on the assumption that the autocorrelation used in the passive experiment closely resembles the GF of the medium if there are enough sources, and these sources are stable. In our experiment, the GF is not reconstructed in the auto-correlation. Nevertheless, figure 5.9 demonstrates[4] that it is still possible to retrieve correct information about small changes in the medium

[4]Note that the systematic deviation of the passive experiment from the active one is in part due to a small spatial variability of the temperature change. The auto-correlation (S≠R) is sensitive to the whole medium whereas the pulse-echo wavefield (S=R) is more sensitive to the vicinity of the receiver.

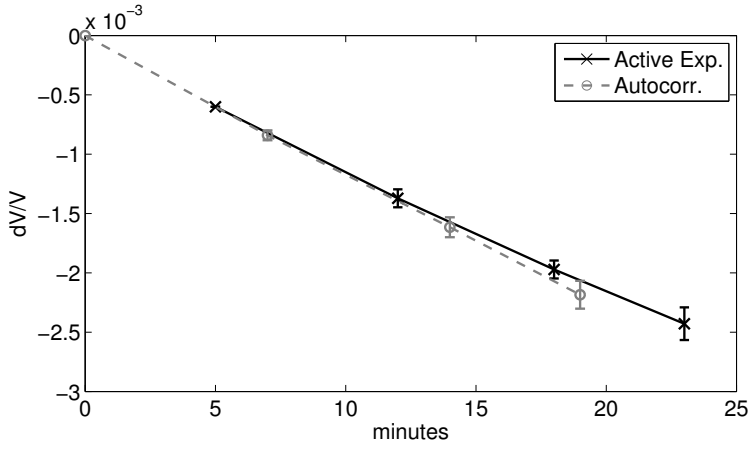

FIG. 5.9 – Relative velocity changes evaluated from the active (pulse-echo with S=R) and the passive (autocorrelation with S≠R) setup.

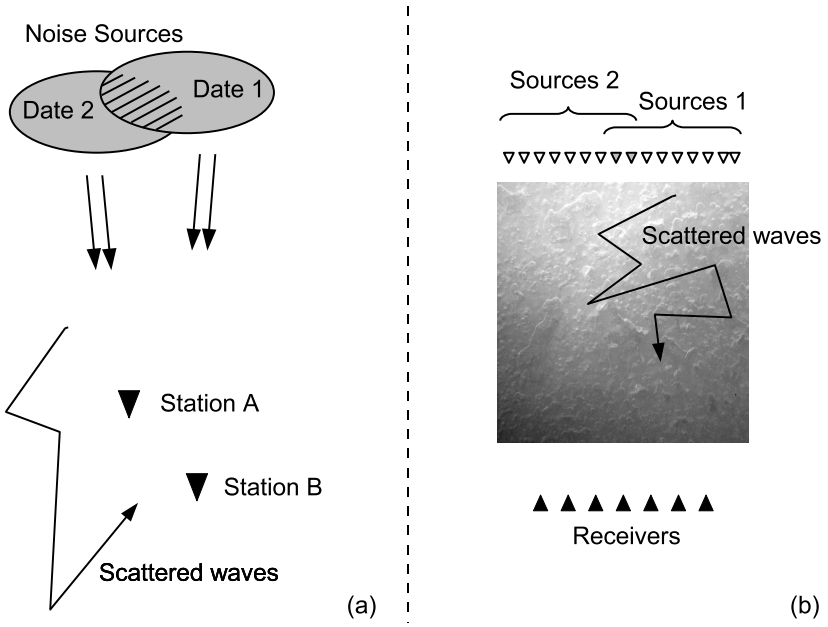

FIG. 5.10 – (a) The seismic noise source structure changes from one date to another. (b) Analogous laboratory experiment : two sets of sources are chosen at two different dates.

properties with the resulting auto-correlation. This is a very promising observation that supports the idea that correlation of seismic noise will give the opportunity to monitor weak changes in the Earth with good reliability even when the correlations have not converged to the GF. Indeed, in both *active* and *passive* experiments, we measure the acoustic/seismic signatures of the medium, which naturally include its weak variations.

Nevertheless, in order to achieve a proper comparison between our laboratory-scale experiment and seismology, we have to take into account another phenomenon. Indeed, on the earth, the seismic noise sources location is smoothly changing from one week to another. The question addressed in the next section is then : what will happen to our monitoring technique when the background noise is no longer stable, *i.e.*, the source distribution changes spatially ?

5.7 Influence of noise source stability

The change in background noise structure is simulated by averaging the autocorrelations for a number of simultaneous uncorrelated sources i. The same is done for a slightly different selection of sources a few instants later, then we calculate the

relative velocity change dV/V between the two autocorrelations. A simple picture of this is given in figure 5.10. Imagine for instance that at date k =0, sources 1 and 2 are active, and at date k =1 sources 2 and 3. For three sources, the decorrelation of the signals can be analyzed theoretically. For the first experiment (k =0), the record is :

$$h_0 = G(S_1, R, t) \otimes n_1(t) + G(S_2, R, t) \otimes n_2(t) \tag{5.14}$$

and its auto-correlation reads :

$$C_0 = h_0 \times h_0 \tag{5.15}$$

or :

$$\begin{aligned} C_0 \quad = \quad & G(S_1, R, t) \times G(S_1, R, t) \otimes n_1(t) \times n_1(-t) && (5.16)\\ & + G(S_2, R, t) \times G(S_2, R, t) \otimes n_2(t) \times n_2(-t) && (5.17)\\ & + 2G(S_1, R, t) \times G(S_2, R, t) \otimes n_1(t) \times n_2(-t) && (5.18) \end{aligned}$$

Since $n_1(t) \times n_2(t)$ is almost zero, we neglect the third term. For simplicity, we shorten the notation :

$$G(S_i, R, t) \times G(S_i, R, t) \otimes n_i(t) \times n_i(-t) = AC_i(t) \tag{5.19}$$

Which leads to :

$$C_0(t) = AC_1(t) + AC_2(t) \tag{5.20}$$

Similarly, for the second experiment (k =1), in which the signal is stretched due to the velocity change and the sources used are numbered 2 and 3, we get :

$$C_k = AC_2(t[1-\varepsilon]) + AC_3(t[1-\varepsilon]). \tag{5.21}$$

The objective is to find the ε_k that maximizes the cross correlation coefficient CC_k defined in Eq. 5.4. The terms AC_1 and AC_3 are decorrelated waveforms that play the role of fluctuations (eq. 5.2) and will contribute to the term B in eq. 5.5. Assuming that the variance of AC_k is constant : $\langle AC_1^2 \rangle = \langle AC_2^2 \rangle = \langle AC_3^2 \rangle$, we find $A = \frac{1}{2}$ and the standard deviation of B simplifies as $\sqrt{\langle B^2 \rangle} = \sqrt{3}\sqrt{2\pi}/2\sqrt{T\Delta\omega}$. From this latter equation, we deduce that a proper estimation of dV/V is carried out if we process a sufficiently large amount of data : $\sqrt{T\Delta\omega} \gg \sqrt{3}\sqrt{2\pi}$. This figure is valid

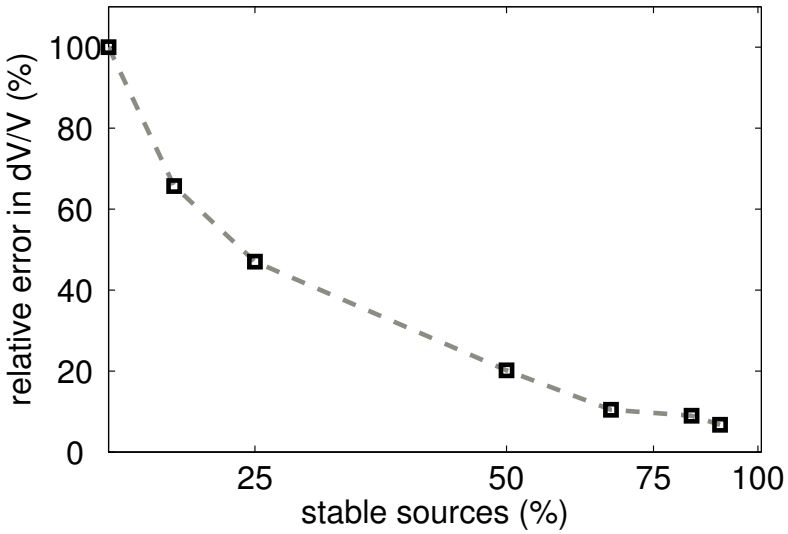

FIG. 5.11 – Relative error in the estimation of $\varepsilon = dV/V$, versus the ratio of unchanged-to-total amount of noise sources (x-axis in log. scale).

for two sets of sources that have 50% of sources in common. The same calculation can be carried out for any ratio of unchanged-to-total amount of uncorrelated sources.

As an example, in figure 5.11 we report the relative experimental error in the estimation of dV/V for various unchanged-to-total source amount ratio. The velocity evolution retrieved through the autocorrelation, as shown in figure 5.9, is used as a reference. For different ratios of spatially unchanged sources, the velocity changes are computed again, and the deviation with respect to the reference is considered the error. In figure 5.11 the relative error estimation is shown for different ratios of unchanged-to-total sources. When half the sources remain stationary, the relative error is ~ 20 %, meaning that we have access to a rough (but relevant and interpretable) estimate of the velocity change. With the given experimental coda duration and bandwidth, we observe that a satisfying estimation of dV/V is obtained if 50% of the sources are unchanged.

In this framework, we conclude more generally that the spatial instability of the source distribution is not a limitation for noise-based correlation monitoring as long as at least part of the noise spatial distribution is stable. The smaller the stable area, the harder the dV/V estimation, and similar to the conclusion of section III, a larger the integration time T or bandwidth $\Delta\omega$ is required.

5.8 Discussion and Perspectives

In this paper we conducted laboratory experiments with ultrasonic waves to monitor weak velocity changes in the medium. To that end, we employed and compared several procedures that process small phase shift in the diffuse coda waves. These phase shifts correspond to change of arrival time in the waveforms, which were due to small temperature changes in the medium.

The paper began with an active (pulse-echo) experiment (section 5.5), in which we compared the *doublet* (or CSMWT) technique to the more recent *stretching* technique. The former is based on Fourier analysis in multiple time windows. The latter is based on the interpolation of the whole waveform and on a grid search optimization. The latter was found to require more computing power, but was also found to be more stable toward noise in the data. In the second part of the paper (section 5.6), we processed the auto-correlation of noise records acquired in the same medium. Active (pulse-echo) and passive (auto-correlations) data were processed using exactly the same processing procedure : the relative velocity changes of the medium were deduced from the late arrivals using the *stretching* technique. Very similar results were found in both cases, although auto-correlations had not at all converged to the GF. We therefore demonstrated that, contrary to prior belief, passive monitoring with ambient noise remains possible even when the correlation has not converged to the GF. In other words, noise-based monitoring requires weaker assumptions than noise-based imaging. In the last part of the present document (section 5.7), we tested the robustness of the noise-based monitoring technique in the case of unstable distributions of noise sources. We demonstrated that, as long as a certain portion of the sources is stable, velocity variations can still be retrieved.

Even though we consider a laboratory experiment in this paper, in practice the results can be extended to different scales, among which seismology is of particular interest. Note that the idea that the coda of the correlations contains precious informations has been recently demonstrated by studying the Correlation of the Coda of the Correlation (C^3) [Stehly et al., 2008]. In previous monitoring studies along the San-Andreas faultline at Parkfield, California [Brenguier et al., 2008a], there were some doubts as to whether or not the GF was properly reconstructed in the correlations. This was due to i) the imperfect source distribution in the ocean, ii) to the short time-series over which correlations were performed and iii) the low quality data for frequencies below 1 Hz. Nevertheless, it was still possible to observe small variations in the coda of the correlations. From our laboratory experiment, we can confirm that these latter changes are actual physical observations that can be interpreted by velocity changes in the crust. On a somewhat smaller scale, passive monitoring can be applied to seismic prospecting on reservoirs. On such reservoirs, the technique could for instance be used to follow the effect of fluid flows as oil or

gas. During production, we indeed expect relative changes of velocity in the reservoir of the order of a few percent [Ellison et al., 2004], which seems to be observable by the method presented here. It might also be possible to detect the velocity variations caused by stress changes following subsidence. This monitoring could either be performed with reproducible active sources or with background seismic noise.

5.9 Calculations

In this section, I derive expressions for the value of A and B in equations (5.7) and (5.8), respectively. Then, in subsection 5.9.2, the same is repeated in the case of signals with added noise. This leads to expressions for A (5.10) and B (5.11).

5.9.1 High Quality Data

In the stretching technique we are looking to maximize the cross correlation coefficient (equation (5.4)) :

$$CC_k(\varepsilon) = \frac{\int_{t_1}^{t_2} h_k\left[t(1-\varepsilon)\right] h_0[t]dt}{\sqrt{\int_{t_1}^{t_2} h_k^2\left[t(1-\varepsilon)\right] dt \int_{t_1}^{t_2} h_0^2[t]dt}} \tag{5.22}$$

In section 5.5.1 we estimate CC_k for high quality data, without electronic or other noise. Our signals before and after a small temperature change then become :

$$h_0(t) = G_0(R,R,t) \otimes e(t) \tag{5.23}$$

and

$$h_k(t) = G_k(R,R,t) \otimes e(t) = \left[G_0\left(R,R,t(1+\varepsilon_k)\right) + f(t)\right] \otimes e(t) \tag{5.24}$$

where ε_k is the amount by which the record is stretched, and $f(t)$ represents the small fluctuations due to tiny physical changes in the medium as it expands slightly. Both h_0 and h_k are assumed to be stationary. Applying (5.23) and (5.24) to (5.22), we get :

$$CC_k(\varepsilon) = \frac{\int_{t_1}^{t_2} \left[G_0\left(R, R, t(1+\varepsilon_k) + f(t)\right] \otimes e(t)\left[G_0(R, R, t)\right] \otimes e(t) dt}{\sqrt{\int_{t_1}^{t_2} \{\left[G_0\left(R, R, t(1+\varepsilon_k) + f(t)\right] \otimes e(t)\}^2 dt \int_{t_1}^{t_2} \{\left[G_0(R, R, t)\right] \otimes e(t)\}^2 dt}} \tag{5.25}$$

We consider the simple case where $t_1 = 0$ and $t_2 = T$. We know that :

$$\rho(t) = \frac{e(t) \otimes e(t)}{\int e^2(t)} \tag{5.26}$$

and simplify the expression to :

$$CC_k = \frac{\int_0^T \left[G_0^2 + G_0 f\right] \otimes \rho(t)\, dt}{\sqrt{\int_0^T \left[G_0^2\right] \otimes \rho(t)\, dt \int_0^T \left[G_0^2 + f^2 + 2G_0 f\right] \otimes \rho(t)\, dt}} \tag{5.27}$$

Before calculating the mean value of CC_k, we assume that the Green functions at different times $G_0(t)$ and $G_0(t')$ are random, δ-correlated signals, with zero mean. This means that $\langle G(t)G(t')\rangle \approx \delta(t-t')$ and $\langle G_0\rangle = 0$. Furthermore, we suppose that the mean intensity of the Green function will remain unchanged before and after a temperature change : $\langle G_0^2\rangle = \langle G_k^2\rangle = \langle G^2\rangle$. The mean of any crossterms with the fluctuations $\langle G_0 f\rangle$ are set to zero. We use that $\langle \int_0^T G_0^2 dt\rangle = T\langle G_0^2\rangle$. With all this we can estimate the mean of CC_k :

$$A = \langle CC_k\rangle = \frac{T\langle G_0^2\rangle}{T\sqrt{\langle G_0^2\rangle(\langle G_0^2\rangle + \langle f^2\rangle)}} = \frac{\sqrt{\langle G_0^2\rangle}}{\sqrt{\langle G_0^2\rangle + \langle f^2\rangle}} \tag{5.28}$$

which is the constant A in equation (5.7).

In order to find the amplitude of the fluctuations around the mean value we need to calculate the standard deviation of CC_k. We can first estimate its variance : $\mathrm{var}(CC_k) = \langle CC_k^2\rangle - \langle CC_k\rangle^2$. Breaking it up into smaller pieces, we start by calculating the mean of CC_k^2 :

$$CC_k^2 = \frac{\int_0^T \left[G_0^2 + G_0 f\right] \otimes \rho(t)\, dt \int_0^T \left[G_0^2 + G_0 f\right] \otimes \rho(t')\, dt'}{\int_0^T \left[G_0^2\right] \otimes \rho(t)\, dt \int_0^T \left[G_0^2 + f^2 + 2G_0 f\right] \otimes \rho(t)\, dt}$$

$$= \frac{\int_0^T \int_0^T \left[G_0^2 + G_0 f\right]\left[G_0^2 + G_0 f\right] \otimes \rho(t) \otimes \rho(t')\, dt dt'}{\int_0^T G_0^2 \otimes \rho(t)\, dt \int_0^T \left[G_0^2 + f^2 + 2G_0 f\right] \otimes \rho(t)\, dt} \tag{5.29}$$

Again, crossterms with $\langle G_0 f \rangle$ are zero. The same assumptions as before equation (5.28) hold, and we use that :

$$\int \rho(t)^2 dt \approx \frac{\Delta\omega}{2\pi} \tag{5.30}$$

The mean value of CC_k^2 then becomes :

$$\langle CC_k^2 \rangle = \frac{2\pi}{\Delta\omega} \frac{T(\langle G_0^2 \rangle^2 + \langle G_0^2 \rangle \langle f^2 \rangle)}{T^2 \langle G_0^2 \rangle (\langle G_0^2 \rangle + \langle f^2 \rangle)}. \tag{5.31}$$

Now the standard deviation is $\sqrt{\mathrm{var}(CC_k)}$, or, using $\langle CC_k \rangle^2$ from equation (5.28), $\sqrt{\langle B^2 \rangle} = \sqrt{\langle CC_k^2 \rangle - \langle CC_k \rangle^2}$:

$$\sqrt{\langle B^2 \rangle} = \sqrt{\frac{2\pi}{\Delta\omega\, T}} \frac{\sqrt{\langle f^2 \rangle}}{\sqrt{\langle G_0^2 \rangle + \langle f^2 \rangle}}, \tag{5.32}$$

which is equation (5.8).

5.9.2 Low Quality Data

In section 5.5.2 we consider a signal with some noise added, electronic or otherwise :

$$S_0 = h_0 + n_0 \tag{5.33}$$

$$S_k = h_k + n_k \tag{5.34}$$

The mean value of CC_k will be a bit different for this case :

$$CC_k(\varepsilon) = \frac{\int_0^T [h_0 + n_0]\,[h_k + n_k] \otimes e(t) \otimes e(t)\, dt}{\sqrt{\int_0^T [(h_0 + n_0) \otimes e(t)]^2\, dt \int_0^T [(h_k + n_k) \otimes e(t)]^2\, dt}}$$

$$= \frac{\int_0^T [h_0 h_k + h_0 n_k + h_k n_0 + n_0 n_k] \otimes \rho(t)\, dt}{\sqrt{\int_0^T \left[h_0^2 + n_0^2 + 2h_0 n_0\right] \otimes \rho(t)\, dt \int_0^T \left[h_k^2 + n_k^2 + 2h_k n_k\right] \otimes \rho(t)\, dt}} \tag{5.35}$$

We assume that the mean of the crossterms involving noise (*e.g.*, $\langle h_i n_i \rangle$ and $\langle n_i n_j \rangle$) are zero. We also assume that the mean of the main signal h will stay the same after a temperature change : $\langle h_0^2 \rangle = \langle h_k^2 \rangle = \langle h^2 \rangle$. With this, the mean of CC_k is :

$$A = \langle CC_k \rangle = \frac{\langle h^2 \rangle}{\langle h^2 \rangle + \langle n^2 \rangle}, \tag{5.36}$$

which is equation (5.10).

As before, the variance of CC_k is given by $\mathrm{var}(CC_k) = \langle CC_k^2 \rangle - \langle CC_k \rangle^2$:

$$CC_k^2 = \frac{\int_0^T \int_0^T \left[(h_0 + n_0)^2 (h_k + n_k)^2\right] \otimes \rho(t) \otimes \rho(t')\, dt' dt}{T^2(\langle h^2 \rangle + \langle n^2 \rangle)^2 \int_0^T \rho(t)^2 dt}$$

$$= \frac{\int_0^T \int_0^T \left[(h_0^2 + n_0^2 + h_0 n_0)(h_k^2 + n_k^2 + h_k n_k)\right] \otimes \rho(t) \otimes \rho(t')\, dt' dt}{T^2(\langle h^2 \rangle + \langle n^2 \rangle)^2 \int_0^T \rho(t)^2 dt} \tag{5.37}$$

Again, crossterms with noise are set to zero. Using equation (5.30), the mean of CC_k^2 is now :

$$\langle CC_k^2 \rangle = \frac{2\pi\, T \left[\langle h^2 \rangle^2 + \langle n^2 \rangle^2 + 2\langle h^2 \rangle \langle n^2 \rangle\right]}{\Delta\omega\, T^2(\langle h^2 \rangle + \langle n^2 \rangle)^2} \tag{5.38}$$

and the variance of CC_k, using equation (5.36) :

$$\mathrm{var}(CC_k) = \langle CC_k^2 \rangle - \langle CC_k \rangle^2 = \frac{2\pi}{\Delta\omega\, T} \frac{\langle n^2 \rangle^2 + 2\langle h^2 \rangle \langle n^2 \rangle}{(\langle h^2 \rangle + \langle n^2 \rangle)^2} \tag{5.39}$$

Now the standard deviation is just the square root of equation (5.39) :

$$\sqrt{\langle B^2 \rangle} = \sqrt{\frac{2\pi}{\Delta\omega\, T}} \frac{\sqrt{\langle n^2 \rangle^2 + 2\langle h^2 \rangle \langle n^2 \rangle}}{\langle h^2 \rangle + \langle n^2 \rangle}, \tag{5.40}$$

which is equation (5.11).

5.10 Questions Raised

The most important result from this paper is that it is possible to measure the relative velocity change on the coda of a cross-correlation signal which has not

completely converged to the Green's function. This result holds as long as the noise sources used stay stable during the measurement, or if the medium is sufficiently scattering.

Applied to seismology, this result means that it may not be necessary to cross-correlate long temporal averages of seismic noise. Armed with this knowledge, I will go back to the Parkfield dataset in chapter 7. By reducing the stack length of the cross-correlations, and applying an adaptive filter to the signals, it is possible to improve the temporal resolution of the dV/V measurements.

Chapitre 6

Precision of velocity change measurements

Contents

6.1 Introduction **63**
6.2 Apparent Dilation **63**
6.2.1 Calculation 65
6.3 Application : Laboratory Experiments **66**
6.4 Application : Parkfield **68**
6.5 Conclusion **70**

6.1 Introduction

In chapter 4, we have established the possibility of measuring dV/V on fault zones. Two velocity drops were measured, as well as smaller fluctuations. To what extent are these relative velocity changes significant ? In the following, we estimate the precision of dV/V measurements when evaluated with the *stretching* method, as detailed in section 3.3. This is an excerpt of the paper, which is included in its entirety in Appendix A.

6.2 Apparent Dilation

A multiply scattered wave can resist detailed interpretation, but for purposes of monitoring it may not be necessary to interpret the waveform : it is sufficient to notice changes. In many such cases the change is due to a uniform change of wave speed. To detect such, Lobkis and Weaver [2003] constructed a dilation correlation coefficient between waveforms ϕ_1 and ϕ_2.

$$X(\varepsilon) = \int \frac{\phi_1(t)\phi_2(t(1+\varepsilon))dt}{\sqrt{\int \phi_1^2(t)dt \int \phi_2^2(t(1+\varepsilon))dt}} \tag{6.1}$$

X takes on a value of unity at $\varepsilon = 0$ if the two waveforms are identical. It will reach unity at some characteristic value of ε if the two waveforms differ only by some temporal dilation. The estimated degree of dilation between two waveforms is taken to be the value of ε at which X is maximum. X reaches a maximum of less than unity if the waveforms differ by more than dilation alone. Therefore, the value of X at its maximum, if it is less than unity, may be interpreted as a measure of the distortion between the waveforms.

In the previous chapters, monitoring is performed by comparing correlations of noise taken at different moments. Very commonly, the noise which is correlated is incompletely equipartitioned, such that the resulting correlation waveforms do not precisely correspond to the Green's function. It also may be that one has not averaged enough raw data ; the correlation may not have yet converged. Theoretical and applied work is ongoing in attempts to understand and correct for systematic errors due to these effects (*e.g.*, Weaver et al. [2009a]; Froment et al. [2010]).

The correlations may have been obtained from different samples of ambient noise, perhaps on different dates, or from the codas of different events. The correlations are of course never identical ; they are often very different. One reason for a difference is that the source of the noise may be different (yet if the correlation has converged to the local Green's function, a change of noise source ought to have little effect). Continuous seismic sources can move and strengthen and weaken as weather changes at sea. It may also be that the correlation has not fully converged (*i.e.*, , insufficient averaging has been done). A third possibility is that the local mechanical or acoustic environment may have evolved, in particular, the local wave speed(s) may have changed. It is this possibility that is of particular interest, as changes in seismic velocities are associated with relaxations after major seismic events (such as in chapter 4). In some cases changes in seismic velocity can be used to predict volcanic eruptions [Brenguier et al., 2008b]. Therefore, it is of great interest to be able to discern whether a change is due to a change in local environment or to a change in the character of the noise.

Our purpose here is to evaluate the precision with which wave speed changes can be evaluated. To do this we consider the case in which the two waveforms $\phi_1(t)$ and $\phi_2(t)$ differ only by noise so that the actual relative dilation, without noise, is zero. We then ask for the apparent (non-zero in general) value of ε at which the corresponding X in equation (6.1) achieves its maximum. We calculate the root mean square value of this apparent, and erroneous, relative dilation.

6.2.1 Calculation

Here we examine the apparent waveform-dilation between two nominally identical signals. Theoretically, which one ought to infer a relative dilation ε of zero, however, noise can corrupt the inference. Key to the following analysis is an understanding that the signals being discussed are like coda, in that they are statistically stationary with durations long compared to an inverse bandwidth. We take the two waveforms to have an identical part $\psi(t)$, and to differ by noise $2\mu\chi(t)$. In the limit $\mu \to 0$, the waveforms become identical and have no relative dilation. However, if $\mu \neq 0$, there will be an apparent, but actually meaningless, temporal dilation between them. We wish to estimate this erroneous apparent relative dilation, and to identify any signatures that could be used to alert to the possibility of error. Note that the common part ψ of the signals need not be the local Green's functions.

Given an expression for the apparent dilation between two waveforms differing only by noise fluctuations, we can obtain statistical estimates for its root-mean-square, given assumptions about the envelopes and spectra of the waveforms. The root-mean-square value of this dilation gives an indication of the typical fluctuations around the expected zero.

The root-mean-square values will be estimated based on a number of assumptions about the two waveforms :
– They are stationary, noise-like and Gaussian
– The spectra are similar, with a central frequency ω_c
– Their duration is long compared to the inverse of ω_c
– They have the same amplitude
The root mean square of the apparent dilation measured between two waveforms, which is *not* the result of a dilation, can be expressed as :

$$\text{rms } \varepsilon = \frac{\sqrt{1-X^2}}{2X}\sqrt{\frac{6\sqrt{\frac{\pi}{2}}T}{\omega_c^2\,(t_2^3 - t_1^3)}} \tag{6.2}$$

Here, T can be identified by noting that the -10dB points are at $\omega_c \pm \ln(10/T)$. t_1 and t_2 are the start and end time of the signal timewindow, respectively.

This expression scales inversely with the duration of the correlation waveform in units of the period, and inversely with the square root of the duration in units of the inverse bandwidth. In practice (6.2) can be very small. The quantity $\omega(t_2 - t_1)$ is of the order of the coda-Q, the duration of the waveform in units of the period. The quantity T is the amount of time for one bit of information to be delivered. Thus (6.2) can be recognized as scaling inversely with Q, and inversely with the square root of the amount of information. It also may be recognized that small X corresponding

to waveforms ϕ_1 and ϕ_2 that are very different, permits the practitioners erroneous estimate of dilation to be large.

Application of equation 6.2 is straightforward. An estimate of the relative dilation ε between two waveforms ϕ_1 and ϕ_2 may be compared to (6.2). Values in excess of (6.2) are consistent with the inference that the observed dilation is real. Changes in waveform source or other character should not generate apparent dilations in excess of (6.2). Furthermore, in absence of any actual dilation, estimates of ε of the order of (6.2) will nevertheless be generated in practice. These should be regarded as un-meaningful.

6.3 Application : Laboratory Experiments

The prediction from equation 6.2 is compared to waveform dilation measurements in the laboratory ultrasonic experiments from chapter 5.

Several piezoelectric sensors and sources were applied to a multiply scattering air-bubble filled gel. Sources and receivers were placed on opposite sides, 64 mm apart. We know that multiple scattering was strong : received waveforms from sources to receivers were coda-like, with envelopes that resembled the solution of a diffusion equation (figure 5.1, section 5.4.2). Each correlation-function g_{sr} is windowed between lapse times of $t_1 = 12.5$ to $t_2 = 50$ μsec. The typical g_{sr} is stationary over this interval and has a power spectrum centered on 2.35 MHz with -10dB points at 1.7 and 3.0 MHz.

Using t_1=12.5 μsec, $t_2 = 50$ μsec, $\omega_c = 15\text{rad}/\mu\text{sec}$; and $T = 0.56$ μsec, we conclude from (6.2),

$$\text{rms } \varepsilon = 3.8 \times 10^{-4} \ \frac{\sqrt{1 - X^2}}{2X} \tag{6.3}$$

It may be that lengthening the considered time interval beyond the chosen 12.5 $\rightarrow$ 50 μsec would increase the precision. However, it could also diminish X : in principle there are trade-offs.

The tables below are formed by maximizing the dilation correlation coefficient X between sums over different sets of sources. All tests were conducted at fixed temperature, the actual relative temporal dilation is therefore zero. The goal of the test is to measure the dilation induced by the difference in waveform due to a different source distribution.

X for seven receivers and three different choices for the set of sources

set 1	0.9312	0.9169	0.8893	0.8458	0.8226	0.8852	0.8683
set 2	0.9394	0.8833	0.9083	0.8464	0.8872	0.8631	0.8928
set 3	0.9458	0.9009	0.8730	0.7942	0.8322	0.8396	0.7979

The dilation ε ($\times 10^{-3}$) as obtained by maximizing X for each of these cases

set 1	0.06	0.04	-0.16	0.08	-0.04	-0.10	0.18
set 2	-0.04	-0.04	-0.08	0.06	-0.14	-0.08	0.10
set 3	-0.16	0.08	-0.12	0.00	-0.14	-0.24	-0.12

Experimental root mean square dilation ε ($\times 10^{-3}$)

all sets	0.1013	0.0566	0.1244	0.0577	0.1166	0.1571	0.1376

Theoretical root mean square (6.3)

all sets	0.07	0.09	0.09	0.12	0.11	0.10	0.11

TAB. 6.1 – Comparison of best-fit waveform dilations ε with the predictions of equation (6.3). A maximum value of X and the ε at which that X is maximum, are constructed for each of seven receivers (the seven columns) and the three choices for the set of sources described in the text (the three rows). The root mean square of those ε is compared with the predictions of theory. That X is of order 0.9 is consistent with one source in ten having changed.

Tables 6.1 and 6.2 show two case studies. In the first case, autocorrelations calculated from the signals at a receiver r, as produced by eleven distinct sources s, were averaged to generate the reference waveform $\phi_1 = \sum_s g_{sr}$. For each of three comparison waveforms ϕ_2, the same sum was done, keeping the first ten sources unchanged. In order to deliberately change the waveform without dilation, the eleventh source is replaced with sources number twelve, thirteen and fourteen respectively. This was repeated for each of seven receivers. In each case we compare three waveforms ϕ_2 with the reference ϕ_1 and evaluate $X(\varepsilon)$. The table shows the maximum value of $X(\varepsilon)$, and the value of ε that did this, for each of the 21 cases. For each of the seven receivers we calculate the rms of these three ε. If the only changes were to the source of the noise field, and not the medium, one would expect no dilation, or $\varepsilon = 0$. Nevertheless, the differences in sources do generate apparent dilations ε. Theory, especially in light of the approximate modeling of the spectrum, may be said to have done a good job predicting the fluctuations.

In the second study, four sources were held constant, and two were varied. Here the reference waveform was constructed from a sum over six sources $\sum_s g_{sr}$; each of the other three waveforms was constructed by replacing sources number five and six in that sum with two others. Again, the theory may be said to have done a good job.

X for seven receivers and three different choices for the set of sources

set 1	0.6181	0.7864	0.7143	0.8400	0.7149	0.8458	0.7863
set 2	0.6359	0.7340	0.7011	0.8451	0.8020	0.8285	0.8194
set 3	0.5948	0.7397	0.5837	0.8165	0.8294	0.8451	0.8745

The dilation ε ($\times 10^{-3}$) as obtained by maximizing X for each of these cases

set 1	-0.0800	0.0400	0.4600	-0.0200	0.1400	0.0400	0.1600
set 2	-0.0200	0.0400	0.0400	-0.3400	-0.0800	-0.1400	0.0800
set 3	-0.4600	0.1600	0.5600	-0.0400	0.0800	-0.0400	0.0400

Experimental root mean square dilation ε ($\times 10^{-3}$)

all sets	0.27	0.098	0.419	0.198	0.104	0.087	0.106

Theoretical root mean square (6.3)

all sets	0.19	0.14	0.17	0.12	0.14	0.12	0.11

TAB. 6.2 – As in table 6.1, but for sources that differ by more, as evident in the smaller values of X

6.4 Application : Parkfield

In chapter 4, the dV/V changes were evaluated with the *doublet* method (section 3.2). Here, we repeat the measurements using the *stretching* method (section 3.3), only to obtain very similar results. Now, we will see if the dV/V values obtained for the two velocity drops are larger than the apparent dilation derived above.

For each of 78 receiver pairs, we compared the 1550-day average correlation waveform with the correlation waveform constructed from each of 1546 overlapping 5-day segments. Each correlation waveform was windowed between -50 and -20 seconds, and again from 20 to 50 seconds (thus excluding direct Rayleigh arrivals and emphasizing the multiply scattered diffuse part of the signal for which the theory was developed). An X and an ε were deduced for each day. Power spectra were centered on 0.5 Hz, with -10dB shoulders at 0.1 and 0.9 Hz. These numbers permit the evaluation of (6.2) :

$$\text{rms } \varepsilon = 3 \times 10^{-3} \, \frac{\sqrt{1 - X^2}}{2X} \tag{6.4}$$

Figure 6.1 shows the mean (over the 78 receiver pairs) values of X and ε between each of the 1546 overlapping 5-day correlation waveforms, ϕ_1, and the correlation waveform ϕ_2 as obtained by averaging over the entire 5 year period. Except for the two events on December 22, 2003 and September 28, 2004, and the slow relaxation

after the latter, the dilation appears constant, with daily random fluctuations of order 10^{-4}. A correlation coefficient X of 0.8 predicts a rms fluctuation, equation 6.4, of 10^{-3}. On averaging over 78 pairs, this prediction is reduced by a factor $\sqrt{78}$, to 1.1×10^{-4}, consistent with the observed fluctuations in ε. In light of the approximations, in particular that of modeling the spectrum as Gaussian and the waveform as stationary, we count this as excellent agreement.

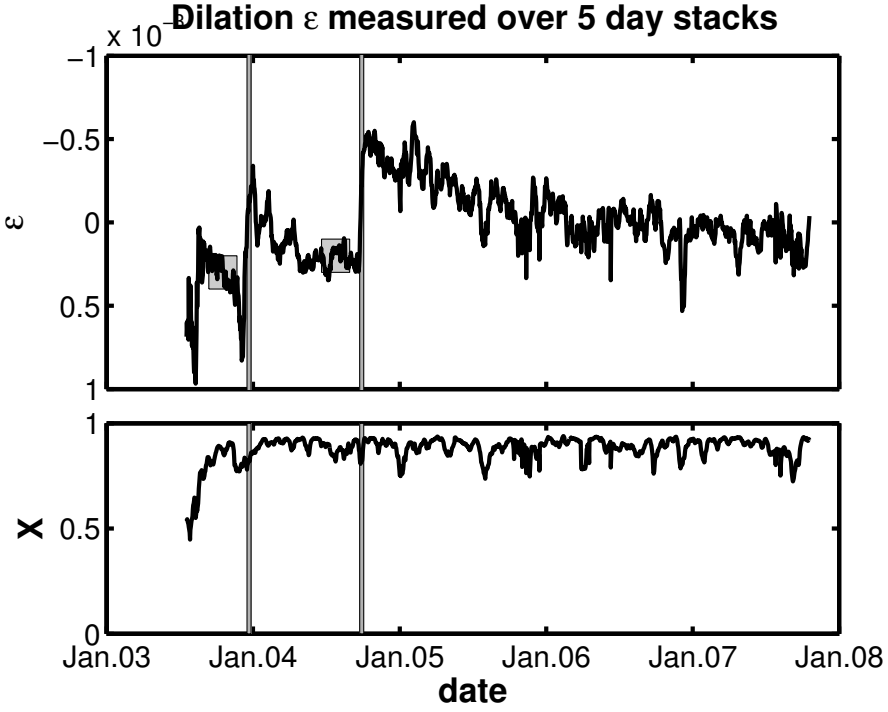

FIG. 6.1 – Top : Dilation ε averaged over 78 receiver pairs, using a 5-day sliding window. The grey squares indicate the 70-day reference windows. The best fit ε varied weakly and stochastically over this period, with two notable jumps, after December 22, 2003 and after the Parkfield earthquake on September 28, 2004. The latter jump was followed by a slow recovery. Fluctuations have an rms strength of about 10^{-4}. Bottom : Dilation coefficient X. the maximum value of the dilation coefficient X, averaged over 78 receiver pairs.

The discontinuities in ε at December 22, 2003 and September 28, 2004 are of particular interest. The latter is coincident with the Parkfield earthquake. Jumps in dilation on those dates by $\sim 0.8 \times 10^{-3}$ were interpreted as decrease of local seismic wavespeed. But one might wish to entertain the hypothesis that these jumps are due to a change in the source of the noise.

To examine the question, we evaluated X and ε using correlation waveforms ϕ_1 as averaged over a 70-day period before each event as a reference and correlation waveforms ϕ_2 obtained over a series of 5 day spans after the events. The relative dilation across the events are the same as seen in figure 6.1, of order 5×10^{-4}. The

values of X for these pairs of waveforms varied between 0.6 and 0.7. According to equation 6.4, divided by $\sqrt{78}$ the value of X would have had to be below 0.33 if this large and apparent dilation were to be a random function of the field having changed in a manner unrelated to actual dilation. The relative dilation between correlation waveforms before and after the event is therefore due to changes in seismic Green's function, and not to changes in the source of the waves.

6.5 Conclusion

An expression was derived for the rms of the apparent dV/V measured on two waveforms, when there is no actual dilation between the two. This apparent dilation can be an effect of *e.g.*, a change in noise sources. The rms value thus allows us to distinguish between an erroneous dV/V measurement due to waveform change, and a physical wavespeed change in the medium.

We have tested the validity of the rms value using data from the laboratory experiments from chapter 5, and we find that the theory predicts errors well.

Next, we have applied the error calculation to the dV/V measurements performed on Parkfield (in chapter 4). We find that the dV/V drops associated with the two events (San Simeon in 2003, Parkfield in 2004) are significantly larger than the rms value predicted. It is therefore safe to say that we measure a velocity change in the medium.

Chapitre 7

Parkfield II : Improving the temporal resolution

Contents

7.1 Summary **71**
7.2 Improving the temporal resolution **73**
7.3 Introduction **73**
7.4 Parkfield Data **76**
7.5 Method : Adaptive Filter **78**
7.5.1 The S-transform 78
7.5.2 Construction of the Self-Filter 79
7.6 Method : Doublets & Stretching **80**
7.7 Results **81**
7.7.1 Velocity Variations from Doublets 82
7.7.2 Velocity Variations from Stretching 83
7.8 Beamforming **85**
7.9 Error calculation **88**
7.10 Discussion **88**
7.11 Conclusion **89**

7.1 Summary

The laboratory experiments in the chapter 5 have shown that it is possible to measure global velocity changes on cross-correlations which have not converged to the Green's function. This result holds as long as the medium is sufficiently diffusive and the noise sources stay stable in time.

Unlike in imaging, a fully reconstructed Green's function is not a prerequisite for monitoring. So, instead of averaging over long periods of seismic noise to obtain a 'correct' Green's function, we can measure velocity changes on shorter cross-correlations.

In the following, I will apply this to improve the temporal resolution of the dV/V measurements on the same seismological data used in chapter 4.

One important disadvantage of using shorter temporal averages in cross-correlations, is that the resulting signal will present more random fluctuations – recall that the fluctuations scale with the square root of the amount of data used (section 5.1).

As seen in section 5.5.3, the stretching method will result in more robust dV/V measurements in the case of low quality data. In addition to using the stretching method, an adaptive filter is introduced to improve the SNR of the cross-correlations [Baig et al., 2009].

Another restriction encountered in chapter 5 is that the spatial distribution of noise sources must remain stable throughout the measurements. Therefore, the orientation of the strongest ambient noise sources at Parkfield is tracked using beamforming. Chapter 6 presented an estimation for the apparent dilation measured when no actual velocity change occurs. This quantity can help distinguish between velocity variations dV/V related to a physical change in the medium, and those related to a change in the waveform. In the following, we use the estimate to identify the significant dV/V fluctuations, and investigate if they relate to the noise source distribution.

7.2 Improving Temporal Resolution in Ambient Noise Monitoring of Seismic Speed

Authors :
C. Hadziioannou, E. Larose, A. Baig, P. Roux, M. Campillo

Abstract

The use of ambient seismic noise has been intensively investigated to perform passive tomography as various scales. Besides passive tomography, passive monitoring is another application of seismic noise correlation as was shown by the recent observation of postseismic velocity changes around the San Andreas Fault in Parkfield, California. One of the drawbacks of using ambient noise correlation for passive monitoring is the need to average the correlations over a long time period in order to obtain a sufficient signal-to-noise ratio (SNR) for the phase fluctuations to be measured accurately. For the application to passive monitoring, one wants the possibility of following short-term velocity variations (one day or less) using noise correlation functions calculated on short time windows. Another difficulty may then appear when the spatial distribution of noise sources also evolves with time. The aim of this paper is to introduce an adaptive filter to the Parkfield dataset in order to improve the SNR output of the ambient noise correlation functions. When applied to passive monitoring, the temporal resolution can be increased from 30 days up to 1 day. With this improved temporal resolution, the velocity drop observed at Parkfield is shown to be cosesimic with the September 24, 2004 $M_W = 6.0$ event. The relationship between the measured velocity fluctuations and the time-evolution of the spatial distribution of the noise wavefield is also investigated. Finally, the error bar in the amplitudes of the velocity variations are compared with a theoretical expectation.

7.3 Introduction

It was observed that the two-point cross-correlation between long records of ambient seismic noise yields the Green's Function (GF) between the two stations (*e.g.* Shapiro and Campillo [2004]). This property is expected when noise sources are distributed isotropically around the stations which is eventually the case when the ambient noise correlation is integrated over a long time [Weaver and Lobkis, 2004; Sanchez-Sesma and Campillo, 2006; Wapenaar, 2004; Roux and Kuperman, 2004]. However, these optimal conditions are almost never fulfilled in seismology as the noise sources (primarily oceanic, Gerstoft and Tanimoto [2007]; Landès et al. [2010])

are distributed unevenly. The consequence is that the Green's function is only partially reconstructed, and that a certain amount of unpredicted fluctuations remain in the long-time averaged noise correlation. However, using dense network of seismic stations, the large number of correlation pairs provides enough redundancy from the data to counterbalance the relative inaccuracy of travel-time measurements extracted from noise correlation. As a matter of fact, seismic tomography based on noise correlation has been performed successfully at various scales ranging from kilometers to hundred of kilometers [Shapiro et al., 2005].

Another application of seismic noise correlation is the monitoring of seismic velocity variations. Indeed, an advantage of using noise correlation to retrieve the Green's function is that it is a continuous measurement. This allows to track temporal changes from a set of correlation functions calculated on successive time windows of noise recordings. For example, by looking at small phase changes in the signals extracted from noise correlation, we may detect velocity changes occurring in the medium sampled by the seismic waves. In practice, the coda portion of the noise correlation is used for measuring seismic velocity changes. The coda waves have been scattered throughout the medium, and have accumulated the delays due to a velocity change along their trajectories. This makes them more suitable to measuring velocity variations than the direct waves.

What makes this use of noise correlation even more appealing is the work performed by Hadziioannou et al. [2009] through laboratory experiments that showed that passive monitoring was successful without completely reconstructing the GF from cross-correlations. This means that, contrarily to passive imaging, passive monitoring would be viable with a few stations and an uneven distribution of noise sources.

Actually, two ingredients are necessary for passive monitoring. First, measuring accurate phase variations between similar signals requires a good signal-to-noise (SNR) ratio. In particular, the velocity variations associated with earthquakes are very subtle – of the order of 0.1% relative change – except for the non-linear response of unconsolidated materials at the surface [Peng and Ben-Zion, 2006; Rubinstein et al., 2007a; Niu et al., 2003] or in highly damaged fault zones [Li et al., 2007]. Since the coda waves strongly contribute to the accuracy of phase variation measurements, it is therefore challenging to obtain a good SNR on this part of the correlation function that is classically of much lower amplitudes than the direct waves. Second, since the spatial distribution of seismic noise is uneven, the correlation function may evolve with time as the noise sources are modified [Froment et al., 2010]. For example, seasonal changes of ocean noise directivity have been observed, whose effect on the direct arrivals of the noise correlation function is comparable or of greater amplitude than an actual change of the medium velocity.

Going back to the SNR issue, improving SNR in the seismic noise correlation function means averaging over longer noise time series of typically weeks or months

TAB. 7.1 – Overview of the different timescales used in this paper.

designation	typical duration	definition
T	0.1 – 1 s	Dominant period of the correlated signal
t	10 – 120 s	Lapse time of the correlated signal
T_{SNR}	1 – 30 days	Averaging time of cross-correlation ; stack length.
T_{noise}	days – months	Evolution timescale of the noise sources
T_{medium}	months – years	Evolution timescale of crustal properties

[Larose et al., 2008; Sabra et al., 2005a]. This need for long averages might be problematic though, since we would like to follow short term variations in the medium as well. In particular, Brenguier et al. [2008a] have measured the velocity changes occurring around an array near Parkfield, California, in the period spanning from 2003–2007. They observed drops in seismic velocity around the array which seem to coincide with the 2004 $M_W = 6.0$ Parkfield earthquake, as well as with the 2003 $M_W = 6.5$ San Simeon earthquake. However, since the noise was averaged over 30 days to retrieve the Green's function, it is very difficult to say if the observed changes are coseismic or slightly delayed or advanced.

As for the time evolution of the noise source distribution, one may claim that the coda part of the noise correlation function will be less sensitive to the spatial distribution of the noise sources than the direct waves as was experimentally shown at the laboratory scale [Hadziioannou et al., 2009].

In conclusion, the key issue for passive monitoring is the combination of a strong SNR on strongly-scattered waves extracted from noise correlation. To reach such condition, different timescales play a role in the success of passive monitoring which will be discussed throughout the paper (see table‘7.1) : T_{SNR} is the averaging time of the noise correlation function, T_{medium} is the time evolution of the medium properties (the local velocity change after an earthquake, for example) and T_{noise} is the time evolution of the spatial distribution of the noise sources.

In this paper, we revisit the 2003–2007 Parkfield data introducing a new processing algorithm with the objective to improve the temporal resolution of the velocity change measurements. The goal of the processing is to improve the SNR of our signals while keeping short temporal averages. The paper is structured as follows : in the next section (section 7.4), we discuss the data set and the signal processing methods previously applied on the noise data. Then, (section 7.5), we introduce an adaptive filter to improve the SNR of noise-extracted correlation functions, which increases the temporal resolution of velocity variation measurements (sections 7.6 and 7.7). We then investigate if the origin of the velocity variations can be attributed to changes in the ambient noise source distribution (section 7.8). Finally, in section 7.9 we introduce an expression for estimating the errors made on velocity variation measurements. Conclusion is that the velocity drop observed with waves

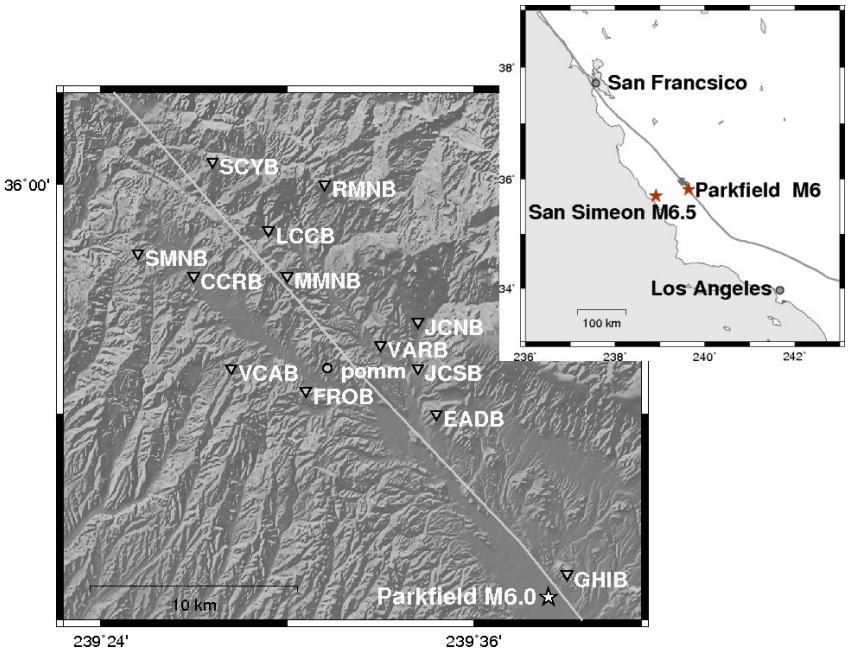

FIG. 7.1 – Location of the HRSN stations (white and black triangles) near Parkfield, California. In the inset figure, the locations of the 2003 San Simeon and 2004 Parkfield earthquakes (stars). The white and black circle indicates the location of the GPS station `pomm`.

in the band from 0.1 to 0.9 Hz at the Parkfield earthquake is coseismic, and that the noise field distribution has no influence on the velocity variations observed when using the coda of the signal.

7.4 Parkfield Data

The data used in this study is recorded at the Berkeley High Resolution Seismic Network (HRSN[1]) near Parkfield, California. This network consists of 13 borehole stations which have been recording continuously since July 2001. The borehole depths range from 60 m to 300 m, which helps reduce surface effects such as temperature variations and precipitation. The location of the stations and these two earthquakes is shown in Figure 7.1. For each pair of stations, we consider the continuous record between the 1st of August 2003 and December 31st, 2006. In this period, the $M_W = 6.5$ San Simeon earthquake occurred on 22 December 2003, as well as the $M_W = 6.0$ Parkfield earthquake of September 28, 2004.

[1]More information concerning the Parkfield HRSN can be found at `http://seismo.berkeley.edu/bdsn/hrsn.overview.html`

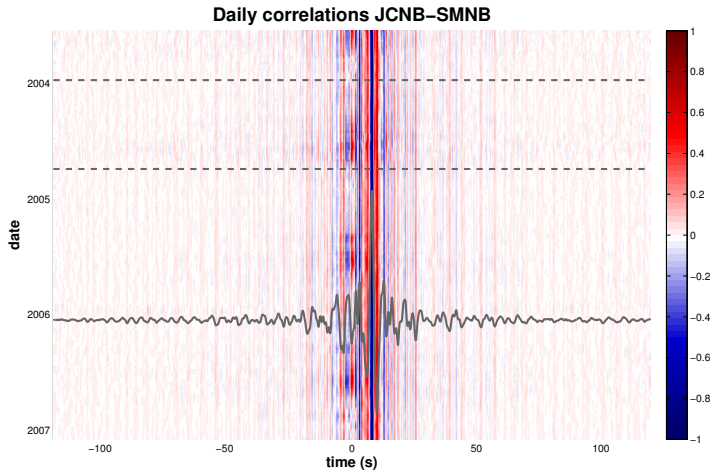

FIG. 7.2 – Cross correlation signal for JCNB-SMNB, stacked with a 30-day sliding window. Overlain in gray is the reference trace for this station pair. The gray horizontal dashed lines represent the dates of the San Simeon earthquake (22 December,2003) and the Parkfield earthquake (28 September, 2004).

The noise signal recorded at each station is whitened between [0.1 0.9] Hz and is 1-bit digitized. The daily cross-correlation is then computed for each of the 78 station pairs as well as the 13 autocorrelations, for lapse times between -120 and +120 seconds.

Initially, in an effort to improve the SNR, the daily cross-correlations are stacked with a sliding window of 30 days, which is shifted 1 day at a time. Later on, sliding window stacks of 1 and 5 days are used as well. An example of the signals obtained for a 30 day sliding window for one station pair (JCNB-SMNB) is shown in Figure 7.2. For each station pair, we define a reference correlation as the average of the correlations for the whole 1248 day measurement period. The temporal evolution of the seismic velocity can be measured by comparing the coda of the reference correlation to that of the shorter stacks. Temporal variations are measured using two different methods, as detailed in section 7.6.

In Figure 7.2, seasonal variations are visible on the ballistic waves of the cross-correlation as an asymmetric change in intensity. This suggests a seasonal change in noise source, as will be investigated in section 7.8. Note that this intensity variation is not visible in the coda part of the signal.

7.5 Method : Adaptive Filter

In an attempt to improve the SNR of the noise correlations, thereby increasing the temporal resolution, an adaptive filter (developed by Baig et al. [2009]) is applied to the correlations before retrieving the velocity variations.

7.5.1 The S-transform

The algorithm used is based on the S-transform, as developed by Stockwell [Stockwell et al., 1996]. The analytical S-transform of a continuous function of time $x(t)$, noted as $S\{x\}(\tau, f)$, is defined as :

$$S\{x\}(\tau, f) = \frac{1}{\sqrt{2\pi}} \int_{-\infty}^{\infty} x(t)|f| \exp\left[-\frac{(\tau - t)^2 f^2}{2} - i2\pi f t\right] dt, \tag{7.1}$$

which transforms the signal $x(t)$ into a time-frequency domain (τ, f).

The Gaussian envelope function ($\exp[-(\tau - t)^2 f^2/2]$) localizes in time, and is translated along the signal. In the meantime, the oscillatory exponential kernel $\exp[-i2\pi f t]$ fixes the frequency being analyzed, and does not translate. This allows the S-transform to find the amplitude and phase independently. In other words, the S-transform not only estimates the local power spectrum, but also the local phase spectrum.

For a discrete, real signal $x(t)$ with N points, the S-transforms need to be evaluated at $N^2/2$ points in time-frequency space. Stockwell [2007] developed the Discrete Orthonormal S-transform (DOST) to reduce the number of evaluations necessary. The N-point signal is projected onto a series of N complex basis functions $x_k[\tau, f]$; $k = 1 : N$, with each function mapping to a localized patch of time-frequency space described by its frequency, f, and a time lag, τ. These basis functions form an orthonormal set. Like its parent S-transform, DOST allows both straightforward manipulation of signals from time to time-frequency while preserving the phase of the signal.

Both the analytical S-transform and the DOST are linear, which is beneficial in application to noise discrimination. Modelling a recorded time series, $x(t)$ as signal, $g(t)$, corrupted with noise, $n(t)$, (*i.e.*, $x(t) = g(t) + n(t)$), the S-transform of the signal ($S\{x\}(\tau, f)$) becomes :

$$S\{x\}(\tau, f) = S\{g\}(\tau, f) + S\{n\}(\tau, f) \tag{7.2}$$

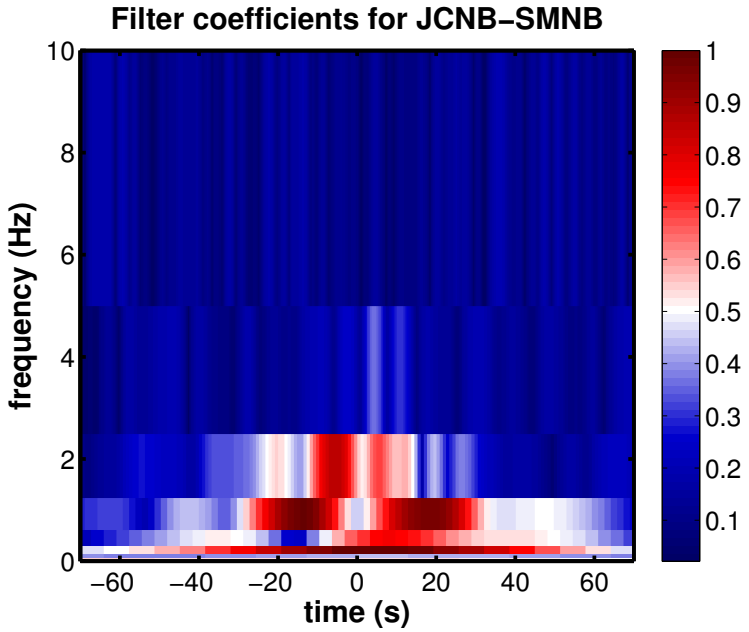

FIG. 7.3 – The absolute value of the coefficients of DOST basis vectors for the reference signal for JCNB-SMNB with each number coefficient plotted at its appropriate patch of time-frequency space. The colorscale ranges from white - representing zero amplitude - to dark red for the highest amplitudes.

Provided the signal and noise occupy different portions of time-frequency space, the absence of cross-terms in equation 7.2 potentially allows for the noise cancellation. We shall exploit this property in section 7.5.2.

7.5.2 Construction of the Self-Filter

To construct a denoising filter based on the data itself we use the linearity property of the S-transform, as shown in equation 7.2. The challenge is to identify the signal $g(t)$ when only the noisy timeseries $x_i(t)$ are measured. Suppose we have M records of the same timeseries, $x_i(t)$. When we average over all these $x_i(t)$, and assume a random noise, the noise part of the record should tend to 0 as the number of records approaches ∞, and only the signal remains. We can see that with equation (7.2) the S-transform of the timeseries becomes :

$$\langle S\{x\}(\tau, f)\rangle = S\{g\}(\tau, f) + \frac{1}{M}\sum_{k=1}^{M} S\{n_k\}(\tau, f) \tag{7.3}$$

where $\langle . \rangle$ represents a normalized sum over the signals $\frac{1}{M}\sum_{i=1}^{M}$. The second term in equation 7.3 disappears as $M \to \infty$.

We can now construct a phase coherence filter F, inspired by the method used in Schimmel and Paulssen [1997], using the 'cleanest' possible signal $x(t)$. The signal $x(t)$ is decomposed into its DOST basis vectors x_k. The normalized, complex values of these basis vectors are stacked :

$$F(\tau, f) = \left| \frac{1}{N} \sum_{k=1}^{N} \frac{S\{x_k\}(\tau, f)}{|S\{x_k\}(\tau, f)|} \right|^{\nu}, \tag{7.4}$$

The parameter ν can be used to control the strength of the filter. In this paper, $\nu = 0.5$.

In this case, the reference stack takes the role of the clean signal $x(t)$ used in equation (7.3) and is used to construct the filter for each station pair. Each daily cross-correlation is then S-transformed, filtered according to :

$$\int_{-\infty}^{\infty} S\{x_i\}(\tau, f) F(\tau, f) d\tau = X_i(f), \tag{7.5}$$

and finally transformed back to the time-domain.

A drawback of the analytical S-transform (equation 7.1) is that it is computationally expensive to calculate. In practice, we apply the DOST transform to our signals in order to gain on computing time.

7.6 Method : Doublets & Stretching

Two processing techniques have been proposed in the literature to estimate relative velocity changes dV/V in the coda of the correlations.The first one, the doublet technique, was developed by Poupinet et al. [1984]. It is also known as cross-spectral moving-window technique (CSMWT, Frechet et al. [1989]), and in practice computes the phase shift between records for consecutive, overlapping time windows Δt. For a given window Δt, the time shift δt is assumed to be constant and is estimated in the frequency domain by measuring the Fourier cross-spectrum phase. This estimator uses an accurate, unbiased Wiener filter technique [Jenkins and Watts, 1969] and produces an estimate whose confidence interval is controlled by the coherence values in the frequency band used for the analysis. The method can then measure arbitrary time-shifts between two records with enough similarity (or coherence). It is consequently possible to represent the time-shift δt versus time t in the coda. The actual velocity variation is simply the average slope of $\delta t(t)$: $dV/V = -\delta t/t$. The key parameter in this analysis is the Fourier transform window length Δt, which is the time-window over which the time-delay is measured. On one hand, large time windows include more data, thus averaging down the fluctuations of δt due to noise.

This results in more accurate measurements. On the other hand, the approximation that the time-shift is constant within the given time-window is getting more erroneous when the window length is increased. The choice of Δt is therefore a trade-off between time-shift accuracy, and the time resolution between two consecutive measurements.

This processing found remarkable applications in seismology, including recent developments in ambient noise seismology [Brenguier et al., 2008b,a].

Another idea [Lobkis and Weaver, 2003; Sens-Schönfelder and Wegler, 2006] is to interpolate the coda at times $t(1-\varepsilon)$ with various stretching factors ε.

The actual relative velocity change is the stretching factor $\varepsilon_0 = dV/V$ that maximizes the cross-correlation coefficient :

$$X(\varepsilon) = \frac{\int_{t_1}^{t_2} h\left[t(1-\varepsilon)\right] h_0[t]dt}{\sqrt{\int_{t_1}^{t_2} h^2\left[t(1-\varepsilon)\right] dt . \int_{t_1}^{t_2} h_0^2[t]dt}}, \tag{7.6}$$

where t_1 and t_2 the start and end time of the coda used, respectively.

One drawback is that this latter processing assumes a linear behavior δt versus t, equivalent to a homogeneous relative velocity change $dV/V = \varepsilon$. This is sometimes not the case in complex media. But this technique has also a noticeable advantage : whole data is processed at once, which is found to result in a more stable, and thus more precise, estimation of dV/V. In particular, we showed from laboratory experiments that the stretching technique is more adapted to data with low signal-to-noise ratio [Hadziioannou et al., 2009]. It was also found very useful for noisy seismic correlations on the moon [Sens-Schönfelder and Larose, 2008]. Another interesting feature of the stretching technique is to provide the remnant coherence $X(\varepsilon)$. This coherence indicates if noise sources are stable or changing over the period of observation of interest : $X \sim 1$ means absolutely stable sources, $X << 1$ means that sources locations are changing. X also indicates the quality of the ε estimation (see section 7). In the case of Parkfield, we end up with a dV/V resolution of 10^{-3} for measurements on 1 day stacks, and up to $2 \cdot 10^{-4}$ for 30 day stacks (section 7.9).

7.7 Results

The adaptive filter is tested with the two methods (doublets and stretching) for retrieving velocity variations detailed in section 7.6. Both analyses are done on cross-correlations bandpassed for [0.1 0.9]Hz.

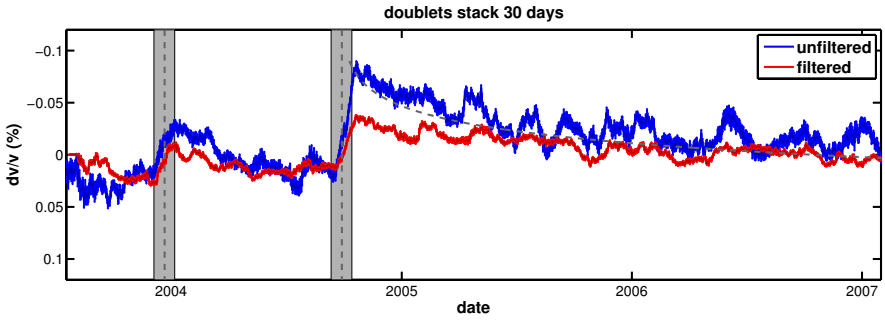

FIG. 7.4 – dV/V using the doublet method, for a stack of 30 days. In blue : using the original data, in red : after applying the adaptive filter. The dashed line represents displacement measurements along the fault measured at the `pomm` GPS station (Figure 7.1). The first vertical dashed line indicates the date of the San Simeon earthquake, the second that of the Parkfield earthquake.

7.7.1 Velocity Variations from Doublets

In the doublet analysis the time shift δt is measured for 100 windows of $\Delta t = 10$s, which are shifted by 1 second. A slope is then fitted along the measurements for time windows ranging from -120s to -20s and +20s to +120s in the cross-correlation signal. The window from -20s to 20s is excluded, in order to minimize effects from the direct waves.

Figure 7.4 shows the relative velocity changes obtained with the doublet method on 30 day stacks (which slide by 1 day), before (blue) and after (red) application of the adaptive filter. We can see that while the dispersion of the measurements is reduced, as seen by the reduction of the errorbars, the overall values of velocity change measured are reduced. This follows from the way the doublet method retrieves the time lag in the frequency domain [Poupinet et al., 1984]. The delay of each small window of the signal is measured by fitting a line to the phase-frequency behavior in the cross-spectrum of the signal and its reference. In Figure 7.3, the absolute value of each of the N DOST basis vectors is portrayed on its corresponding time-frequency space. In a way, it represents the absolute value of the DOST basis function for the reference signal of station pair JCNB-SMNB. In this figure, it is visible that the adaptive filter applies different filtering coefficients for different frequencies, which affects this linear phase-frequency behavior. Since the doublet method measures the time delay by fitting a linear regression to the phase-frequency, this way of filtering interferes with the measurements.

This lower amplitude of the dV/V is a disadvantage of the adaptive filter when it is used in combination with the doublet technique. However, in some cases it can

be useful to use the filter to increase the SNR and thereby the temporal resolution. This way, it is possible to pinpoint the date at which a change occurred, even if the amplitude is wrong. For stacks shorter than 10 days, the SNR of the signals become too small to apply the doublet method, even after filtering.

7.7.2 Velocity Variations from Stretching

The stretching technique measures the dilation of the signal using as much of the coda as possible (see equation 7.6) – in this case, from 20s to 120 s. This renders the technique less sensitive to fluctuations in the correlations.

In Figure 7.5a we show the velocity changes measured with the stretching method using 30 day stacks, with and without application of the filter. Again, we remark an improvement of the errorbars (detailed in section 7.9) and a reduction of fluctuations after applying the filter. However, unlike in the case of the doublet method, the filter does not degrade the amplitude of the variations measured. In Figure 7.5b, we observe the same with a stack of 5 days. Note that the postseismic behavior is still consistent with the postseismic slip as measured by Freed [2007] from GPS measurements [2]. Another improvement by the filter can be seen when reducing the stack length to only 1 day (Figure 7.5c). Here, when using the unfiltered signal, the velocity drops associated with the San Simeon and Parkfield earthquakes can be observed, but they become much clearer in the case of the filtered signal. This is especially apparent when we look closely at the velocity behavior around the date of the Parkfield earthquake (Figure 7.6). The measurements from the filtered signals show that the velocity one day after the earthquake has dropped to a lower value, and recovers slowly.

Note that the ambient noise on the day of the earthquake is altered by numerous aftershocks and the mainshock itself. After elimination of these parts of the noise, not much data remains to work with on that day, thus producing an unreliable correlation signal. From these observations (Figure 7.6), we can safely conclude that the velocity drop we measure has its maximum at the time of the Parkfield earthquake [Rubinstein and Beroza, 2005].

Stretching, especially in combination with the adaptive filter to remove as much noise from the signals as possible, allows to greatly improve the temporal resolution of the measurements.

[2] More information concerning the USGS GPS network at Parkfield can be found at `http://earthquake.usgs.gov/monitoring/edm/parkfield/continuous.php`

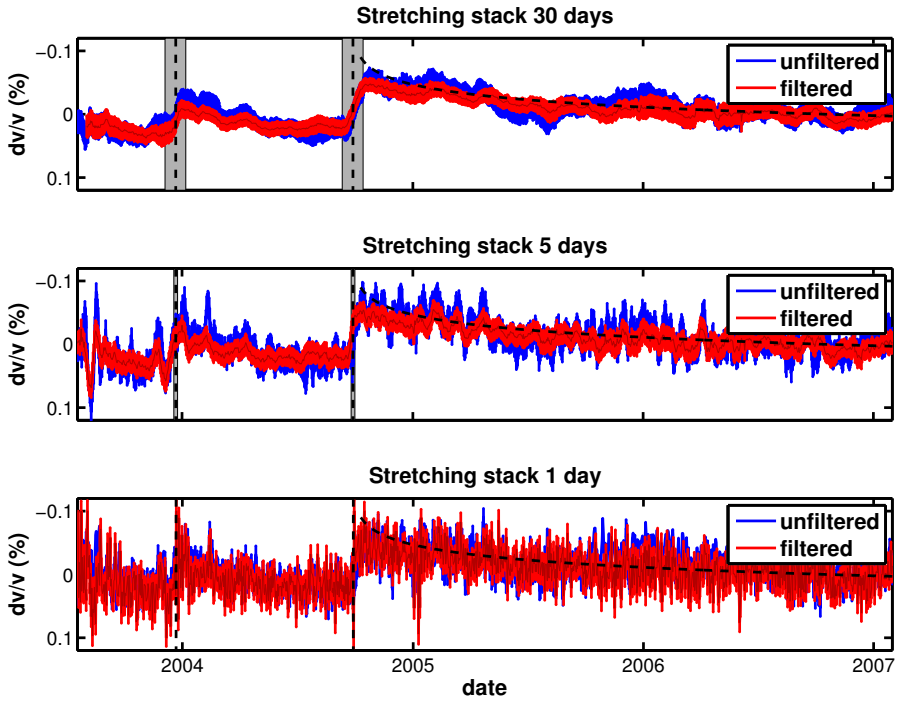

FIG. 7.5 – dV/V using the stretching method, for a stack of 30 days (top), 5 days (center) and 1 day (bottom). In blue : using the original data, in red : after applying the adaptive filter. The black dashed line represents displacement measurements along the fault measured at the `pomm` GPS station (Figure 7.1). The first gray shaded area/black dashed line indicates the date of the San Simeon earthquake, the second that of the Parkfield earthquake.

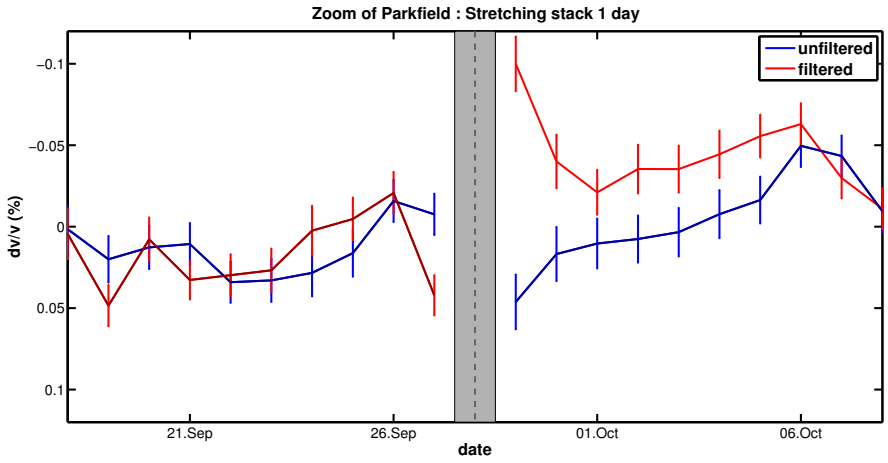

FIG. 7.6 – dV/V using the stretching method, for a stack of 1 day, zoom around Parkfield earthquake (28 September, 2004). In blue : using the original data, in red : after applying the adaptive filter. The gray shading represents the day of the earthquake. Due to the many aftershocks this day interfering with the background noise, the dV/V measurement is unreliable. The points for the day of the earthquake are therefore not plotted.

7.8 Noise Source Location from Beamforming

After the previous discussion on the improvement of the temporal resolution of the dV/V measurements, we study if the observed fluctuations in the velocity can be explained by the change in noise source distribution. We observe on the example of cross-correlations of couple JCNB-SMNB (Figure 7.2) that the direct waves are sensitive to seasonal variation, probably due to variations in the noise source distribution. According to the theory [Gouédard et al., 2008; Froment et al., 2010; Paul et al., 2005], we expect any strongly directive and varying part of the noise field to influence the Green's function reconstruction negatively and thus alter the dV/V measurement.

In order to establish if any such strong moving sources exist around the Parkfield array, we investigate the structure and evolution of the ambient noise field. To do so, we perform plane wave beamforming (as described by Roux [2009]) on 1-day segments of ambient noise in the [0.1 0.2]Hz frequency band which contains the secondary microseism peak. Figure 7.7 shows an example of the angular-speed distribution of the background noise on this frequency interval.

We observe that the ambient noise field at Parkfield is very directive and dominated by a component propagating to $\sim 50°$ clockwise from North with an apparent around

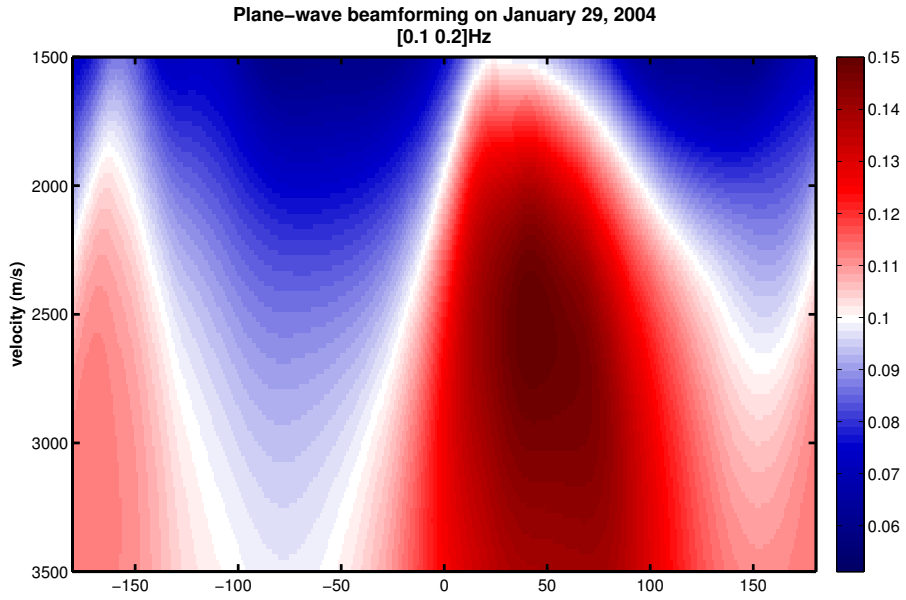

FIG. 7.7 – Beamforming spot at [0.1 0.2]Hz. Azimuth in degrees clockwise from North.

2500 m/s. This means that it consists mostly of surface waves originating from the direction of the Pacific Ocean, in agreement with results from similar analyses by Roux [2009].

We track the azimuthal variation of the most prominent maximum in Figure 7.8a. In order to quantify the temporal change of the beamformer output, we calculate its daily coherence with respect to the beamformer output averaged over the three years of data (Figure 7.8b).

Do the azimuthal variations of the dominant source, or variations of the noise field coherence, reflect on the dV/V measurements ? In Figure 7.8, we have plotted the azimuthal variation of the strong source at [0.1 0.2]Hz, as well as the noise field coherence (a and b) along with the dV/V measurements and the wavefield coherence (c and d).

From Figure 7.8a, some seasonal variations in the azimuth of the beamformer output is visible, reminiscent of the variations seen on the cross-correlations in Figure 7.2. However, one can see that the change in noise direction does not influence the dV/V measurements. On the other hand, the change in noise field structure, expressed as a decoherence in Figure 7.8b, does relate to a change in correlation waveform (Figure 7.8d). As seen in section 7.6, this decrease in waveform coherence as the source distribution changes, is expected. In some cases, such as in the beginning of 2005,

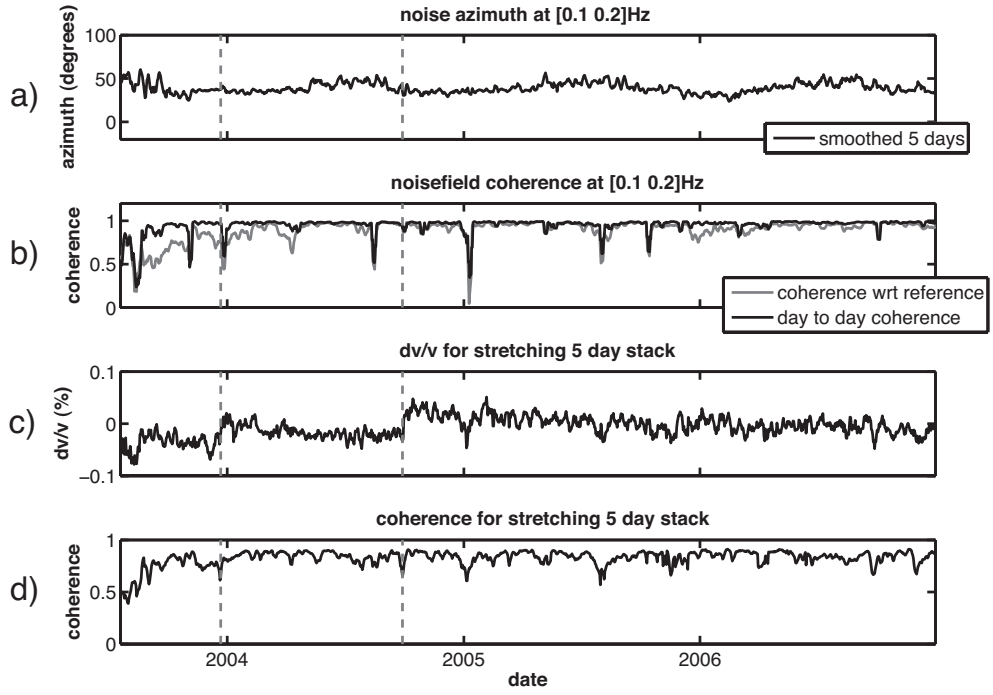

FIG. 7.8 – (a) The maximum ambient noise azimuth (in degrees clockwise from North) and (b) the noise field coherence, both at [0.1 0.2]Hz. (c) The velocity variations as well as (d) the correlation waveform coherence for a 5-day sliding stack. The gray vertical dashed lines represent the dates of the San Simeon earthquake and that of the Parkfield earthquake, respectively.

a strong change in noise sources has even led to more noise and fluctuations in the dV/V measurements. This effect of decreased waveform coherence on the measurements is included in the expected rms fluctuations, as can be seen in section 7.9.

In conclusion, a change in noise wavefield incidence does temporarily result in a noisier dV/V measurement. Since such a change is also visible as a decoherence of the waveform these periods of time can be detected and treated accordingly.

7.9 Error calculation

The precision with which a dilation coefficient ε is retrieved depends on the strength of correlation between two signals. Weaver et al. [2009b] derived an expression to predict the fluctuations in dilation coefficient due to *e.g.* changes in the noise source, in the case where the velocity in the medium has not changed :

$$\mathrm{rms}(\varepsilon) = \frac{\sqrt{1-X^2}}{2X}\sqrt{\frac{6\sqrt{\frac{\pi}{2}}T}{\omega_c^2(t_2^3-t_1^3)}}, \tag{7.7}$$

where ε is the dilation, X the coherence of the waveform after dilation, between starting time t_1 and end time $t2$. T is the half bandwidth, with ω_c the center frequency of the signal.

In the case of the data used in this paper, this boils down to :

$$\mathrm{rms}(\varepsilon) = 3\times10^{-3}\frac{\sqrt{1-X^2}}{2X}, \tag{7.8}$$

as detailed by Weaver et al. [2009b]. Since we average the measurement over 91 station pairs, this rms value is reduced by $\sqrt{91}$, which leads to a rms of the order of 1×10^{-4} for a wavefield coherence around $X = 0.8$. If the dilation measured exceeds this rms value, we can conclude that it is indeed due to a velocity change in the medium. We find that in the case of the Parkfield data, the velocity variations measured are larger than the predicted fluctuation value of ε for a correlation coefficient of X. This means that they are due to a local velocity change and not due to source variations.

7.10 Discussion

By improving the temporal resolution of our dV/V measurements using an adaptive filter and the stretching technique, we have shown that the velocity drop observed at

Parkfield is coseismic. The increased in temporal resolution obtained in this paper allows us to track velocity changes immediately after the event.

Similar, albeit stronger, coseismic velocity drops have been observed and are generally associated with shallow damage in either the crust [Rubinstein and Beroza, 2004; Sawazaki et al., 2009; Peng and Ben-Zion, 2006; Niu et al., 2003] or the fault zone [Li et al., 2003]. These shallow effects are modeled by a strong drop in shear modulus (and thus velocity drop) very shortly after the mainshock, followed by a postseismic logarithmic healing curve.

It could be argued that we observe this same effect. The lower amplitude of velocity drop – on the order of 0.1% instead of 30% – could be the result of averaging a localized effect over a larger volume, seeing as we measure the change with multiply scattered coda waves.

However, if the velocity drop we observe were due only to superficial damage, we would expect the drop amplitude to become higher as we measure closer to the event (1 day as opposed to 30 days). As seen in Figure 7.5, this is not the case.

In fact, the postseismic relaxation behaviour closely follows along-fault displacement deduced from GPS measurements [Freed, 2007; Johanson et al., 2006]. This suggests the possibility that not shallow, but deeper, stress-related effects are involved here.

Apart from the velocity drop at the PF event, some small velocity fluctuations remain. As shown in section 7.9, these fluctuations are larger than the error expected on dV/V, and should have a physical origin. Since our GF is not perfectly reconstructed, these fluctuations could be due to a change of the sources. In section 7.8, we find no direct relation between the dominant noise direction and the dV/V measurements (Figure 7.8). However, the amount of decorrelation of the cross-correlations does reflect the stability of the ambient noise wavefield.

7.11 Conclusion

By using an adaptive filter to rid the data of as much noise as possible, and by applying the stretching method to retrieve the velocity variation measurements, we are able to perform monitoring on cross-correlations of only 1 day of ambient noise. Thanks to this, we can show that the 0.1% velocity change observed at the Parkfield event is real and coseismic.

Furthermore, we show that changes in the orientation of the main noise sources do not affect the velocity change measurements directly. The stability of the noise wavefield does relate to the amplitude of fluctuations measured in dV/V.

Chapitre 8

Japan : Distance dependence of velocity variations

Contents

8.1 Introduction 91
8.2 Data 91
8.3 Method : Processing 93
8.3.1 Clock Error Correction 94
8.3.2 Velocity Variation Measurement 97
8.3.3 Coda Coherence 98
8.3.4 Quality Control 99
8.4 Velocity Variations 100
8.4.1 Distance dependence 102
8.5 Discussion & Conclusion 106

8.1 Introduction

In this chapter, the methods developed in this PhD are applied to a different seismic dataset, namely tiltmeter noise recordings from the Hi-Net array in Japan. First of all, it is interesting to see if the results from Parkfield are repeatable for a different earthquake. Furthermore, a spatially larger array allows us to study the distance dependence of the dV/V observed (section 8.4.1).

8.2 Data

The data used in this chapter has been recorded on the dense Hi-Net array that covers most of Japan. After the 1995 Kobe earthquake, an effort started to create a unified seismic observation network covering Japan [Okada et al., 2004; Obara et al., 2005]. The result was Hi-Net (High sensitivity seismograph Network Japan),

a network of seismic instruments spaced by approximately 20 km. The National Research Institute for Earth Science and Disaster Prevention (NIED) operates most of this network, including the data acquisition, monitoring and archive aspects.

The Hi-Net stations are installed at the bottom of 700 boreholes of at least 100 meter depth to ensure high sensitivity observations. Additionally, the installation in the borehole helps to eliminate noise caused by human activity and weather conditions. Each borehole contains a 3-component short-period velocimeter, a 3-component accelerometer and a 2-component tiltmeter.

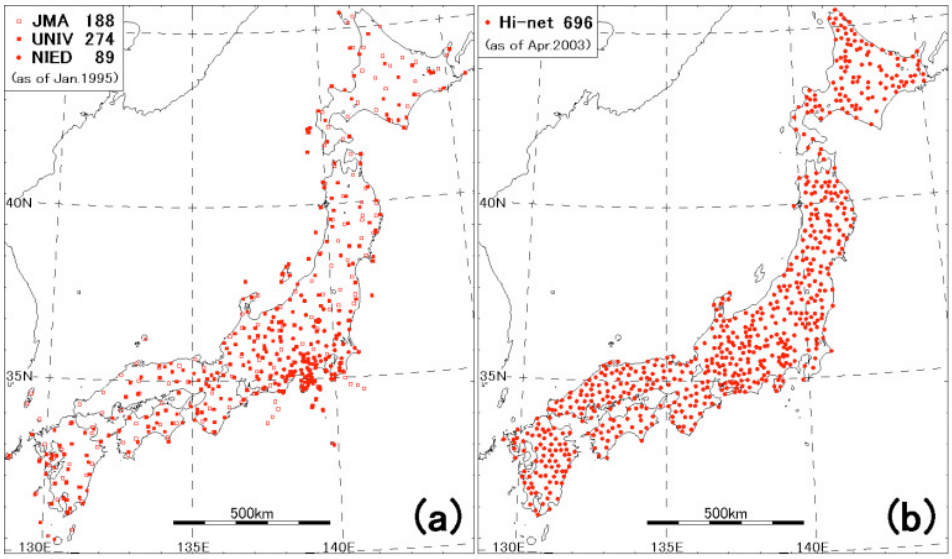

FIG. 8.1 – Distribution of high sensitivity seismic stations in Japan (a) at the time of 1995 Kobe earthquake and (b) newly added Hi-net stations as of April 2003 (JMA : Japan Meteorological Agency, UNIV : University, NIED : National Research Institute for Earth Science and Disaster Prevention). *Source :* Okada et al. [2004]

The 24 stations used in this study are a sub-array of the Hi-Net network. Approximately 2 years of continuous two-component measurements are available for the tiltmeters of these stations, spanning from the start of 2004 to the end of 2005. The size of the raw data amounts to over 2 Tb. On October 23, 2004, a $M_w = 6.6$ event occurred in the Niigata prefecture, in the area of Chuetsu [Hikima and Koketsu, 2005]. The location of its epicenter is indicated by the white star in figure 8.2.

The goal here is to measure any velocity variations resulting from the 2004 $M_w = 6.6$ Chuetsu event. In addition, we will use the full extent of the array we have access to, to see how far the dV/V effect reaches.

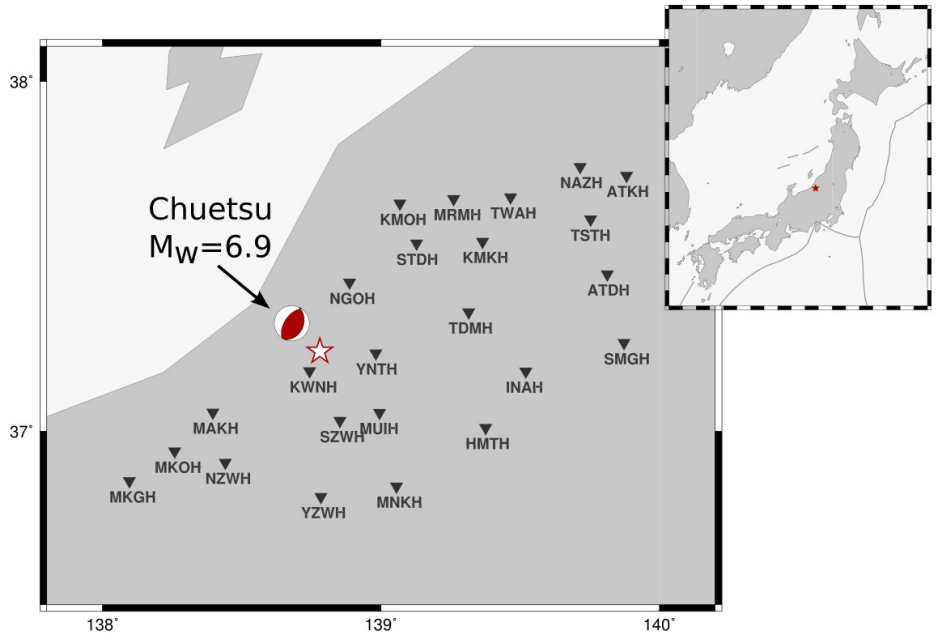

FIG. 8.2 – Location of the tiltmeter stations (grey triangles) used in this study. The Chuetsu event is indicated as a white star, with its focal mechanism in red. Included is an overview map showing the location of the event (red star) in Japan.

8.3 Method : Processing

We use continuous noise recordings from the two horizontal components of the Hi-Net tiltmeters. The seismic noise data is stored in the 'WIN32' format [Urabe and Tsukuda, 1992] with a sampling frequency of 20 Hz, in sections of 1 minute. The first step is to concatenate these sections into noise records of 2 hours. Next, the mean of the signal is removed. Every day, the signals from all the stations exhibit a spike at the same time, likely a side-effect from the synchronization of the station clocks. These spikes are automatically detected and removed using a running window *rms* clipping algorithm.

The spectral content of the noise is studied to find the most promising bandwidth to study. In figure 8.3, we can see that most of the energy in the noise is located around the microseismic peaks, between [0.1 0.3]Hz (see section 2.5).

Spectral whitening is then applied to each noise record using a tapered boxcar between [0.08 0.5]Hz, followed by one-bit digitization in an effort to remove earthquake signatures [Campillo and Paul, 2003; Larose et al., 2004; Bensen et al., 2007]. Finally, the 2-hour noise records are cross-correlated for lag times between -500 and +500 seconds. This results in six cross-correlation functions every day for each com-

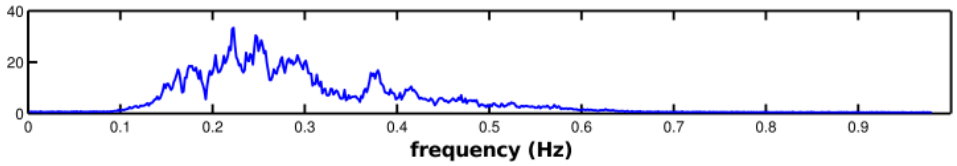

FIG. 8.3 – Typical spectrum of one day of seismic noise recorded at KWNH.

ponent. These six functions are stacked to acquire daily cross-correlations for each of the 276 station pairs as well as 24 daily autocorrelations.

An example of the cross-correlation signals obtained is shown in figure 8.4. This figure represents a collection of 30-day correlation stacks for all station pairs, binned and ordered according to the interstation distance. At negative and positive times, surface waves can clearly be seen propagating with an apparent velocity between 2 km/s and 3 km/s (blue and red dashed lines, respectively). Another arrival can be seen propagating with an apparent velocity larger than 10 km/s (grey dashed lines). According to Landès et al. [2010], such fast arrivals can be interpreted as steep incident P-waves, generated by distant sources.

The relative velocity change is measured with the *stretching* method (described in section 3.3). Each cross-correlation function is compared to a reference. For each station pair, the reference correlation signal is determined by stacking all 730 daily cross-correlations.

To gain a better signal-to-noise ratio (SNR), the daily correlations are stacked using a 30-day sliding window, which is translated by 1 day at a time. These 30-day correlation stacks will be used to measure the dV/V in section 8.3.2.

8.3.1 Clock Error Correction

When the cross-correlation function has completely converged to the Green's function, it should be completely symmetric around zero : travel times are identical on the positive and negative side of the correlation. However, we have seen repeatedly that in seismology, the Green's function is usually not fully reconstructed. When this is the case, 3 phenomena can cause shifts in travel time [Stehly et al., 2007] :

- A physical velocity change results in a longer or shorter traveltime, symmetric on both sides of the correlation function.
- A change in the spatial distribution of noise sources will cause a change in travel time independently on either side of the correlation, as each side is sensitive to a different set of sources.
- A clock error in one of the stations will cause opposite changes in the traveltime

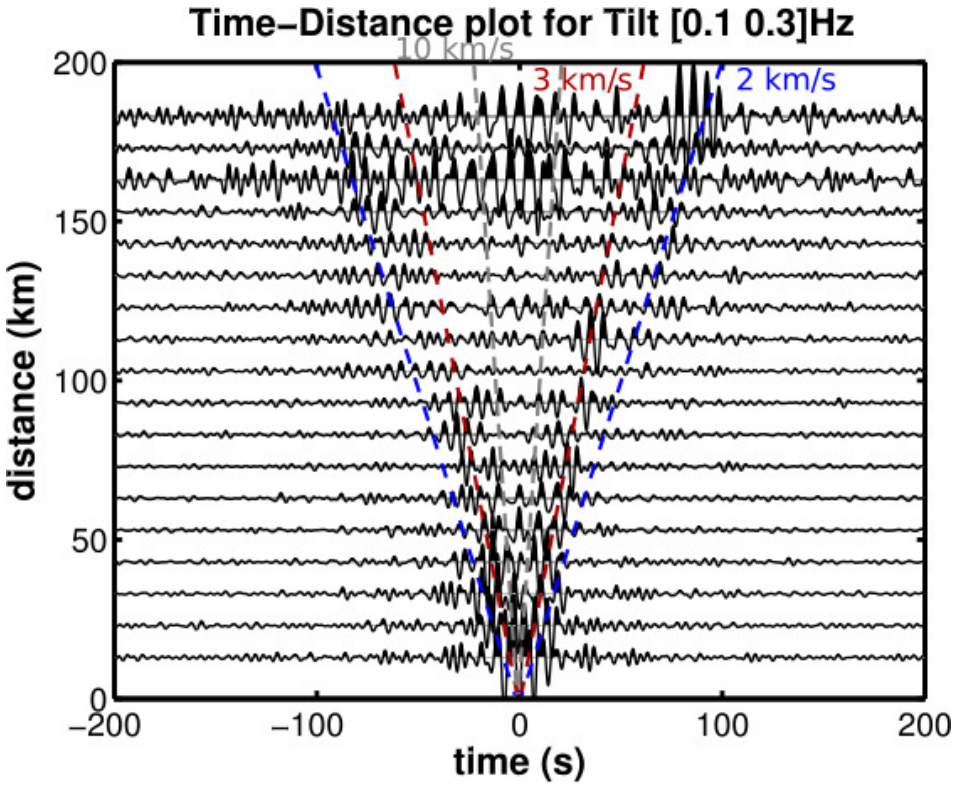

FIG. 8.4 – Time-Distance diagram for the R-R component of cross-correlations at [0.1 0.3]Hz. The cross-correlations are binned according to interstation distance into 10 km bins. The red dashed lines indicate a 3 km/s wave speed, the blue ones 2 km/s. The grey dashed lines correspond to a 10 km/s wave speed.

on each side of the correlation. The traveltime will appear shorter on one side, and longer on the other : the whole correlation function is shifted.

We are interested in the first type of traveltime change, and would like to eliminate any effects from the two other phenomena. The effect of a source distribution change can be reduced by using the coda, as seen in chapter 7 and shown by Weaver et al. [2009a] and Froment et al. [2010]. The possibility of correcting instrumental clock errors using cross-correlation functions has been shown in past studies [Stehly et al., 2007; Sens-Schönfelder, 2008; Brenguier et al., 2008a].

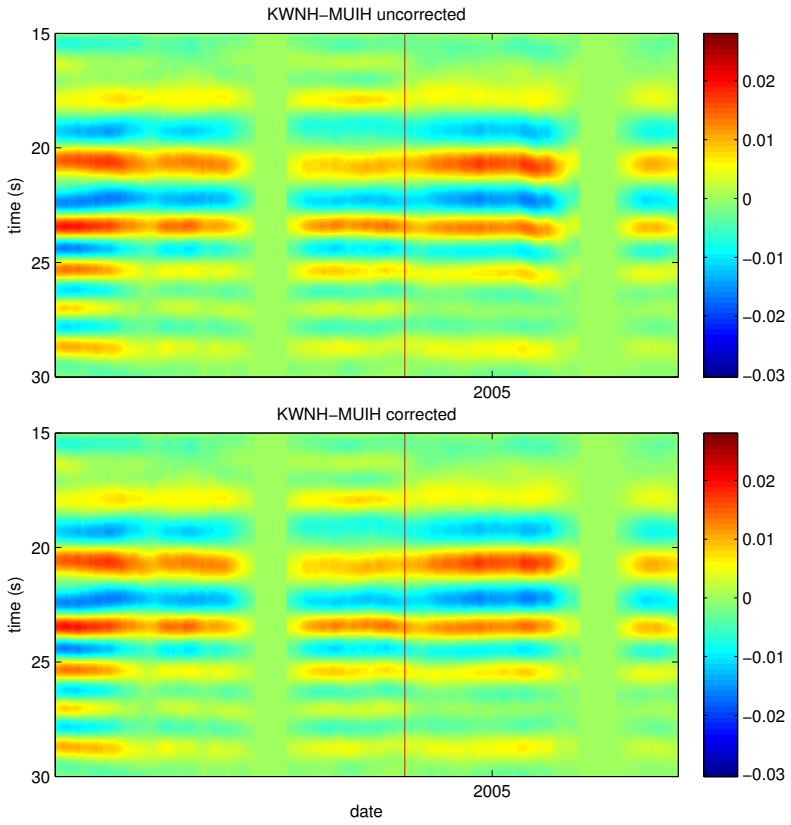

FIG. 8.5 – Top : correlations functions for station pair KWNH-MUIH, before correction of clock error. Bottom : after correction. The red line indicates the date of the Chuetsu earthquake.

When we look at a closeup of the direct waves on the correlation function of one couple (figure 8.5, top), we can see that the phase of the correlation function starts drifting after 2005. In this case, the whole correlation function had been shifted to one side. The direct waves on the negative side of the correlation function present a smaller travel time, while those on the positive side present a larger travel time.

The bottom half of figure 8.5 shows the same correlation functions, after correction for the clock error.

8.3.2 Velocity Variation Measurement

The velocity changes are measured using the stretching method [Lobkis and Weaver, 2003; Sens-Schönfelder and Wegler, 2006]. In this method, the coda of correlation signal $h\,[t]$ is compared to the reference signal $h_0\,[t]$. As said before, reference used is the average of all daily correlation functions. The signal $h\,[t]$ is one of the 30-day stacks mentioned above. This correlation signal is then interpolated at times $t(1-\varepsilon)$ with various stretching factors ε. The actual relative velocity change is the stretching factor $\varepsilon_0 = dV/V$ that maximizes the cross-correlation coefficient :

$$CC(\varepsilon) = \frac{\int_{t_1}^{t_2} h\,[t(1-\varepsilon)]\, h_0[t]dt}{\sqrt{\int_{t_1}^{t_2} h^2\,[t(1-\varepsilon)]\,dt.\int_{t_1}^{t_2} h_0^2[t]dt}}, \tag{8.1}$$

where t_1 and t_2 the start and end time of the coda used, respectively. This operation is repeated for each stack and each station couple.

This technique works correctly for a linear behavior of δt versus t and therefore assumes a homogeneous relative velocity change. In complex media this might not be entirely accurate. Nevertheless, because the whole coda is processed at once, this technique provides a stable, and thus more precise, estimation of dV/V.

Another advantage of the technique is that the remnant coherence $CC(\varepsilon)$ provides additional information. It indicates if noise sources are stable or changing over the period of observation of interest : $CC \sim 1$ means absolutely stable sources, $CC << 1$ means that sources locations are changing. Using CC, we can thus evaluate the error on the ε estimation.

When measuring the dV/V, we want to exclude the direct waves in the correlation signal. The phase of these waves can be influenced by the source distribution [Weaver et al., 2009a; Froment et al., 2010], which could lead to errors in the dV/V measurement. Thus, the dV/V measurement is preferably done using the coda part of the signal. The timewindow used in equation 8.1 (t_1 to t_2) is selected accordingly. To avoid the use of the direct waves, the start of the timewindow is selected based on the interstation distance d. A maximum wave propagation speed is selected, which is supposed slower than the surface waves. Thus, the start of the timewindow is set at $\pm V_{\max} d$. Figure 8.4 shows that typically, the surface waves propagate faster than $V_{\max} = 1$ km/s.

The end of the timewindow used will depend on the lapse time at which the am-

plitude of the coda becomes too small compared to the noise level. This can be evaluated by looking at the evolution of the coherence along the signal, explained in section 8.3.3.

The results of the dV/V measurements are presented in section 8.4.

8.3.3 Coda Coherence

To get a good, stable result from stretching, we need to compare reasonably coherent parts of the signals with each other. In order to determine the end of the timewindow used in the stretching technique, the gradual decorrelation of the signal is examined. For a selection of station pairs, we calculate the similarity between one stack and the reference function. A 30-second sliding window is translated along the signal, and for each step the coherence is determined. As the lapse time increases, the coda will start to disappear in the noise, which is expressed as a gradual decrease in coherence.

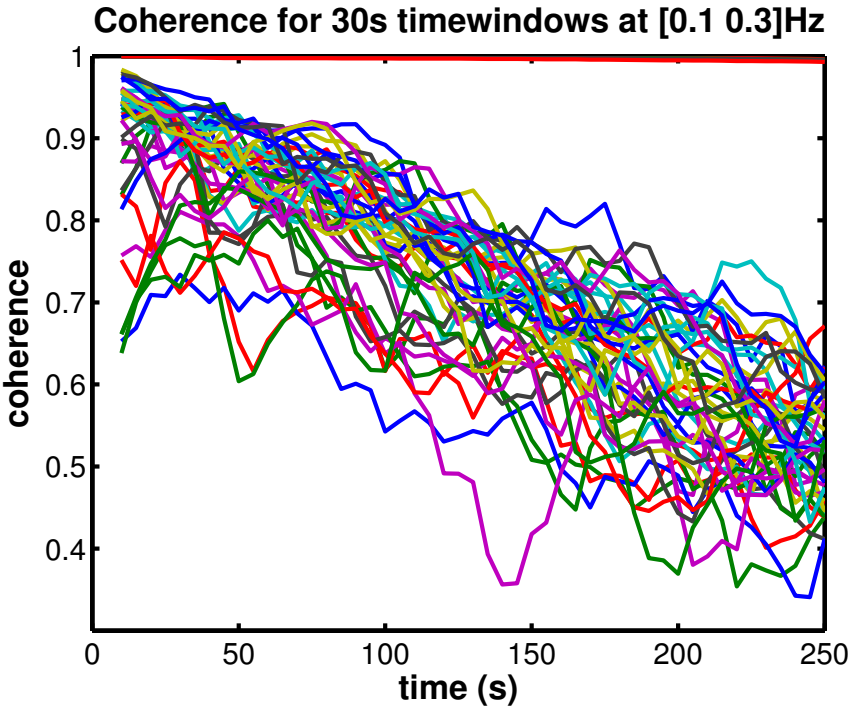

FIG. 8.6 – Coherence versus lapse-time for a 30 second sliding window in the coda. Results shown for 98 station pairs, for correlation functions are bandpassed at [0.1 0.3]Hz.

Examples of this degradation in coherence are shown in figure 8.6 for several station pairs. Here we see that for lapse times larger than 150 seconds, the coherence falls

below 0.7 in most cases. Based on this observation, we decide to use 150 seconds as a cutoff of the stretching timewindow.

So finally, the timewindow used spans from $\pm V_{\max} d$ to $\pm$ 150 seconds. The disadvantage of the fixed end time is that the usable part of the signal decreases as two stations from a pair lie further apart. Regrettably, for more distant station pairs, the SNR is generally lower. Using a short timewindow in cases with high SNR is less than ideal with the stretching technique. A possible solution would be to let the end of the timewindow depend on the interstation distance as well as the beginning. However, we would then risk using the noisy tail-end signal to measure the dV/V. This trade-off must be taken into account when selecting the stretching timewindow.

8.3.4 Quality Control

When inspecting the data, it becomes clear that the quality of the correlation functions fluctuates quite significantly. In figure 8.7 an example of a time section of the correlation functions is shown, spanning from January 2004 to December 2005. The black line on the right represents the overall coherence of each 30-day stack with respect to the reference function. Almost all station pairs present periods of missing data, and most exhibit temporary 'dips' in the coherence of the correlations.

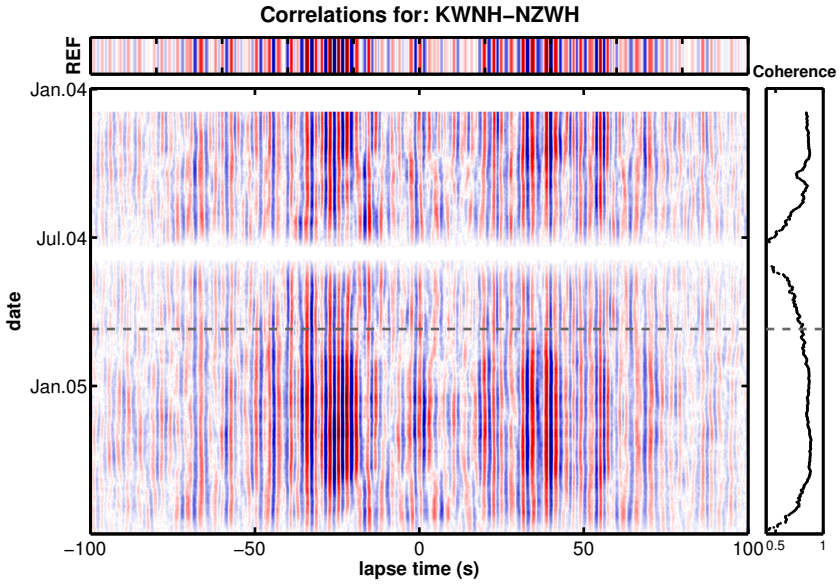

FIG. 8.7 – Time section of the correlation functions for station pair KWNH-NZWH from January 2004 to July 2005. The grey dashed line indicates the date of the Chuetsu event. On the right : the coherence of each 30-day stack with respect to the reference stack (represented on top).

In order to get the best results from the dV/V measurements, we must determine which 30-day stacks are reliable enough to use. As we have seen in section 8.3.2, the correlation coefficient CC can be used as a measure for noise source stability. In order to avoid negative effects from any noise source changes, it would be best to use the time periods for which a station pair exhibits a constant coherence.

As a first criterion, only the stacks with a coherence $\geq$ 0.7 are used. This conveniently excludes the time periods where no data exists. Next, we keep the station pairs where at least 50 % of the 30-day stacks remain after this first selection. Finally, a visual inspection eliminates the stations pairs where heavy coherence fluctuations remain.

8.4 Velocity Variations

Initially, the dV/V is measured for the 13 station pairs directly surrounding the event (see map in figure 8.8), which have acceptable quality cross-correlation functions. The correlation functions are bandpassed between [0.1 0.3]Hz, and stacked with a 30-day sliding window. The reference function is the stack for the whole 18-month period. The dV/V measurement is performed on the coda from $\pm$ 30 to $\pm$ 120 seconds. The results of this analysis are shown in figure 8.9.

From this figure, we see that the velocity is quite constant leading up to the event. We also clearly see a drop in seismic speed coinciding with the event. Note that the amplitude of the drop is of the order of 0.1%. Wegler et al. [2009] have studied the velocity change of this same event using velocimeter data bandpassed for [0.1 0.5] Hz. They find a relative velocity drop coinciding with the event, with amplitudes ranging from 0.1% to 0.25%, depending on the station pair. These values are similar to the one observed in Parkfield (chapter 4).

It is important to note the stability of the coherence at the time of the event. It indicates that the change of velocity is likely not related to a change in noise sources, but rather a physical velocity change in the medium (see chapter 6).

After the event, the velocity does not return to pre-seismic levels immediately. Rather, it drops by $\sim$ 0.05% within two months, only to stabilize approximately 0.07% above the pre-seismic mean velocity level. A tentative interpretation would be that part of the damage to the fault zone is permanent.

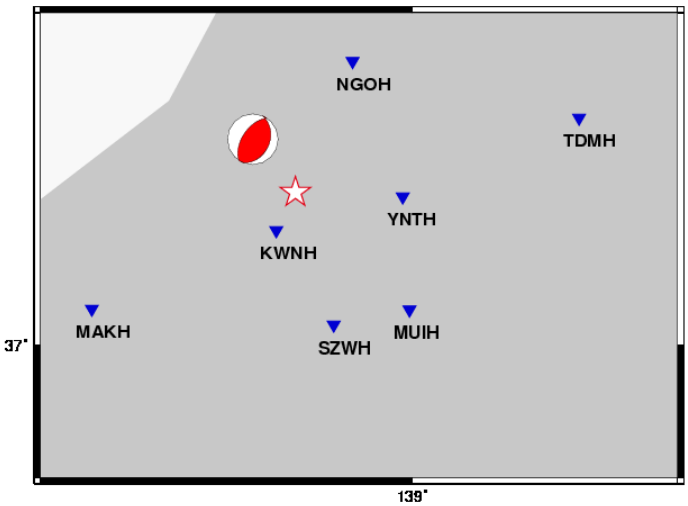

FIG. 8.8 – Zoom on the sub-array used for the results in figure 8.9.

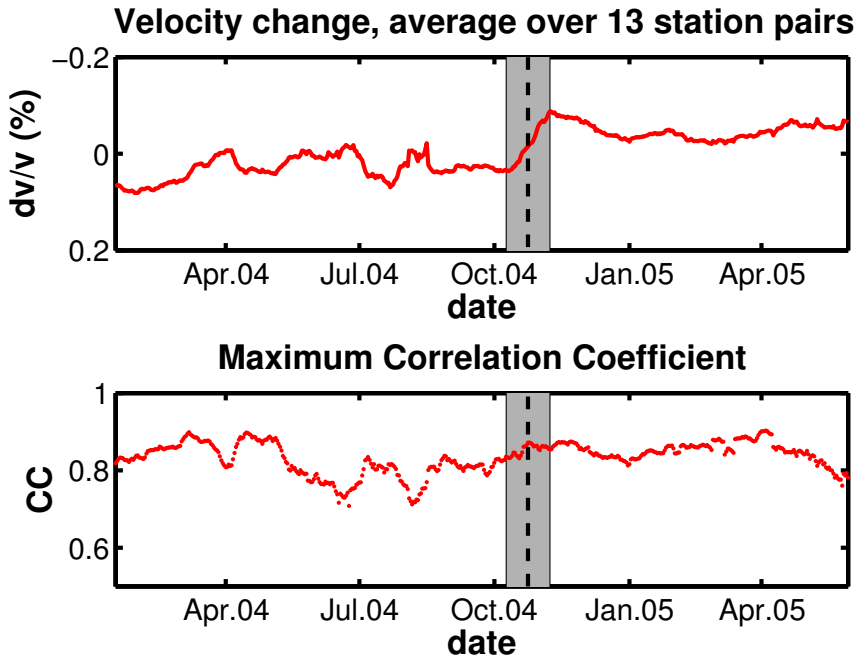

FIG. 8.9 – Top : dV/V measurements averaged over 13 station pairs. Bottom : corresponding maximum correlation coefficient (CC). Correlation functions are band-passed for [0.1 0.3]Hz. The black dashed line indicates the date of the $M_w = 6.9$ Chuetsu event. The grey area indicates the extent of the 30-day stack.

8.4.1 Distance dependence

dV/V measurements on the 2008 $M_w = 7.9$ Wenchuan, China earthquake, show a coseismic velocity drop at frequencies around [0.3 1.0] Hz [Campillo et al., 2009]. However, when the dV/V is measured at lower frequencies ([0.03 0.1]Hz), the effect is delayed : the velocity drop sets in at a later time. Since lower frequency seismic waves are typically sensitive to the deeper crust, this observation could be interpreted as a velocity change starting at the hypocenter and slowly spreading down. If this is the case, we can hypothesise that the velocity change also spreads laterally. In the following, we investigate the dependence of the velocity change to the distance to the epicenter.

We repeat the dV/V the measurements from the previous section for all reasonable quality stacks identified using the criteria outlined in section 8.3.4. The 30-day sliding stack of correlations is again compared to a reference trace, which is simply the average over the 18-month period. The coda timewindow used spans from $\pm V_{\max} d$ to $\pm$ 150 seconds, as detailed in section 8.3.3. The average over all available station pairs is shown in figure 8.10. We see the same overall behavior as in figure 8.9, with a coseismic velocity drop of $\sim 0.1\%$. So the average works when including stations further away. The next step is to sort the dV/V measurements according to epicentral distance.

Since coda waves sample an extended volume, defining a physically relevant 'distance' measure is not straightforward, without resorting to the calculation of a sensitivity kernel. The multiple scattering 'halo', *i.e.*, the volume sampled by the wavefield, grows as $\sqrt{Dt}$, where $D = \frac{vl^\star}{2}$ the diffusion constant. Here, v is the wave speed and $l^\star$ is the mean free path. In order to use this model, we would have to determine $l^\star$ for the Niigata region of Japan, at the frequencies used in our study.

In a first approximation, based on single scattering, we can consider the minimum distance a wave needs to travel to pass through the epicentral region. For each station couple, we calculate the distance from station A to the epicenter, and back to station B :

$$d_{\text{epi}} = d_{AS} + d_{BS},$$

where d_{AS} and d_{BS} the distance from the epicenter S to stations A and B, respectively.

The approximately 50 station pairs which satisfy the quality criteria (from section 8.3.4) are binned into three distance bins, while trying to distribute them as evenly as possible. The dV/V measurements are averaged for each distance set, with the results in figures 8.11, 8.12 and 8.13. The most striking result is that, at least up to $d_{\text{epi}} \sim 200$ km, the order of velocity drop measured (approximately 0.1%) is similar to the near-epicenter result from figure 8.9. The question arises whether the

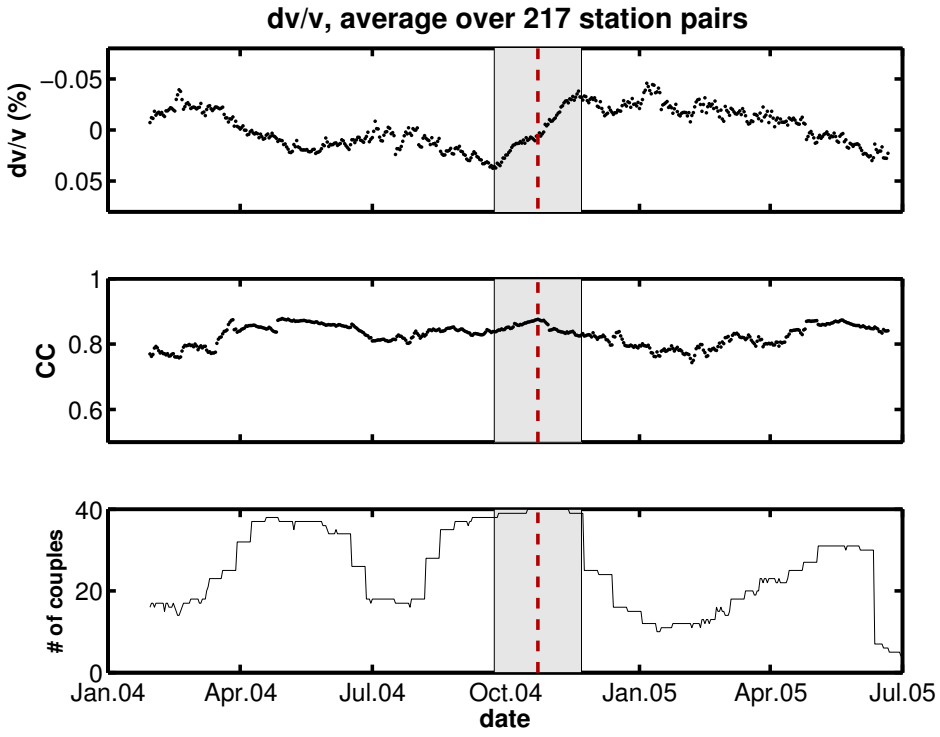

FIG. 8.10 – Top : dV/V measurements, averaged over 217 station pairs. Center : The corresponding maximum correlation coefficient (CC) values. Bottom : the number of station pairs used in the average (*i.e.*, which satisfy the quality criteria). The dashed red line indicates the date of the Chuetsu earthquake, the grey area shows the extent of the 30-day sliding window used.

effect we measure is localized around the epicenter or more widespread.

However, in the dV/V measurements, we use the coda up to 150 seconds. Taking into account the average interstation distance of $\sim$ 50 km, this means the average correlation function contains physical information from a wave which has propagated for 120 seconds. Assuming a seismic wave speed of $\sim$ 3 km/s, we can estimate that the part of the correlation function we use can be sensitive to velocity changes lying on trajectories of up to 360 km. The longest station – epicenter – station paths available on the array are of the order of 200 km. Therefore it is possible that all the correlation functions we use are sensitive to a velocity change in the epicentral area, and we cannot say if the change we observe in figures 8.11-8.13 are located near the epicenter or further away.

One way to ensure we are measuring mostly local velocity changes is to reduce the maximum length of the signal used. However, the use of shorter timewindow complicates the successful application of the stretching method. Tests to measure a more local dV/V by using shorter coda timewindows are currently in progress.

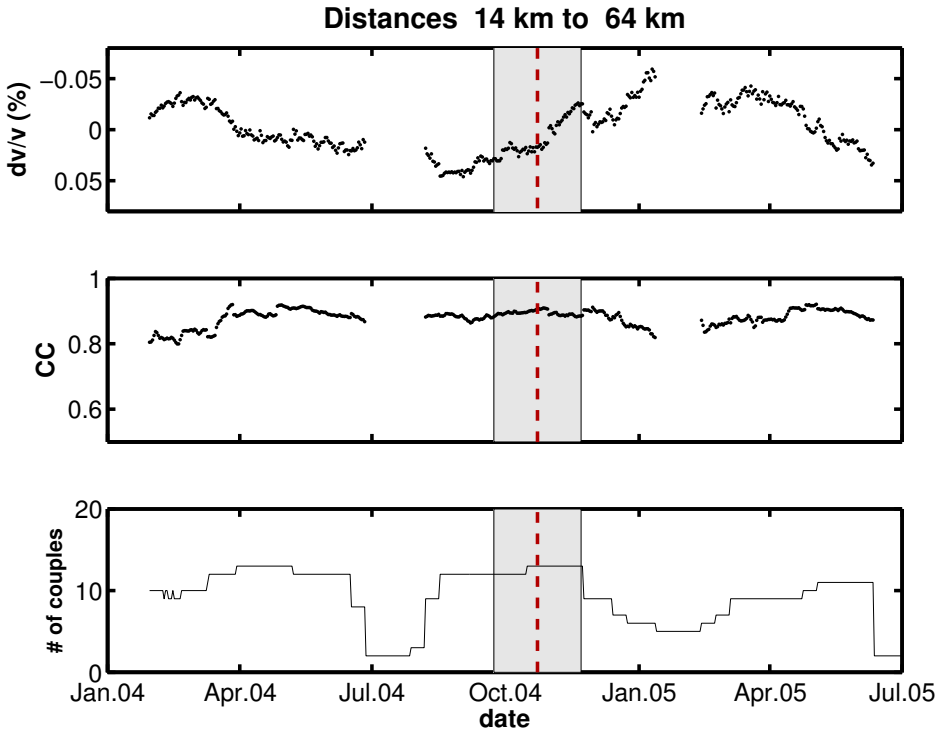

FIG. 8.11 – Top : dV/V measurements, averaged over the station pairs closest to the epicenter. Center : The corresponding maximum correlation coefficient (CC) values. Bottom : the number of station pairs used in the average (*i.e.*, which satisfy the quality criteria). The dashed red line indicates the date of the Chuetsu earthquake, the grey area shows the extent of the 30-day sliding window used.

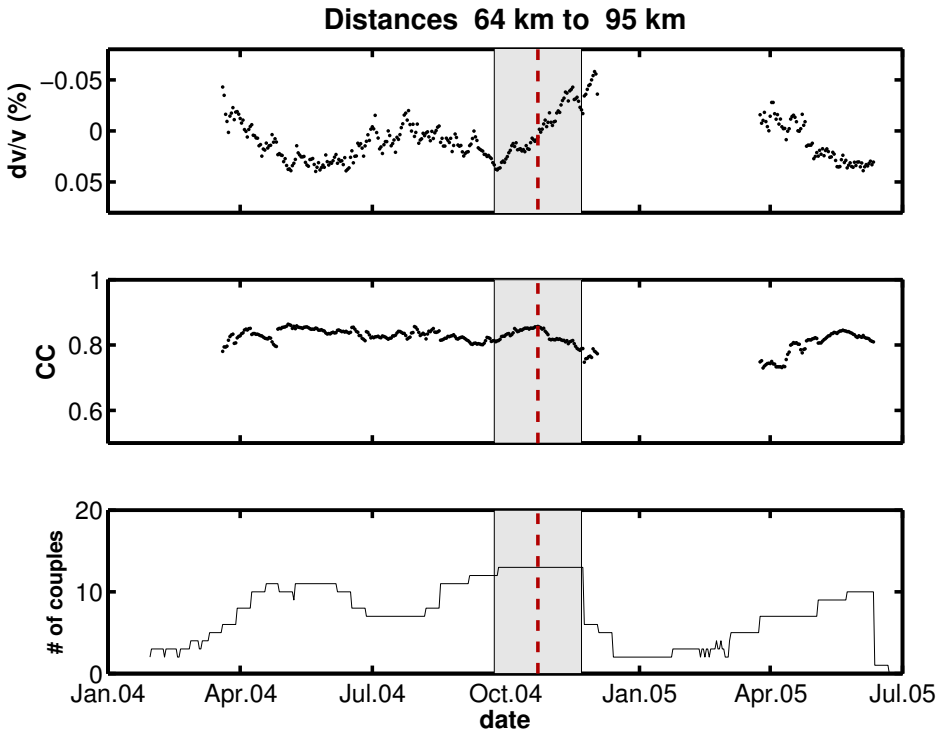

FIG. 8.12 – As figure 8.11, but for a subset of stations at intermediary distance from the epicenter.

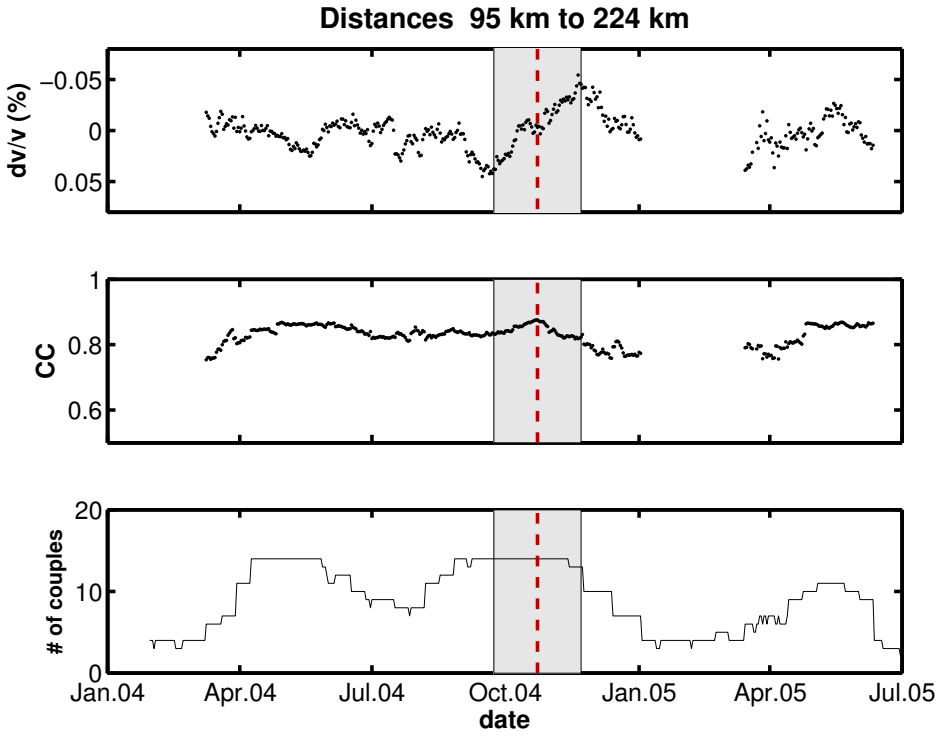

FIG. 8.13 – As figure 8.11, but for a subset of stations furthest from the epicenter.

8.5 Discussion & Conclusion

We have observed a relative velocity drop of the order of 0.1%, coinciding with the $M_w = 6.6$ Chuetsu earthquake in 2004. We have studied the distance dependence of this velocity change using a simple single-scattering model for wave propagation. Some improvements are still necessary however.

Coda waves sample an extended 3D volume. This makes it difficult to evaluate the distance dependence of the relative velocity changes we measure. The ideal would be to know the sensitivity kernel of multiply scattered coda waves. Alternately, we could determine the extent of the multiple scattering halo to get an indication of the volume sampled by the wavefield used.

The use of smaller subsets of station pairs, in the effort to regionalize the velocity change, will decrease the precision on dV/V measurements. To compensate for this, it is possible to include the correlation functions for the other components into the analysis, thereby improving the SNR.

Chapitre 9

Conclusion

La présente thèse explore les méthodes et les applications de l'utilisation des corrélations de bruit ambiant pour suivre les variations de vitesse dans les zones de failles actives.

La première étape consistait à appliquer les méthodes de suivi temporel aux données provenant d'une zone de faille active à Parkfield, Californie, oùnous avons réussi à détecter deux chutes de vitesse. Ces dernières coïncident avec des évènements sismiques régionaux, le plus important concernant un évènement proche des stations (séisme de Parkfield), l'autre à environ 60 km (séisme de San Simeon). Les deux chutes de vitesse sont suivies d'une récupération postsismique progressive. Les processus physiques provoquant ce comportement ne sont pas encore compris. Les causes possibles évoquées sont les dommages en surface ou dans la zone de faille, la variation de stress ou l'écoulement fluide.

Pour mieux comprendre la fiabilité des mesures de dV/V, nous avons effectué une expérience en laboratoire. Nous avons produit un changement de vitesse dans un environnement de laboratoire contrôlé, pour tester les limites des méthodes de suivi temporel. Cette variation de vitesse est mesurée d'une part par une méthode de "suivi temporel actif" bien établie, d'autre part par la reconstruction imparfaite de la fonction de Green à partir d'intercorrélations. Nous avons montré que mesurer la variation de vitesse par l'une ou l'autre méthode donnait les mÃªmes valeurs. Ce résultat intéressant montre que la reconstruction exacte de la fonction de Green n'est pas nécessaire pour le suivi temporel, ce qui ouvre la voie à de nombreuses possibilités d'applications en sismologie.

Poursuivant nos efforts pour évaluer la fiabilité de nos mesures, nous avons développé une expression pour les fluctuations attendues dans les quantités mesurées dV/V. Cette expression nous fournit un moyen d'estimer les erreurs de mesure, et par conséquent d'identifier des variations de vitesse significatives.

Grâce à cette connaissance, nous avons revu la série de données de Parkfield dans le but d'améliorer les mesures. Nous avons utilisé les résultats d'expériences en laboratoire pour affirmer qu'il suffisait d'une moyenne temporelle réduite pour obtenir une fonction de corrélation appropriée au suivi temporel. Après avoir appliqué un filtre

adaptatif nous avons pu améliorer la résolution temporelle à 1 journée. De plus, nous montrons que la chute de vitesse observée est cosismique avec le séisme de Parkfield. En outre, en suivant le champ de bruit à l'aide de techniquesÂ de formation de voie, nous avons établi que les fluctuations restantes de dV/V ne sont pas directement corrélées à la distribution de sources de bruit.

Enfin, nous avons appliqué les méthodes développées à une série de données différentes, à savoir provenant d'un ensemble de stations au Japon. La taille du réseau étant beaucoup plus vaste que celui utilisée pour l'étude de Parkfield, nous avons utilisé ces données pour étudier la dépendance entre la distance et les variations de vitesse mesurées. Ce travail est toujours en cours.

Quelques suggestions concernant la poursuite de ces recherches figurent dans le chapitre suivant.

Chapitre 10

Perspectives

10.1 Parkfield : 9-component Green's Tensor

Since the work in chapter 7, additional correlations were calculated to obtain the full 9-component Green's tensor. Using all these components to measure the dV/V has proven to increase the precision of the measurements.

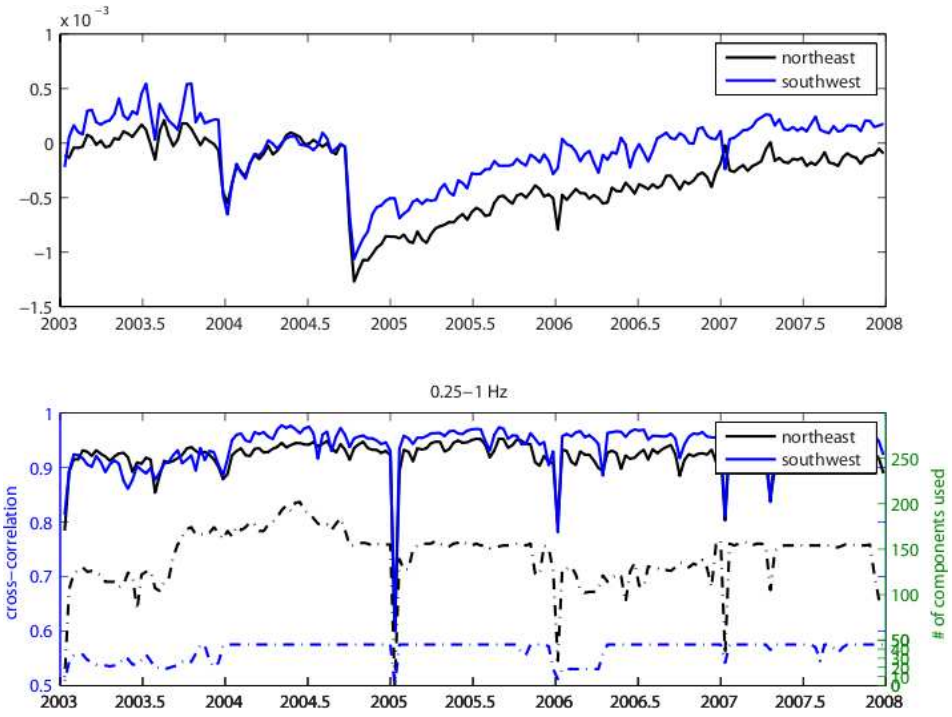

Fig. 10.1 – Relative velocity change measured near Parkfield, using the whole 9-component Green's tensor. Correlation functions are bandpassed at [0.25 1]Hz, and averaged using a 20-day sliding window. The reference function used is the average of 3 months of noise around July, 2004. (Courtesy Ozgun Koncao.)

With these new measurements, it is possible to distinguish the dV/V on either side of the fault independently (figure 10.1). Why do the two sides exhibit a different

postseismic behavior ? Additionally, there seems to be an initial steep increase in velocity right after Parkfield, followed a more moderate slope after the start of 2005.

The increase in precision gained by using the full 9-component Green's tensor can lead to greater understanding of the physical processes involved.

10.2 Localization

Finally, the logical step after the measurement of global velocity changes is to locate the changes. Larose et al. [2010] have developed a technique which allows to locate small perturbations which appear in a multiple scattering environment. This technique is based on the direct dependence in space and time of the coda decorrelation resulting from the apparition of a supplementary scatterer. The technique uses the decorrelation of waveforms after a perturbation is introduced. It returns a probability function, χ^2, of where the perturbation is located.

The technique was developed with the monitoring of concrete structures (bridges, buildings, ...) in mind. We tried applying the technique to the data from Parkfield on a whim. The correlation coefficient for 30 days before and after the Parkfield event were compared, to find the decorrelation. The result is shown in figure 10.2. Here, the white area indicates a high χ^2 value, with the maximum located at the red square. The location of the event, right next to the maximum, is indicated by the red star. The extent of the white area (high probability of perturbation) suggests that most of the structural change is located around the epicenter.

This suggestive result incites further study towards the application of localization techniques to seismological applications.

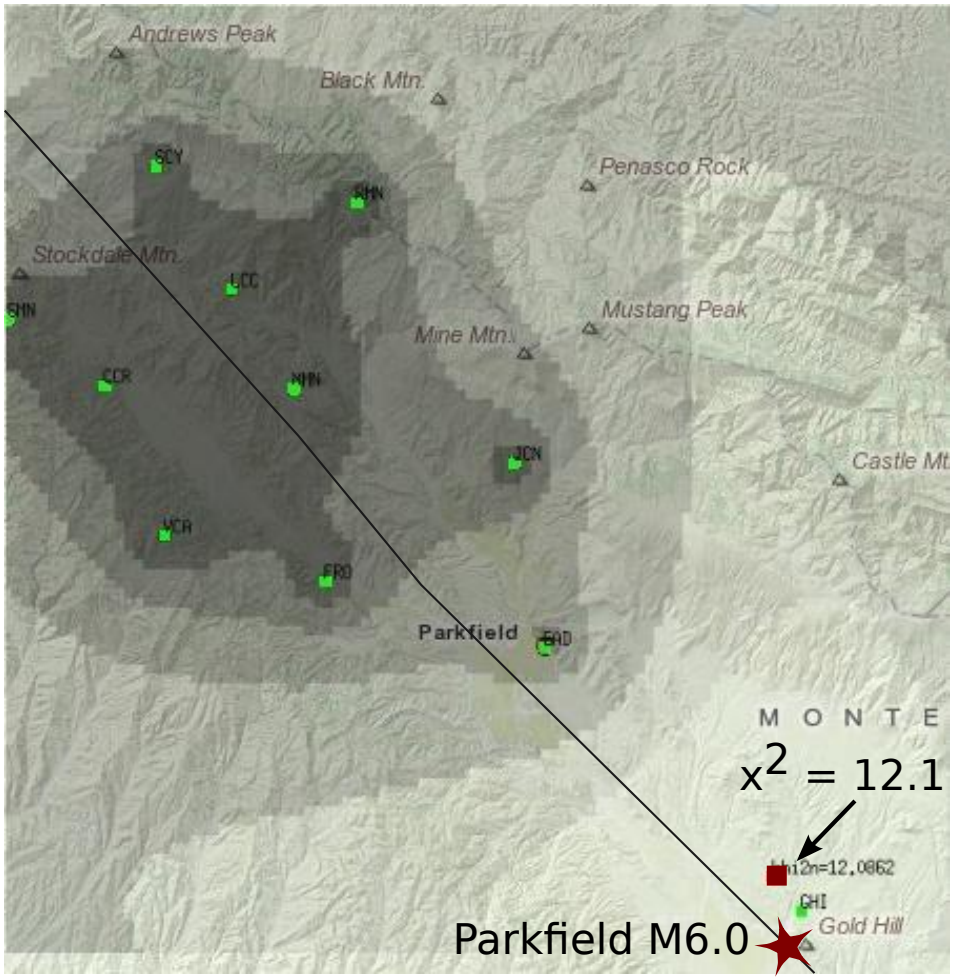

FIG. 10.2 – Dark areas represent low χ^2 values, light areas high ones. The red square indicates the maximum normalized $\chi^2 = 12.1$. The green squares show the location of the stations used, the red star is epicenter of the Parkfield event.

Annexe A

Appendix

A.1 On the precision of noise-correlation interferometry

Authors :
R. L. Weaver, C. Hadziioannou, E. Larose, and M. Campillo

Abstract

Long duration noisy-looking waveforms such as those obtained in randomly multiply scattering and reverberant media are complex ; they resist direct interpretation. Nevertheless, such waveforms are sensitive to small changes in the source of the waves or in the medium in which they propagate. Monitoring such waveforms, whether obtained directly or obtained indirectly by noise correlation, is emerging as a technique for detecting changes in media. Interpretation of changes is in principle problematic ; it is not always clear whether a change is due to sources or to the medium. Of particular interest is the detection of small changes in propagation speeds. An expression is derived here for the apparent, but illusory, waveform dilation due to a change of source. The expression permits changes in waveforms due to changes in wavespeed to be distinguished with high precision from changes due to other reasons. The theory is successfully compared with analysis of a laboratory ultrasonic data set and a seismic data set from Parkfield California.

A.1.1 Introduction

The technique proposed in the 1980's [Poupinet et al., 1984] and later called 'Coda wave interferometry' [Snieder et al., 2002] compares coda waveforms from multiply scattered waves obtained under different circumstances or on different dates and detects changes in a medium. A multiply scattered wave can resist detailed interpretation, but for purposes of monitoring one may not need to interpret the waveform ; it suffices to notice changes. Coda wave interferometry was first suggested for seismic waves but has also been applied in laboratory ultrasonics [Lobkis and Weaver,

2003; Gorin et al., 2006; Lobkis and Weaver, 2008; De Rosny and Roux, 2001; Lu and Michaels, 2005]. In many such cases the change is due to a uniform change of temperature, and thus a uniform change in wave velocity. To detect such, Lobkis and Weaver [2003] constructed a dilation correlation coefficient between waveforms ϕ_1 and ϕ_2.

$$X(\varepsilon) = \int \frac{\phi_1(t)\phi_2(t(1+\varepsilon))dt}{\sqrt{\int \phi_1^2(t)dt \int \phi_2^2(t(1+\varepsilon))dt}} \tag{A.1}$$

X takes on a value of unity at $\varepsilon = 0$ if the two waveforms are identical, and a value of unity at some characteristic value of ε if the two waveforms differ only by some temporal dilation. It takes a value less than unity if the waveforms differ by more than dilation. The estimated degree of dilation between two waveforms is taken to be the value of ε at which X is maximum. The degree to which X at its maximum is less than unity may be interpreted as a measure of the irreconcilable difference, or distortion, between the waveforms.

An alternative formulation is Poupinet's doublet method ([Poupinet et al., 1984]), which breaks ϕ_1 and ϕ_2 into a series of short time windows at several distinct times t, and determines the apparent shift δt between them by examining conventional cross correlations. δt as a function of t, and in particular its slope $\delta t/t$ reveals a change in the medium. Poupinet developed the doublet method in which seismic signals from repeated seismic events could be compared to infer changes in the earth [Poupinet et al., 1984]. Song and Richards [1996] and Zhang et al. [2005] used this to show that certain earth crossing rays were shifted and distorted compared to versions some years earlier, indicating a relative rotation between the earth and its core.

The extensive literature in recent years on correlations of diffuse acoustic noise has reported theory and measurements in support of the notion that such correlations are essentially equal to the acoustic response that one would have at one receiver were there a source at the other [Lobkis and Weaver, 2001; Weaver and Lobkis, 2004; Derode et al., 2003b; Snieder, 2004; Roux et al., 2005; Gouédard et al., 2008]. More technically, what is recovered is the Green's function as filtered into the frequency band of the noise and symmetrized in time. Sometimes it is coda that is correlated, a short duration random looking signal that follows the main arrivals from a strong seismic source and is due to single or multiple scattering. More commonly the diffuse noise is due to ambient seismic waves from continuously acting sources such as human activity or ocean storms. Much recent literature reports constructions of the earth's seismic response between two seismograph stations, without the use of controlled sources, and without waiting for a seismic event. Tomographic maps of seismic velocity with unprecedented resolution have been obtained [Shapiro et al., 2005; Sabra et al., 2005a]. The technique has even been applied on the moon [Larose

et al., 2005a]. Very commonly, the noise which is correlated is incompletely equipartitioned, such that the resulting correlation waveforms do not precisely correspond to the Green's function. It also may be that one has not averaged enough raw data ; the correlation may not have yet converged. Theoretical and applied work is ongoing in attempts to understand and correct for systematic errors due to these effects, *e.g.*, , [Weaver et al., 2009a; Froment et al., 2010].

These two approaches have been combined into what may be termed 'noise-correlation interferometry', [Sabra et al., 2006; Sens-Schönfelder and Wegler, 2006; Brenguier et al., 2008b,a] in which correlations of seismic noise taken in different circumstances are compared. The correlations may have been obtained from different samples of ambient noise, perhaps on different dates, or from the codas of different events. The correlations are of course never identical ; they are often very different. One reason for a difference is that the source of the noise may be different (yet if the correlation has converged to the local Green's function, a change of noise source ought have little effect). Continuous seismic sources can move and strengthen and weaken as weather changes at sea. It may also be that the correlation has not fully converged (*i.e.*, , insufficient averaging has been done). A third possibility is that the local mechanical or acoustic environment may have evolved, in particular, the local wave speed(s) may have changed. It is this possibility that is of particular interest, as changes in seismic velocities are associated with relaxations after major seismic events [Brenguier et al., 2008a]. In some cases changes in seismic velocity can be used to predict volcanic eruptions [Brenguier et al., 2008b]. Thus it is of great interest to be able to discern whether a change is due to a change in local environment or to a change in the character of the noise.The latter possibility is of some interest ; the former is of great interest.

Our purpose here is to evaluate the precision with which wave speed changes can be evaluated. To do this we consider the case in which the two waveforms $\phi_1(t)$ and $\phi_2(t)$ differ only by noise so that the actual relative dilation, sans noise, is zero. We then ask for the apparent (non-zero in general) value of ε at which the corresponding X in equation (A.1) achieves its maximum. The next section calculates the root mean square of this apparent, and erroneous, relative dilation. The subsequent sections compare this prediction with experiment.

A.1.2 Dilation Correlation Coefficient

Here we examine, theoretically, the apparent waveform-dilation between two nominally identical signals, for which one ought infer a relative dilation ε of zero, but for which noise corrupts the inference. Key to the following analysis is an understanding that the signals being discussed are like coda, in that they are statistically stationary with durations long compared to an inverse bandwidth. We take the two waveforms

to have an identical part $\psi(t)$, and to differ by noise $2\mu\chi(t)$. In the limit $\mu \to 0$, the waveforms become identical and have no relative dilation. If $\mu \neq 0$, there will be an apparent, but actually meaningless, temporal dilation between them. We wish to estimate this erroneous apparent relative dilation, and to identify any signatures that could be used to alert to the possibility of error. The common part ψ of the signals need not be the local Green's functions.

We split the difference between these two waveforms ϕ_1 and ϕ_2. and define two signals ψ and χ ;

$$\phi_{1,2} = \psi(t) \pm \mu\chi(t) \tag{A.2}$$

The waveform dilation-correlation coefficient (A.1) between them is

$$\begin{aligned} X(\varepsilon,\mu) &= \frac{\int \phi_1(t(1+\varepsilon/2))\ \phi_2(t(1-\varepsilon/2))\ dt}{\sqrt{\int \phi_1^2(t(1+\varepsilon/2))\ dt\ \int \phi_2^2(t(1-\varepsilon/2))\ dt}} \\ &= \sqrt{1-\varepsilon^2/4}\frac{\int \left[\psi(t(1+\varepsilon/2)) + \mu\chi(t(1+\varepsilon/2))\right]\ \left[\psi(t(1-\varepsilon/2)) - \mu\chi(t(1-\varepsilon/2))\right]\ dt}{\sqrt{\left[\int \psi^2 + \mu^2\chi^2)\ dt\right]^2 - 4\mu^2\left[\int \chi\psi\ dt\right]^2}} \\ &= \sqrt{1-\varepsilon^2/4}\ \frac{N(\varepsilon,\mu)}{D(\mu)} \end{aligned} \tag{A.3}$$

with N and D implicitly defined by equation (A.3). The integrations are typically taken over a finite time-window with tapered edges.

The value of ε at which X achieves its maximum is the practitioner's estimate of the dilation between the waveforms ϕ_1 and ϕ_2. It occurs at ε such that $\partial X/\partial\varepsilon = 0$, or,

$$0 = \sqrt{1-\varepsilon^2/4}\ D(\mu)\frac{\partial X(\varepsilon,\mu)}{\partial\varepsilon} = \frac{-\varepsilon\ N(\varepsilon,\mu)}{4+(1-\varepsilon^2/4)}\frac{\partial N(\varepsilon,\mu)}{\partial\varepsilon} \tag{A.4}$$

If $t\omega\varepsilon << 1$ for all times t and frequencies of interest, it suffices to expand N through only the 2nd power of ε :

$$\begin{aligned} N(\varepsilon,\mu) = \int &\left[\psi(t) + \frac{t\varepsilon}{2}\dot{\psi}(t) + \frac{t^2\varepsilon^2}{8}\ddot{\psi}(t) + \mu\chi(t) + \frac{\mu\varepsilon t}{2}\dot{\chi}(t) + \frac{\mu t^2\varepsilon^2}{8}\ddot{\chi}(t)\right] \\ &\times \left[\psi(t) - \frac{t\varepsilon}{2}\dot{\psi}(t) + \frac{t^2\varepsilon^2}{8}\ddot{\psi}(t) - \mu\chi(t) + \frac{\mu\varepsilon t}{2}\dot{\chi}(t) - \frac{\mu t^2\varepsilon^2}{8}\ddot{\chi}(t)\right]\ dt \end{aligned} \tag{A.5}$$

On collecting terms in $N(\varepsilon,\mu)$ that are linear and quadratic in ε obtains

$$\begin{aligned} N(\varepsilon,\mu) \;\sim\; & \int \left[\psi(t)^2-\mu^2\chi(t)^2\right] dt + \int \left[\frac{t\varepsilon}{2}\dot{\psi}(t)+\frac{\mu\varepsilon t}{2}\dot{\chi}(t)\right]\,\left[\psi(t)-\mu\chi(t)\right] dt \\ + & \int \left[-\frac{t\varepsilon}{2}\dot{\psi}(t)+\frac{\mu\varepsilon t}{2}\dot{\chi}(t)\right]\,\left[\psi(t)+\mu\chi(t)\right] dt \\ + & \int \left[\frac{t^2\varepsilon^2}{8}\ddot{\psi}(t)+\frac{t^2\mu\varepsilon^2}{8}\ddot{\chi}(t)\right]\,\left[\psi(t)-\mu\chi(t)\right] dt \\ + & \int \left[\frac{t^2\varepsilon^2}{8}\ddot{\psi}(t)-\frac{t^2\mu\varepsilon^2}{8}\ddot{\chi}(t)\right]\,\left[\psi(t)+\mu\chi(t)\right] dt \\ + & \int \left[\frac{t\varepsilon}{2}\dot{\psi}(t)+\frac{\mu\varepsilon t}{2}\dot{\chi}(t)\right]\left[-\frac{t\varepsilon}{2}\dot{\psi}(t)+\frac{\mu\varepsilon t}{2}\dot{\chi}(t)\right] dt \end{aligned} \tag{A.6}$$

$$\begin{aligned} = & \int \left[\psi(t)^2-\mu^2\chi(t)^2\right] dt + \varepsilon\int t\mu\left[(\dot{\chi}(t)\psi(t)-\chi(t)\dot{\psi}(t)\right] dt \\ & +\frac{\varepsilon^2}{4}\int t^2\left[\ddot{\psi}(t)\psi(t)-\mu^2\ddot{\chi}(t)\chi(t)\right] dt \\ & -\frac{\varepsilon^2}{4}\int t^2\left[\dot{\psi}(t)^2-\mu^2\dot{\chi}(t)^2\right] dt \end{aligned} \tag{A.7}$$

The first term in ε^2 may be integrated by parts.

$$\begin{aligned} N(\varepsilon,\mu) \;\sim\; & \int \left[\psi(t)^2-\mu^2\chi(t)^2\right] dt + \varepsilon\int t\mu\left[\dot{\chi}(t)\psi(t)-\chi(t)\dot{\psi}(t)\right] dt \\ & -\frac{1}{2}\varepsilon^2\int t^2\left[\dot{\psi}(t)^2-\mu^2\dot{\chi}(t)^2\right] dt + \frac{1}{4}\varepsilon^2 r \end{aligned} \tag{A.8}$$

where quantity r is :

$$r = \int \left[\psi(t)^2-\mu^2\chi(t)^2\right] dt - t\left[\psi(t)^2-\mu^2\chi(t)^2\right]\left|-t^2\left[\psi(t)\dot{\psi}(t)-\mu^2\chi(t)\dot{\chi}(t)\right]\right| \tag{A.9}$$

whose expectation is zero and whose typical value is much less – by a factor of $t^2\omega^2$ – than the other coefficient of ε^2 in (A.8). For this reason we henceforth neglect it.

So finally,

$$\partial N(\varepsilon,\mu)/\partial\varepsilon \sim \int \mu t \left[\dot{\chi}(t)\psi(t) - \chi(t)\dot{\psi}(t)\right] dt - \varepsilon \int t^2 \left[\dot{\psi}(t)^2 - \mu^2\dot{\chi}(t)^2\right] dt \quad \text{(A.10)}$$

Equation (A.4) is satisfied for :

$$\varepsilon = n/d \quad \text{(A.11)}$$

where

$$\begin{aligned} n &= \mu \int t \left[\dot{\chi}(t)\psi(t) - \chi(t)\dot{\psi}(t)\right] dt \\ d &= \int \left[t^2(\dot{\psi}(t)^2 - \mu^2\dot{\chi}(t)^2)\right] dt + \frac{1}{4}\int \left[\psi(t)^2 - \mu^2\chi(t)^2\right] dt \end{aligned}$$

Equation (A.11) is an expression for the apparent dilation induced by the difference $2\mu\chi$ between the original waveforms ϕ_1 and ϕ_2. Given specific ψ and χ, one could evaluate it. It will be more useful, however, to obtain statistical estimates for the apparent dilation given assumptions about the envelopes and spectra of ψ and χ. The numerator n has expectation zero, as χ and ψ are statistically unrelated. Thus within the stated limit $\omega t\varepsilon << 1$, differences $\phi_2 - \phi_1$ do not manifest as an apparent dilation and the expected dilation ε is zero.

Given $\langle n\rangle = 0$, one then seeks estimates for the root-mean-square of equation (A.11) in order to judge typical fluctuations around the expected zero. These will be made based on assumptions that ψ and χ are stationary and noise-like and Gaussian, with similar spectra, having central frequency ω_c, and the same durations, long compared to the inverse of ω_c. Without loss of generality it is also assumed that they have the same amplitudes $\langle\psi^2\rangle = \langle\chi^2\rangle = 1$. They are taken to extend from a start time t_1 to an end time t_2. Under these assumptions the denominator of (A.11) is estimated as :

$$d \sim (1-\mu^2)\left[\frac{1}{3}\omega_c^2(t_2^3 - t_1^3) + \frac{1}{4}(t_2 - t_1)\right] \sim (1-\mu^2)\frac{1}{3}\omega_c^2(t_2^3 - t_1^3) \quad \text{(A.12)}$$

The square of the numerator of (A.11) is

$$n^2 \sim \mu^2 \left[\int tt' \left\{\psi(t)\dot{\chi}(t) - \dot{\psi}(t)\chi(t)\right\}\left\{\psi(t')\dot{\chi}(t') - \dot{\psi}(t')\chi(t')\right\} dt\ dt'\right] \quad \text{(A.13)}$$

On changing variables : $t+t' = 2\tau$, $t-t' = \xi$ and dropping the cross terms as having expectation zero, (A.13) becomes :

$$\langle n^2 \rangle \sim \mu^2 \left[\int \left(\tau^2 - \frac{\xi^2}{4} \right) \left\{ \psi\left(\tau + \frac{\xi}{2}\right) \dot{\chi}\left(\tau + \frac{\xi}{2}\right) \psi\left(\tau - \frac{\xi}{2}\right) \dot{\chi}\left(\tau - \frac{\xi}{2}\right) + \dot{\psi}\left(\tau + \frac{\xi}{2}\right) \chi\left(\tau + \frac{\xi}{2}\right) \dot{\psi}\left(\tau - \frac{\xi}{2}\right) \chi\left(\tau - \frac{\xi}{2}\right) \right\} d\tau \; d\xi \right] \tag{A.14}$$

Auto-correlation functions may be defined

$$\langle \psi\left(\tau + \frac{\xi}{2}\right) \psi\left(\tau - \frac{\xi}{2}\right) \rangle = \langle \psi^2(\tau) \rangle R_\psi(\xi) = R(\xi) \tag{A.15}$$

such that

$$\langle \dot{\psi}\left(\tau + \frac{\xi}{2}\right) \dot{\psi}\left(\tau - \frac{\xi}{2}\right) \rangle \sim \omega_c^2 \langle \psi^2(\tau) \rangle R_\psi(\xi) = \omega_c^2 R(\xi) \tag{A.16}$$

with similar expressions for χ. Then the expectation of the square of the numerator of (A.11) is :

$$\langle n^2 \rangle \sim 2\mu^2 \left[\int \left(\tau^2 - \frac{\xi^2}{4} \right) \omega_c^2 \; R^2(\xi) \; d\tau \; d\xi \right] \approx 2 \; \mu^2 \; \omega_c^2 \left[\int \tau^2 d\tau \right] \left[\int R^2(\xi) d\xi \right] \tag{A.17}$$

The first integral is merely $(t_2^3 - t_1^3)/3$. The second requires knowing something of the spectra of ψ and χ, so we take these to be Gaussian and identical :

$$\sim \exp(-(\omega - \omega_c)^2 T^2) + \exp(-(\omega + \omega_c)^2 T^2).$$

T may be identified by noting that the -10dB points are at $\omega_c \pm \ln(10/T)$. In this case R is related to the inverse Fourier transform of the power spectrum : $R(\xi) = \cos(\omega_c \, \xi) \exp(\xi^2/4T^2)$. Then the second integral in (A.17) is identified as $T\sqrt{(\pi/2)}$

Application of Eqs A.11, A.12, A.17 requires that we also estimate the μ. The quantity μ is related to the maximum of the waveform dilation-correlation coefficient

$$X(0,\mu) = \frac{N(0,\mu)}{D(\mu)} = \frac{\int \left(\psi(t)^2 - \mu^2 \chi(t)^2 \right) dt}{\sqrt{\left[\int \left(\psi^2 + \mu^2 \chi^2 \right) dt \right]^2 - 4\mu^2 \left[\int \chi \; \psi \; dt \right]^2}} \tag{A.18}$$

As χ and ψ are statistically independent, one estimates the following relation between the maximum of the dilation correlation coefficient and the parameter μ :

$$X = \frac{1-\mu^2}{1+\mu^2} \tag{A.19}$$

Finally, the root mean square of the practitioner's (erroneous) estimate for the relative dilation between ϕ_1 and ϕ_2 is

$$\text{rms } \varepsilon = \frac{\langle n^2 \rangle^{1/2}}{d} = \frac{\sqrt{1-X^2}}{2X} \sqrt{\frac{6\sqrt{\frac{\pi}{2}}T}{\omega_c^2 \ (t_2^3 - t_1^3)}} \tag{A.20}$$

This scales inversely with the duration of the correlation waveform in units of the period, and inversely with the square root of the duration in units of the inverse bandwidth. In practice (A.20) can be very small. The quantity $\omega(t_2 - t_1)$ is of the order of the coda-Q, the duration of the waveform in units of the period. The quantity T is the amount of time for one bit of information to be delivered. Thus (A.20) can be recognized as scaling inversely with Q, and inversely with the square root of the amount of information. It also may be recognized that small X corresponding to waveforms ϕ_1 and ϕ_2 that are very different, permits the practitioners erroneous estimate of dilation to be large.

Application of equation (A.20) is straightforward. A practitioner's estimate of the relative dilation ε between two waveforms ϕ_1 and ϕ_2 may be compared to (A.20). Values in excess of (A.20) are consistent with the inference that the observed dilation is real ; changes in waveform source or other character ought not generate apparent dilations in excess of (A.20). Furthermore, absent any actual dilation, estimates of ε of the order of (A.20) will nevertheless be generated in practice. Such should be regarded as unmeaningful.

A.1.3 Comparison with Experiment

The prediction (A.20) has been compared to waveform dilation measurements in a laboratory ultrasonic experiment [Hadziioannou et al., 2009]. Several piezoelectric sensors and sources were applied to a multiply scattering air-bubble filled gel. Sources and receivers were placed on opposite sides, 64 mm apart. Multiple scattering was strong ; received waveforms $f_{sr}(t)$ from sources s to receivers r, were coda-like, with envelopes that resembled the solution of a diffusion equation, figure A.1. The auto-correlation of each $f_{sr}(t)$ was windowed between lapse times of 12.5 to 50 μsec, to yield the waveforms which we call $g_{sr}(\tau)$. Details of the experimental

set-up are described in [Hadziioannou et al., 2009]. The details are, however, unimportant here, as the present theory applies to any pair of coda-like waveforms ϕ_1 and ϕ_2. The typical g_{sr} is stationary over this interval and has a power spectrum centered on 2.35 MHz with -10dB points at 1.7 and 3.0 MHz.

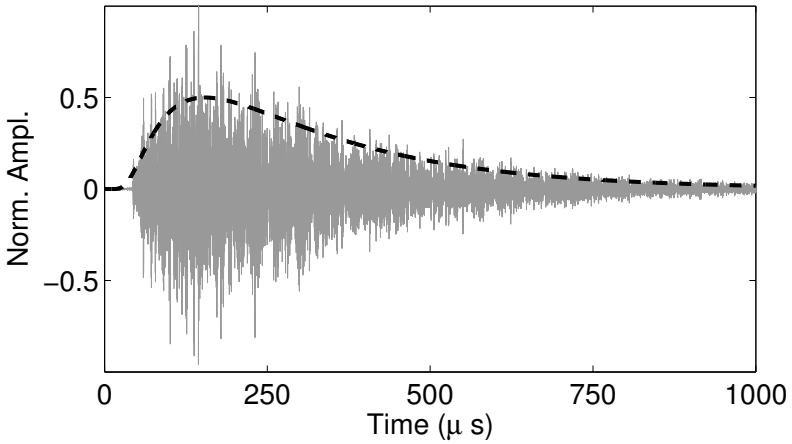

FIG. A.1 – Gray line : acoustic field transmitted through the 64 mm thick bubble-gel mixture (in normalized amplitude). Black broken line : 2D diffusion equation for $\ell^\star = 3.5$ mm and $\ell_a = 200$ mm.

The tables below are formed by maximizing the dilation correlation coefficient X between sums $\phi = \sum_s g_{sr}$ over different sets of sources $\{s\}$. The ϕ are not Green's functions G_{rr}, as the fields $f_{sr}(t)$ used to compose them were not fully equipartitioned ; the excellent impedance match between the gel and the receivers left the field within the receivers essentially zero ; the noise field lacked any components traveling from receiver to receiver. All tests were conducted at fixed temperature, the actual relative temporal dilation is therefore zero.

Autocorrelation waveforms in the interval from 12.5 to 50 μsec appear stationary. Thus we take t_1=12.5 μsec, $t_2 = 50$ μsec, $\omega_c = 15\text{rad}/\mu\text{sec}$; and $T = 0.56$ μsec and conclude from (A.20),

$$\text{rms } \varepsilon = 3.8 \times 10^{-4} \, \frac{\sqrt{1 - X^2}}{2X} \tag{A.21}$$

It may be that lengthening the considered time interval beyond the chosen 12.5 $\rightarrow$ 50 μsec would increase the precision. However, it could also diminish X : in principle there are trade-offs.

Tables A.1 and A.2 show two case studies.In the first case, autocorrelations calculated from the signals at a receiver r, as produced by eleven distinct sources s, were

X for seven receivers and three different choices for the set of sources

set 1	0.9312	0.9169	0.8893	0.8458	0.8226	0.8852	0.8683
set 2	0.9394	0.8833	0.9083	0.8464	0.8872	0.8631	0.8928
set 3	0.9458	0.9009	0.8730	0.7942	0.8322	0.8396	0.7979

The dilation ε ($\times 10^{-3}$) as obtained by maximizing X for each of these cases

set 1	0.06	0.04	-0.16	0.08	-0.04	-0.10	0.18
set 2	-0.04	-0.04	-0.08	0.06	-0.14	-0.08	0.10
set 3	-0.16	0.08	-0.12	0.00	-0.14	-0.24	-0.12

Experimental root mean square dilation ε ($\times 10^{-3}$)

all sets	0.1013	0.0566	0.1244	0.0577	0.1166	0.1571	0.1376

Theoretical root mean square (A.21)

all sets	0.07	0.09	0.09	0.12	0.11	0.10	0.11

TAB. A.1 – Comparison of best-fit waveform dilations ε with the predictions of equation (A.21). A maximum value of X and the ε at which that X is maximum, are constructed for each of seven receivers (the seven columns) and the three choices for the set of sources described in the text (the three rows). The root mean square of those ε is compared with the predictions of theory. That X is of order 90% is consistent with one source in ten having changed.

summed over to generate the reference waveform $\phi_1 = \sum_s g_{sr}$. For each of three comparison waveforms ϕ_2, the same sum was done, keeping the first ten sources unchanged, but replacing the eleventh with sources number twelve, thirteen and fourteen respectively. This was repeated for each of seven receivers. In each case we compare three waveforms ϕ_2 with the reference ϕ_1 and evaluate $X(\varepsilon)$. The table shows the maximum value of $X(\varepsilon)$, and the value of ε that did this, for each of the 21 cases. For each of the seven receivers we calculate the rms of these three ε. Inasmuch as the only changes were to the source of the noise field, and not the medium, one would expect no dilation, or $\varepsilon = 0$. Nevertheless, the differences in sources do generate apparent dilations ε. Theory, especially in light of the approximate modeling of the spectrum, may be said to have done a good job predicting the fluctuations.

In the second study, four sources were held constant, and two were varied. Here the reference waveform was constructed from a sum over six sources $\sum_s g_{sr}$; each of the other three waveforms was constructed by replacing sources number five and six in that sum with two others. Again, the theory may be said to have done a good job.

X for seven receivers and three different choices for the set of sources

set 1	0.6181	0.7864	0.7143	0.8400	0.7149	0.8458	0.7863
set 2	0.6359	0.7340	0.7011	0.8451	0.8020	0.8285	0.8194
set 3	0.5948	0.7397	0.5837	0.8165	0.8294	0.8451	0.8745

The dilation ε ($\times 10^{-3}$) as obtained by maximizing X for each of these cases

set 1	-0.0800	0.0400	0.4600	-0.0200	0.1400	0.0400	0.1600
set 2	-0.0200	0.0400	0.0400	-0.3400	-0.0800	-0.1400	0.0800
set 3	-0.4600	0.1600	0.5600	-0.0400	0.0800	-0.0400	0.0400

Experimental root mean square dilation ε ($\times 10^{-3}$)

all sets	0.27	0.098	0.419	0.198	0.104	0.087	0.106

Theoretical root mean square (A.21)

all sets	0.19	0.14	0.17	0.12	0.14	0.12	0.11

TAB. A.2 – As in table A.1, but for sources that differ by more, as evident in the smaller values of X

A.1.4 Comparison with Seismic Data from Parkfield

We also analyze data from seismic measurements near Parkfield California. Brenguier et al. [2008a] showed that correlation waveforms obtained from ambient seismic noise over a period of five years from 2002 to 2007 changed in a manner consistent with a decrease of seismic velocity after the earthquake of 2004. This decrease then relaxed like $\log(t)$ after the earthquake. While they used the doublet technique, we have re-analyzed their data using the dilation coefficient (equation (A.1)). For each of 78 receiver pairs, we compared the 1550-day average correlation waveform with the correlation waveform constructed from each of 1546 overlapping 5-day segments. Each correlation waveform was windowed between -50 and -20 seconds, and again from 20 to 50 seconds (thus excluding direct Rayleigh arrivals and emphasizing the multiply scattered diffuse part of the signal for which the theory was developed). As in the previous section, the details of the measurements are available elsewhere [Brenguier et al., 2008a] but are unimportant for the present purposes. An X and an ε were deduced for each day. Power spectra were centered on 0.5 Hz, with -10dB shoulders at 0.1 and 0.9 Hz. These numbers permit the evaluation of (A.20) :

$$\text{rms } \varepsilon = 3 \times 10^{-3} \, \frac{\sqrt{1 - X^2}}{2X} \tag{A.22}$$

Figures A.2 shows the mean (over the 78 receiver pairs) values of X and ε between each of the 1546 overlapping 5-day correlation waveforms, ϕ_1, and the correlation waveform ϕ_2 as obtained by averaging over the entire 5 year period. Except for the

two events on December 22, 2003 and September 28, 2004, and the slow relaxation after the latter, the dilation appears constant, with daily random fluctuations of order 10^{-4}. A correlation coefficient X of 0.8 predicts a rms fluctuation, equation (A.22), of 10^{-3}. On averaging over 78 pairs, this prediction is reduced by a factor $\sqrt{78}$, to 1.1×10^{-4}, consistent with the observed fluctuations in ε. In light of the approximations, in particular that of modeling the spectrum as Gaussian and the waveform as stationary, we count this as excellent agreement.

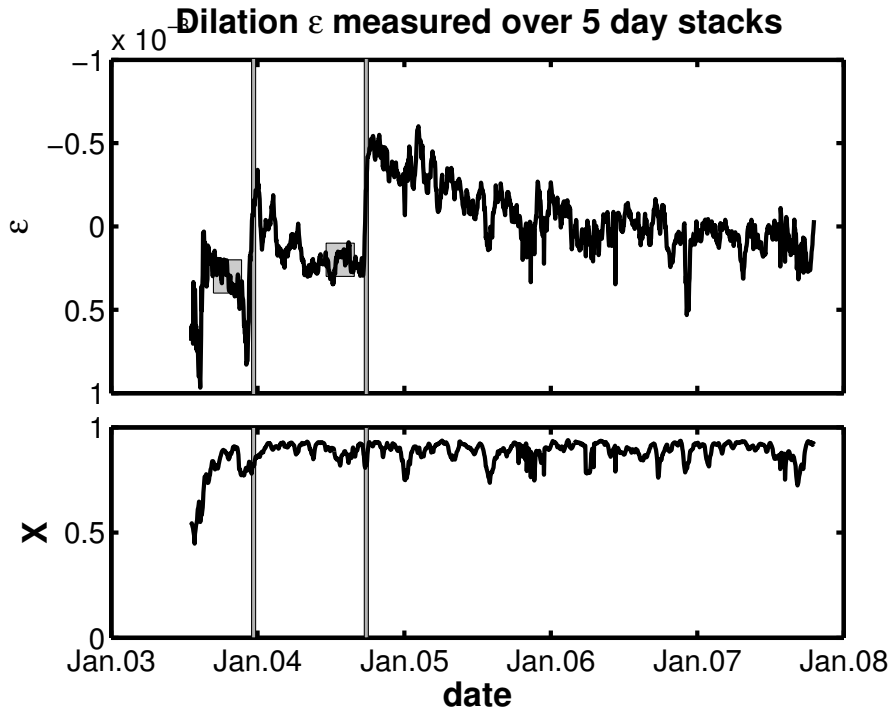

FIG. A.2 – Top : Dilation ε averaged over 78 receiver pairs, using a 5-day sliding window. The grey squares indicate the 70-day reference windows. The best fit ε varied weakly and stochastically over this period, with two notable jumps, after December 22, 2003 and after the Parkfield earthquake on September 28, 2004. The latter jump was followed by a slow recovery. Fluctuations have an rms strength of about 10^{-4}. Bottom : Dilation coefficient X. The maximum value of the dilation coefficient X, averaged over 78 receiver pairs.

The discontinuities in ε on December 22, 2003 and September 28, 2004 are of particular interest. The latter is coincident with the Parkfield earthquake. Jumps in dilation on those dates by $\sim 0.8 \times 10^{-3}$ were interpreted [Brenguier et al., 2008a] as decreases of local seismic wavespeed. But one might wish to entertain the hypothesis that these jumps are due to a change in the source of the noise. To examine the question, we evaluated X and ε using correlation waveforms ϕ_1 as averaged over a 70-day period before each event as a reference and correlation waveforms ϕ_2 obtained over a series of 5 day spans after the events. The relative dilation across the events are the same as seen in figure A.2, of order 5×10^{-4}. The values of X for

these pairs of waveforms varied between 60% and 70%. According to equation (**??**), divided by $\sqrt{78}$ the value of X would have had to be below 33% if this large an apparent dilation were to be a random function of the field having changed in a manner unrelated to actual dilation. The relative dilation between correlation waveforms before and after the event is therefore due to changes in seismic Green's function, and not to changes in the source of the waves.

A.1.5 Summary

Waveforms constructed by noise correlation can be extraordinarily sensitive to changes in material properties. Such waveforms are in principle affected by both changes in noise sources and changes in the acoustic properties of the medium in which the waves propagate. It has been shown here long-duration diffuse waveforms permit changes in the source of the noise to be distinguished with high precision from changes due to a temporal dilation.

Bibliographie

Aki, K. (1957). Space and time spectra of stationary stochastic waves with special reference to microtremors. *Bull. Earthquake Res. Inst.Tokyo Univ.*, 35 :415–456. 10

Aki, K. and Chouet, B. (1975). Origin of coda waves : Source, attenuation, and scattering effects. *J. Geophys. Res.*, 80 :3322–3342. 6

Allmann, B. and Shearer, P. (2007). Spatial and temporal stress drop variations in small earthquakes near Parkfield, California. *J. Geophys. Res.*, 112(B04305) :B04305. 25

Baig, A., Campillo, M., and Brenguier, F. (2009). Denoising seismic noise cross correlations. *J. Geophys. Res.*, 114. 72, 78

Bakun, W. and Lindh, A. (1985). The Parkfield, California, earthquake prediction experiment. *Science*, 229(4714) :619–624. 24

Bensen, G., Ritzwoller, M., Barmin, M., Levshin, A., Lin, F., Moschetti, M., Shapiro, N., and Yang, Y. (2007). Processing seismic ambient noise data to obtain reliable broad-band surface wave dispersion measurements. *Geophys. J. Int.*, 169(3) :1239–1260. 26, 93

Bensen, G., Ritzwoller, M., and Shapiro, N. (2008). Broad-band ambient noise surface wave tomography across the United States. *Geophys. J. Int.*, 113. 11

Bonnefoy-Claudet, S., Cotton, F., and Bard, P. (2006). The nature of noise wavefield and its applications for site effects studies : : A literature review. *Earth-Science Reviews*, 79(3-4) :205–227. 14

Brenguier, F., Campillo, M., Hadziioannou, C., Shapiro, N., Nadeau, R. M., and Larose, E. (2008a). Postseismic relaxation along the San Andreas fault at Parkfield from continuous seismological observations. *Science*, 321(5895) :1478–1481. 43, 49, 56, 75, 81, 96, 115, 123, 124

Brenguier, F., Shapiro, N., Campillo, M., Ferrazzini, V., Duputel, Z., Coutant, O., and Nercessian, A. (2008b). Towards forecasting volcanic eruptions using seismic noise. *Nature Geoscience*, 1(2) :126–130. 4, 26, 28, 29, 40, 43, 49, 64, 81, 115

Brenguier, F., Shapiro, N., Campillo, M., Nercessian, A., and Ferrazzini, V. (2007). 3-D surface wave tomography of the Piton de la Fournaise volcano using seismic noise correlations. *Geophys. Res. Lett.*, 34(2) :2305. 11, 26

Campillo, M. (2006). Phase and Correlation in Random Seismic Fields and the Reconstruction of the Green Function. *Pure and Applied Geophysics*, 163(2) :475–502. 26

Campillo, M., Chen, J., Froment, B., and Liu, Q. (2009). Evidence of depth dependence of the seismic velocity temporal change associated with the Wenchuan earthquake. In *AGU Fall Meeting Abstracts*, volume 1, page 02. 102

Campillo, M. and Paul, A. (2003). Long-range correlations in the diffuse seismic coda. *Science*, 299(5606) :547. 11, 39, 93

Claerbout, J. (1968). Synthesis of a layered medium from its acoustic transmission response. *Geophysics*, 33 :264. 10

De Rosny, J. and Roux, P. (2001). Multiple scattering in a reflecting cavity : Application to fish counting in a tank. *J. Acoust. Soc. Am.*, 109 :2587. 114

Derode, A., Larose, E., Campillo, M., and Fink, M. (2003a). How to estimate the Green's function of a heterogeneous medium between two passive sensors ? Application to acoustic waves. *Appl. Phys. Lett.*, 83 :3054. 10

Derode, A., Larose, E., Tanter, M., de Rosny, J., Tourin, A., Campillo, M., and Fink, M. (2003b). Recovering the Green's function from field-field correlations in an open scattering medium (L). *J. Acoust. Soc. Am.*, 113 :2973. 10, 11, 12, 114

Duvall, T. L., Jefferies, S. M., Harvey, J. W., and Pomerantz, M. A. (1993). Time-distance helioseismology. *Nature*, 362 :430–432. 10, 39

Ellison, S. J., Imhof, M. G., Çoruh, C., Fuqua, A. D., and Henry, S. C. (2004). Modeling offset-dependent reflectivity for time-lapse monitoring of water-flood production in thin-layered reservoirs. *Geophysics*, 69(1) :25–36. 57

Fink, M. (1992). Time reversal of ultrasonic fields – Part I : Basic principles. *IEEE Trans. Ultrason. Ferroelectr. Freq. Control*, 39(5) :555–566. 12

Frechet, J., Martel, L., Nikolla, L., and Poupinet, G. (1989). Application of the Cross-Spectral Moving-Window Technique (CSMWT) to the Seismic Monitoring of Forced Fluid Migration in a Rock Mass. *Int. J. Rock Mech. Min. Sci.*, 26(3-4) :221–233. 44, 80

Freed, A. (2007). Afterslip (and only afterslip) following the 2004 Parkfield, California, earthquake. *Geophys. Res. Lett.*, 34(6). 30, 83, 89

Friedrich, A., Krüger, F., and Klinge, K. (1998). Ocean-generated microseismic noise located with the Gräfenberg array. *Journal of Seismology*, 2(1) :47–64. 14

Froment, B., Campillo, M., Roux, P., Gouédard, P., Verdel, A., and Weaver, R. (2010). Estimation of the effect of non-isotropic distributed energy on the apparent arrival time in correlations. *Geophysics*, 75(5) :SA85–SA93. 64, 74, 85, 96, 97, 115

Fukushima, Y., Nishizawa, O., Sato, H., and Ohtake, M. (2003). Laboratory study on scattering characteristics of shear waves in rock samples. *Bull. Seismol. Soc. Am.*, 93(1) :253. 41

Gerstoft, P. and Tanimoto, T. (2007). A year of microseisms in southern California. *Geophys. Res. Lett.*, 34 :L20304. 73

Gorin, T., Seligman, T., and Weaver, R. (2006). Scattering fidelity in elastodynamics. *Phys. Rev. E*, 73(1) :15202. 114

Gouédard, P., Roux, P., Campillo, M., and Verdel, A. (2008). Convergence of the two-point correlation function toward the green's function in the context of a seismic-prospecting data set. *Geophysics*, 73(6) :V47–V53. 85

Gouédard, P., Stehly, L., Brenguier, F., Campillo, M., Colin de Verdiere, Y., Larose, E., Margerin, L., Roux, P., Sanchez-Sesma, F., Shapiro, N., et al. (2008). Cross-correlation of random fields : mathematical approach and applications. *Geophysical prospecting*, 56(3) :375–394. 114

Gutenberg, B. (1936). On microseisms. *Bull. Seismol. Soc. Am.*, 26(2) :111. 14

Hadziioannou, C., Larose, E., Coutant, O., Roux, P., and Campillo, M. (2009). Stability of Monitoring Weak Changes in Multiply Scattering Media with Ambient Noise Correlation : Laboratory Experiments. *J. Acoust. Soc. Am.*, 125(6) :3688–3695. 74, 75, 81, 120, 121

Hennino, R., Trégoures, N., Shapiro, N., Margerin, L., Campillo, M., Van Tiggelen, B., and Weaver, R. (2001). Observation of equipartition of seismic waves. *Phys. Rev. Lett.*, 86(15) :3447–3450. 9

Hikima, K. and Koketsu, K. (2005). Rupture processes of the 2004 Chuetsu (mid-Niigata prefecture) earthquake, Japan : A series of events in a complex fault system. *Geophys. Res. Lett.*, 32(18) :L18303. 92

Jenkins, G. and Watts, D. (1969). *Spectral Analysis and Its Applications*. Emerson-Adams Press. 44, 80

Johanson, I., Fielding, E., Rolandone, F., and Burgmann, R. (2006). Coseismic and Postseismic Slip of the 2004 Parkfield Earthquake from Space-Geodetic Data. *Bull. Seismol. Soc. Am.*, 96(4 B) :269–282. 30, 89

Johnson, K. M., Burgmann, R., and Larson, K. (2006). Frictional Properties on the San Andreas Fault near Parkfield, California, Inferred from Models of Afterslip following the 2004 Earthquake. *Bull. Seismol. Soc. Am.*, 96(4B) :S321–338. 30

Kedar, S. and Webb, F. (2005). The Ocean's Seismic Hum. *Science*, 307(5710) :682–683. 28

Landès, M., Hubans, F., Shapiro, N., Paul, A., and Campillo, M. (2010). Origin of deep ocean microseisms by using teleseismic body waves. *J. Geophys. Res.*, 115. 14, 15, 73, 94

Larose, E., Campillo, M., Khan, A., and Nakamura, Y. (2005a). Lunar subsurface investigated from correlation of seismic noise. *Geophys. Res. Lett.*, 32(16) :L16201. 114

Larose, E., Derode, A., Campillo, M., and Fink, M. (2004). Imaging from one-bit correlations of wideband diffuse wave fields. *J. Appl. Phys.*, 95 :8393. 37, 93

Larose, E., Derode, A., Clorennec, D., Margerin, L., and Campillo, M. (2005b). Passive retrieval of Rayleigh waves in disordered elastic media. *Phys. Rev. E*, 72(4) :46607. 41

Larose, E. and Hall, S. (2009). Monitoring stress related velocity variation in concrete with a 2.10^{-5} relative resolution using diffuse ultrasound. *J. Acoust. Soc. Am.*, 125 :1853–1856. 40

Larose, E., Margerin, L., Derode, A., van Tiggelen, B., Campillo, M., Shapiro, N., Paul, A., Stehly, L., and Tanter, M. (2006). Correlation of random wavefields : An interdisciplinary review. *Geophysics*, 71(4). 39

Larose, E., Planes, T., Rossetto, V., and Margerin, L. (2010). Locating a small change in a multiple scattering environment. *Appl. Phys. Lett.*, 96(20). 110

Larose, E., Roux, P., Campillo, M., and Derode, A. (2008). Fluctuations of correlations and Green's function reconstruction : role of scattering. *J. Appl. Phys.*, 103(11) :114907–114907. 75

Li, Y., Chen, P., Cochran, E., and Vidale, J. (2007). Seismic velocity variations on the San Andreas fault caused by the 2004 M6 Parkfield Earthquake and their implications. *Earth Planets Space*, 59(1) :21–31. 20, 24, 74

Li, Y., Vidale, J., Aki, K., Xu, F., and Burdette, T. (1998). Evidence of Shallow Fault Zone Strengthening After the 1992 ? M7. 5 Landers, California, Earthquake. *Science*, 279(5348) :217. 23

Li, Y., Vidale, J., Day, S., Oglesby, D., and Cochran, E. (2003). Postseismic Fault Healing on the Rupture Zone of the 1999 M 7.1 Hector Mine, California, Earthquake. *Bull. Seismol. Soc. Am.*, 93(2) :854–869. 25, 30, 89

Lobkis, O. and Weaver, R. (2001). On the emergence of the Green's function in the correlations of a diffuse field. *J. Acoust. Soc. Am.*, 110 :3011. 10, 39, 114

Lobkis, O. and Weaver, R. (2003). Coda-Wave Interferometry in Finite Solids : Recovery of P-to-S Conversion Rates in an Elastodynamic Billiard. *Phys. Rev. Lett.*, 90(25) :254302. 21, 40, 43, 44, 63, 81, 97, 113, 114

Lobkis, O. and Weaver, R. (2008). Scattering fidelity in elastodynamics. II. Further experimental results. *Phys. Rev. E*, 78(6) :66212. 114

Longuet-Higgins, M. (1950). A theory of the origin of microseisms. *Philosophical Transactions of the Royal Society of London. Series A. Mathematical and Physical Sciences*, 243(857) :1–35. 15

Lu, Y. and Michaels, J. (2005). A methodology for structural health monitoring with diffuse ultrasonic waves in the presence of temperature variations. *Ultrasonics*, 43(9) :717–731. 114

Luis, J. F. (2007). Mirone : A multi-purpose tool for exploring grid data. *Computers & Geosciences*, 33 :31–41. 27

Ma, S., Custódio, S., Archuleta, R., and Liu, P. (2008). Dynamic modeling of the 2004 M w 6.0 Parkfield, California, earthquake. *J. Geophys. Res.*, 113 :B02301. 30

Nadeau, R. and Dolenc, D. (2005). Nonvolcanic Tremors Deep Beneath the San Andreas Fault. *Science*, 307(5708) :389–389. 27, 34

Nishida, K., Kobayashi, N., and Fukao, Y. (2002). Origin of Earth's ground noise from 2 to 20 mHz. *Geophys. Res. Lett.*, 29(10) :1413. 14

Nishimura, T., Tanaka, S., Yamawaki, T., Yamamoto, H., Sano, T., Sato, M., Nakahara, H., Uchida, N., Hori, S., and Sato, H. (2005). Temporal changes in seismic velocity of the crust around Iwate volcano, Japan, as inferred from analyses of repeated active seismic experiment data from 1998 to 2003. *Earth Planets Space*, 57 :491. 24

Niu, F., Silver, P., Daley, T., Cheng, X., and Majer, E. (2008). Preseismic velocity changes observed from active source monitoring at the Parkfield SAFOD drill site. *Nature*, 454(7201) :204–208. 25

Niu, F., Silver, P., Nadeau, R., and McEvilly, T. (2003). Migration of seismic scatterers associated with the 1993 Parkfield aseismic transient event. *Nature*, 426(6966) :544–548. 74, 89

Obara, K. (2002). Nonvolcanic Deep Tremor Associated with Subduction in Southwest Japan. *Science*, 296(5573) :1679–1681. 34

Obara, K., Kasahara, K., Hori, S., and Okada, Y. (2005). A densely distributed high-sensitivity seismograph network in Japan : Hi-net by National Research Institute for Earth Science and Disaster Prevention. *Review of Scientific Instruments*, 76 :021301. 91

Okada, Y., Kasahara, K., Hori, S., Obara, K., Sekiguchi, S., Fujiwara, H., and Yamamoto, A. (2004). Recent progress of seismic observation networks in Japan-Hi-net, F-net, K-NET and KiK-net. *Earth Planets Space*, 56(8). 91, 92

Paul, A., Campillo, M., Margerin, L., Larose, E., and Derode, A. (2005). Empirical synthesis of time-asymmetrical Green functions from the correlation of coda waves. *J. Geophys. Res.*, 110. 85

Peng, Z. and Ben-Zion, Y. (2006). Temporal changes of shallow seismic velocity around the Karadere-Düzce branch of the north Anatolian fault and strong ground motion. *Pure and Applied Geophysics*, 163(2) :567–600. 74, 89

Pine, D., Weitz, D., Chaikin, P., and Herbolzheimer, E. (1988). Diffusing wave spectroscopy. *Phys. Rev. Lett.*, 60(12) :1134–1137. 40

Poupinet, G., Ellsworth, W., and Frechet, J. (1984). Monitoring Velocity Variations in the Crust Using Earthquake Doublets - An Application to the Calaveras Fault, California. *J. Geophys. Res.*, 89(NB7) :5719–5731. 18, 23, 29, 40, 43, 49, 80, 82, 113, 114

Poupinet, G., Got, J., and Brenguier, F. (2008). Monitoring Temporal Variations of Physical Properties in the Crust by Cross-Correlating the Waveforms of Seismic Doublets. *Adv. in geophys.*, 50 :373–399. 19

Rhie, J. and Romanowicz, B. (2004). Excitation of earth's continuous free oscillations by atmosphere-ocean-seafloor coupling. *Nature*, 431 :552–556. 40

Rogers, G. and Dragert, H. (2003). Episodic Tremor and Slip on the Cascadia Subduction Zone : The Chatter of Silent Slip. *Science*, 300(5627) :1942–1943. 34

Roux, P. (2009). Passive seismic imaging with directive ambient noise : application to surface waves and the san andreas fault in parkfield, ca. *Geophys. J. Int.*, 179(1) :367–373. 85, 86

Roux, P. and Kuperman, W. (2004). Extracting coherent wave fronts from acoustic ambient noise in the ocean. *J. Acoust. Soc. Am.*, 116 :1995. 73

Roux, P., Sabra, K., Kuperman, W., and Roux, A. (2005). Ambient noise cross correlation in free space : Theoretical approach. *J. Acoust. Soc. Am.*, 117 :79. 10, 114

Rubinstein, J. and Beroza, G. (2004). Evidence for Widespread Nonlinear Strong Ground Motion in the MW 6.9 Loma Prieta Earthquake. *Bull. Seismol. Soc. Am.*, 94(5) :1595–1608. 89

Rubinstein, J. and Beroza, G. (2005). Depth constraints on nonlinear strong ground motion from the 2004 Parkfield earthquake. *Geophys. Res. Lett.*, 32. 30, 83

Rubinstein, J., Uchida, N., and Beroza, G. (2007a). Seismic velocity reductions caused by the 2003 Tokachi-Oki earthquake. *J. Geophys. Res.*, 112(B5). 74

Rubinstein, J., Vidale, J., Gomberg, J., Bodin, P., Creager, K., and Malone, S. (2007b). Non-volcanic tremor driven by large transient shear stresses. *Nature*, 448(7153) :579–582. 34

Sabra, K., Gerstoft, P., Roux, P., Kuperman, W., and Fehler, M. (2005a). Surface wave tomography from microseisms in Southern California. *Geophys. Res. Lett.*, 32(10.1029). 75, 114

Sabra, K. G., Gerstoft, P., Roux, P., Kuperman, W. A., and Fehler, M. C. (2005b). Extracting time-domain green's function estimates from ambient seismic noise. *Geophys. Res. Lett.*, 32 :L03310. 37

Sabra, K. G., Roux, P., Gerstoft, P., Kuperman, W. A., and Fehler, M. C. (2006). Extracting coherent coda arrivals from cross-correlations of long period seismic waves during the mount st. helens 2004 eruption. *Geophys. Res. Lett.*, 33 :L06313. 40, 115

Sanchez-Sesma, F. and Campillo, M. (2006). Retrieval of the Green's function from cross correlation : the canonical elastic problem. *Bull. Seismol. Soc. Am.*, 96(3) :1182. 11, 73

Sawazaki, K., Sato, H., Nakahara, H., and Nishimura, T. (2009). Time-Lapse Changes of Seismic Velocity in the Shallow Ground Caused by Strong Ground Motion Shock of the 2000 Western-Tottori Earthquake, Japan, as Revealed from Coda Deconvolution Analysis. *Bull. Seismol. Soc. Am.*, 99(1) :352–366. 89

Schimmel, M. and Paulssen, H. (1997). Noise reduction and detection of weak, coherent signals through phase-weighted stacks. *Geophys. J. Int.*, 130(2) :497–505. 80

Sens-Schönfelder, C. (2008). Synchronizing seismic networks with ambient noise. *Geophys. J. Int.*, 174(3) :966–970. 96

Sens-Schönfelder, C. and Larose, E. (2008). Temporal changes in the lunar soil from correlation of diffuse vibrations. *Phys. Rev. E*, 78(4) :45601. 40, 81

Sens-Schönfelder, C. and Wegler, U. (2006). Passive image interferometry and seasonal variations of seismic velocities at Merapi Volcano, Indonesia. *Geophys. Res. Lett.*, 33 :1–5. 4, 21, 26, 40, 43, 81, 97, 115

Shapiro, N. and Campillo, M. (2004). Emergence of broadband Rayleigh waves from correlations of the ambient seismic noise. *Geophys. Res. Lett.*, 31(7) :1615–1619. 11, 39, 73

Shapiro, N., Campillo, M., Stehly, L., and Ritzwoller, M. (2005). High-resolution surface-wave tomography from ambient seismic noise. *Science*, 307(5715) :1615. 11, 15, 26, 74, 114

Snieder, R. (2004). Extracting the Green's function from the correlation of coda waves : A derivation based on stationary phase. *Phys. Rev. E*, 69(4). 10, 37, 114

Snieder, R., Grêt, A., Douma, H., and Scales, J. (2002). Coda wave interferometry for estimating nonlinear behavior in seismic velocity. *Science*, 295(5563) :2253. 40, 41, 49, 113

Song, X. and Richards, P. (1996). Seismological evidence for differential rotation of the Earth's inner core. *Nature*, 382(6588) :221–224. 114

Stehly, L., Campillo, M., Froment, B., and Weaver, R. L. (2008). Reconstructing green's function by correlation of the coda of the correlation (c^3) of ambient seismic noise. *J. Geophys. Res.*, 113 :B11306. 16, 56

Stehly, L., Campillo, M., and Shapiro, N. (2006). A study of the seismic noise from its long-range correlation properties. *J. Geophys. Res.*, 111. 14, 15, 28, 40

Stehly, L., Campillo, M., and Shapiro, N. M. (2007). Traveltime measurements from noise correlation : stability and deection of instrumental time-shifts. *Geophys. J. Int.*, 171(1) :223–230. 29, 49, 94, 96

Stockwell, R. (2007). A basis for efficient representation of the S-transform. *Digital Signal Processing*, 17(1) :371–393. 78

Stockwell, R., Mansinha, L., and Lowe, R. (1996). Localization of the complex spectrum : The S transform. *IEEE Transactions on Signal Processing*, 44(4) :998–1001. 78

Urabe, T. and Tsukuda, S. (1992). WIN – A program on workstation for support of manual phase picking process on seismograms recorded by microearthquake observation network. *Programme and Abstract, Seism. Soc. Japan*, (2) :41. *in Japanese.* 93

van Wijk, K., Haney, M., and Scales, J. (2004). 1D energy transport in a strongly scattering laboratory model. *Phys. Rev. E*, 69(3) :36611. 41

Vidale, J. and Li, Y. (2003). Damage to the shallow Landers fault from the nearby Hector Mine earthquake. *Nature*, 421(6922) :524–526. 24, 25, 30

Wapenaar, K. (2004). Retrieving the elastodynamic Green's function of an arbitrary inhomogeneous medium by cross correlation. *Phys. Rev. Lett.*, 93 :254 301. 11, 73

Wapenaar, K. and Fokkema, J. (2006). Green's function representations for seismic interferometry. *Geophysics*, 71 :SI33–SI46. 11

Weaver, R., Froment, B., and Campillo, M. (2009a). On the correlation of non-isotropically distributed ballistic scalar diffuse waves. *J. Acoust. Soc. Am.*, 126(4) :1817–1826. 64, 96, 97, 115

Weaver, R., Hadziioannou, C., Larose, E., , and Campillo, M. (2009b). On the precision of noise-correlation interferometry. (a). *J. Acoust. Soc. Am.*, 125 :2536. 88

Weaver, R. and Lobkis, O. (2001). Ultrasonics without a Source : Thermal Fluctuation Correlations at MHz Frequencies. *Phys. Rev. Lett.*, 87(13) :134301. 10, 39, 51

Weaver, R. and Lobkis, O. (2004). Diffuse fields in open systems and the emergence of the Green's function(L). *J. Acoust. Soc. Am.*, 116(5) :2731–2734. 73, 114

Wegler, U., Nakahara, H., Sens-Schönfelder, C., Korn, M., and Shiomi, K. (2009). Sudden drop of seismic velocity after the 2004 Mw 6.6 Mid-Niigata earthquake, Japan, observed with passive image interferometry. *J. Geophys. Res.*, 114(B6) :B06305. 100

Wegler, U. and Sens-Schöenfelder, C. (2007). Fault zone monitoring with passive image interferometry. *Geophys. J. Int.*, 168(3) :1029–1033. 26

Yang, Y., Zheng, Y., Chen, J., Zhou, S., Celyan, S., Sandvol, E., Tilmann, F., Priestley, K., Hearn, T., Ni, J., et al. (2010). Rayleigh wave phase velocity maps of Tibet and the surrounding regions from ambient seismic noise tomography. *Geochemistry, Geophysics, Geosystems*, 11(8) :Q08010. 11

Yao, H., Beghein, C., and Van der Hilst, R. (2008). Surface wave array tomography in SE Tibet from ambient seismic noise and two-station analysis–II. Crustal and upper-mantle structure. *Geophys. J. Int.*, 173(1) :205–219. 11

Yao, H., Van der Hilst, R., and De Hoop, M. (2006). Surface-wave array tomography in SE Tibet from ambient seismic noise and two-station analysis–I. Phase velocity maps. *Geophys. J. Int.*, 166(2) :732–744. 11

Zagzebski, J. (1996). *Essentials of ultrasound physics*. 42

Zhang, J., Song, X., Li, Y., Richards, P., Sun, X., and Waldhauser, F. (2005). Inner core differential motion confirmed by earthquake waveform doublets. *Science*, 309(5739) :1357. 114